

**INVESTIGATIONS OF NOVEL  
HYDROGEN ADSORPTION PHENOMENA**

---

A Dissertation presented to  
the Faculty of the Graduate School  
at the University of Missouri

---

In Partial Fulfillment  
of the Requirements for the Degree  
Doctor of Philosophy

---

by

RAINA JANEL OLSEN

Dr. Carlos Wexler, Dissertation Supervisor

MAY 2011

The undersigned, appointed by the Dean of the Graduate School, have examined the dissertation entitled:

INVESTIGATIONS OF NOVEL  
HYDROGEN ADSORPTION PHENOMENA

presented by Raina Janel Olsen,  
a candidate for the degree of Doctor of Philosophy and hereby certify that, in their opinion, it is worthy of acceptance.

---

Dr. Carlos Wexler

---

Dr. Peter Pfeifer

---

Dr. Haskell Taub

---

Dr. Giovanni Vignale

---

Dr. Steven Neal

## ACKNOWLEDGMENTS

To Carlos Wexler; few advisers would have given me so much freedom while tolerating my stubbornness so well, I would not have done so well without you. To Peter Pfeifer, who has likewise afforded me a large amount of trust. To Haskell Taub, who has been invaluable both to my writing and to my relatively quick introduction to a very complex field. To Steven Neal, who first demonstrated to me the joy of pure science. To Bahram Mashhoon, who has an uncanny knack for making difficult subjects simple, but still made me work harder than I ever have in any other class. To Giovanni Vignale, who has been like another adviser to me, taught me a lot of things about beautiful and expository writing, and demonstrated by example the value of hard work.

To all my colleagues in ALL-CRAFT; I could not accomplish my work without the benefit of partaking of the fruits of your hard labor. To all of the other colleagues who have assisted me, often in my pursuit of some piece of experimental data: Bogdan Kuchta, Lucyna Firlej, Philip Llewellyn, Delphine Phanon, Matt Stone, and Enrique Robles.

To all of my fellow graduate students, for hours of companionship, from time spent working together to drinks on the roof. Especially to Monika Golebiowska, without your special combination of understanding, gentle prodding, and reminders to ‘stop thinking about physics,’ I would have missed out on many of these experiences.

To my dad, Reed, for always telling me to ‘live up to my full potential.’ To my mom, Lorraine, for spending 18 years yelling at me and still ending up at my best friend. To my brother, Brett, for all those years getting into trouble together; I hope we can do it again someday. To my baby brother, Cullam, for naps on the couch, twirl hugs, and never getting a bit less cute. To everyone at Wilkes Boulevard United Methodist, for providing me with a home, and a place to pray and sing.

# TABLE OF CONTENTS

ACKNOWLEDGMENTS . . . . .	ii
LIST OF TABLES . . . . .	v
LIST OF FIGURES . . . . .	vi
ABSTRACT . . . . .	viii
CHAPTER . . . . .	
<b>1 Introduction . . . . .</b>	<b>1</b>
<b>2 Best Methods for Determining the Coverage-Dependent Isosteric Heat of Adsorption for a Hydrogen Adsorbate . . . . .</b>	<b>9</b>
2.1 Introduction . . . . .	9
2.2 Adsorption isotherms . . . . .	12
2.3 Clausius-Clapeyron equation . . . . .	16
2.4 Hydrogen adsorbed on nanoporous carbon . . . . .	24
2.4.1 Experimental Methods . . . . .	24
2.4.2 Results . . . . .	27
2.5 Summary . . . . .	33
<b>3 Calculation of Theoretical Inelastic Neutron Scattering Spectra from Hydrogen Adsorbed in Slit-Shaped Pores . . . . .</b>	<b>35</b>
3.1 Introduction . . . . .	35
3.2 Energy Levels and Wavefunctions of Adsorbed H <sub>2</sub> . . . . .	39
3.3 Scattering Cross Section . . . . .	44
3.4 Results . . . . .	49
3.5 Summary . . . . .	54

<b>4</b>	<b>Analysis of Experimental Inelastic Neutron Scattering Spectra from Hydrogen adsorbed in Carbon Adsorbents . . . . .</b>	<b>56</b>
4.1	Introduction . . . . .	56
4.2	Experimental Methods . . . . .	58
4.3	Data Analysis . . . . .	60
4.4	Results . . . . .	66
4.5	Summary . . . . .	74
<b>5</b>	<b>Anomalous Characteristics of a PVDC Carbon Adsorbant . . . . .</b>	<b>77</b>
5.1	Introduction . . . . .	77
5.2	Samples . . . . .	79
5.3	Structural Characterization . . . . .	82
5.4	Thermodynamic Characterization . . . . .	88
5.4.1	Hydrogen Adsorption . . . . .	88
5.4.2	Isosteric Heat . . . . .	91
5.5	Discussion . . . . .	92
<b>6</b>	<b>Summary and concluding remarks . . . . .</b>	<b>97</b>
	<b>BIBLIOGRAPHY . . . . .</b>	<b>107</b>
	<b>VITA . . . . .</b>	<b>121</b>

## LIST OF TABLES

Table	Page
1.1 Current hydrogen storage capabilities . . . . .	4
2.1 Experimental sample characteristics . . . . .	25
2.2 Samples with unusual adsorption and isosteric heat characteristics . .	33
4.1 Debye-Waller factors. . . . .	72
5.1 Sample characteristics, including densities . . . . .	83
5.2 Adsorbate densities . . . . .	90

## LIST OF FIGURES

Figure	Page
2.1 Schematic of adsorption in idealized pore . . . . .	14
2.2 Different types of adsorption isotherms and effect on isosteric heat . .	20
2.3 Effect of assumptions in determining isosteric heat . . . . .	21
2.4 Experimental pore size distributions . . . . .	26
2.5 Experimental excess hydrogen adsorption isotherms . . . . .	26
2.6 Effect of fit window size on isosteric heat . . . . .	28
2.7 Effect of type of fit on isosteric heat . . . . .	29
2.8 Effect of assumed film volume on isosteric heat . . . . .	30
2.9 Experimental isosteric heats calculated using best methods . . . . .	31
2.10 Isosteric heats calculated for other activated carbons . . . . .	31
3.1 Experimental INS spectra from the literature . . . . .	37
3.2 Adsorption potentials and energy levels in representative pores . . . .	42
3.3 Roto-vibrational transition energies as a function of pore size . . . . .	45
3.4 Form factors for representative pores . . . . .	48
3.5 Debye-Waller factor as a function of pore size . . . . .	49
3.6 Calculated INS spectra in representative pores . . . . .	50
3.7 Calculated INS spectrum in sample with uniform distribution of pores	53
4.1 Representative INS spectra . . . . .	61

4.2	Peak intensity as a function of energy/momentum transfer . . . . .	62
4.3	Spectrum after subtraction of fit to free recoil . . . . .	65
4.4	Separated spectra for nanotube sample . . . . .	67
4.5	Spectra for all samples . . . . .	69
4.6	Separated spectra for all samples . . . . .	70
4.7	Q dependence of the different peaks. . . . .	71
4.8	Areal absolute adsorption isotherms . . . . .	73
4.9	Separated spectra for all samples . . . . .	74
5.1	Room temperature excess hydrogen isotherms . . . . .	78
5.2	Pore size distributions . . . . .	83
5.3	SEM images. . . . .	85
5.4	TEM images. . . . .	87
5.5	Cryogenic excess hydrogen isotherms . . . . .	88
5.6	Areal absolute hydrogen isotherms . . . . .	90
5.7	Isosteric heats calculated from isotherms and measured by calorimetry	91
5.8	Effects of a variable number of adsorption sites . . . . .	94
6.1	Representative pore shapes. . . . .	101
6.2	Adsorption model . . . . .	102
6.3	Isotherms which allow multiple occupation . . . . .	104
6.4	Localized or mobile adsorption . . . . .	105

## ABSTRACT

For convenient use of energy, it is common to use chemical potential energy stored in a fuel. To reduce pollution, a desirable fuel is molecular hydrogen, whose only byproduct is water vapor. However, there are still many obstacles that must be overcome for it to become widely used; the most significant is its storage. Despite having high energy content per by weight, hydrogen has very low energy content per volume, traditionally requiring high pressures and/or low temperatures to store. One proposed method is via physical adsorption to some high surface area material. However, current materials are still far from meeting Department of Energy goals.

This work discusses improvements to some traditionally less reliable techniques used to characterize adsorbants. The isosteric heat of adsorption, which is the heat released by hydrogen as adsorbed, is an important value because of its relation to the binding energy. It can be estimated from adsorption isotherms or measured directly, but each methods is of limited applicability and requires care to determine accurately. Inelastic neutron scattering is a technique which scatters neutrons from the adsorbed hydrogen molecules, with the resultant energy loss giving direct information about the quantum states. This work establishes a theoretical basis for improved analysis of the spectra and applies it to experimental data.

A case study is presented on a sample with quite high adsorption for its surface area, both at cryogenic and room temperatures, which also has a number of other unusual characteristics. The experimental data for the sample does not fit with classical adsorption theory, suggesting some new phenomena at work. Several hypotheses are presented. One, which takes advantage of the bosonic nature of the composite molecular hydrogen particle, seems to be the most able to offer a complete explanation for the behavior of the sample.

# Chapter 1

## Introduction

For the convenient use of energy, some method of storage must be used. For much of human history, that method has been to use the chemical potential energy stored in some fuel. This fuel can then be used at the time and place of the user's choosing through the process of combustion, which is the exothermic chemical reaction between oxygen and the fuel which results in the release of carbon dioxide, water, and other compounds, along with heat which can then be used to produce work. For the past two centuries since the discovery of petroleum distillation by Lukasiewicz [1], the most useful fuels have been hydrocarbons, due to their relatively inexpensive availability and high energy density. If a hydrocarbon is completely combusted, the only byproducts released are heat, water, and carbon dioxide.

In today's modern world, such large amounts of energy are used that availability is beginning to be an issue [2]. In addition, the large amount of carbon dioxide released can have a significant effect on the environment [3]. The use of hydrogen bypasses the latter problem neatly, as the byproducts of combusting this fuel include only water and heat. However, there are many significant obstacles that must be overcome for this idealized situation to become reality. For instance, efficient ways must be found

to produce hydrogen and engines must be developed to use it. However, the most significant issue is in its storage [4].

While the carbon components of a hydrocarbon fuel are not essential to the actual combustion process itself, and generally act to create additional polluting combustion byproducts, they are essential for the efficient storage of the fuel. The strong chemical bonds between the carbon and hydrogen atoms hold the hydrogen in a reasonably small volume. By itself, hydrogen requires a much larger volume to store. Hydrogen becomes a liquid only at the impractically low temperature of 20.28 Kelvin [5]. Even at this density, there is actually less hydrogen in a given amount of liquid hydrogen than the same volume of gasoline. The situation is even worse for the more practical case of storage at room temperature, which would not require the use of on-board cooling. The ideal gas law gives the density  $\rho$  of a gas of molecules with molar mass  $m$  as

$$\rho = \frac{mP}{RT}, \quad (1.1)$$

where  $P$  is the pressure,  $T$  is the temperature, and  $R$  is the gas constant. Because hydrogen has the smallest molar mass of any molecule, the volume to store a given amount of available energy is larger than for any other fuel at a given temperature and pressure. Of course, the density can always be increased by increasing the pressure, but this comes with a number of attendant practical concerns. Significant mass must be added to the tank to safely store gas at an increased pressure, and the high pressure also creates additional safety concerns. The Missouri University Science and Technology in Rolla, Missouri has a hydrogen fueling station and shuttle bus which runs on compressed hydrogen stored at a pressure of 350 bar [6]. Even at this pressure, the tank takes up nearly half of the volume of a vehicle, leaving room for only 12 passengers.

Because the goal of hydrogen fuel is so desirable, the Department of Energy has set targets [4, 7] for 2015, given in Table 1.1, that they believe would make the use of hydrogen for mobile applications feasible, but which still allow significantly more mass and volume to store the same amount of energy as a given amount of gasoline. These targets also include the ability for the system to operate over a range of ambient temperature conditions up to pressures of only 100 bar, and for refueling to take only 2.5 minutes. Many alternative storage techniques have been proposed which fall into two main classes. One is to store the hydrogen via some chemical process which allows the hydrogen to be released on demand and then burned by itself. Generally these require some method to release the hydrogen, such as increased temperature, as well as high pressure or the use of a catalyst to refuel, creating additional complications in the design of tanks and refueling stations [4]. A more simple and desirable alternative is to adsorb the hydrogen via Van der Waals forces to an adsorbant material with a high surface area, such as activated carbon. The Alliance for Collaborative Research in Alternative Fuel Technology (ALL-CRAFT) [8] at the University of Missouri has recently produced competitive activated carbons from a corncob precursor with surface areas of up to  $3100 \text{ m}^2/\text{g}$  and storage capacities of up to  $100 \text{ g H}_2/\text{kg C}$  at temperatures of  $77 \text{ K}$  and pressures of  $90 \text{ bar}$  [9] and this work discusses this method of physisorption in depth. However, as Table 1.1 shows these activated carbons are still very far from meeting the goals. Clearly significant research is needed to make progress in this field.

When striving for a significant new experimental result, there are two main paths one might tread. Firstly, one might propose some new or improved method based on theory, and then attempt to reach this goal experimentally. While historically many new results have been obtained by this method, it is also possible to spend a lot of time on this process without reaching the goal. Currently, there have been no major theoretical advances in the theory of hydrogen adsorption onto weakly

Table 1.1: Mass and volume of 15 gallons of gasoline and an amount of hydrogen containing an equal amount of usable energy, where the hydrogen is stored by various systems. \*At room temperature and 100 bar.

	mass (kg)	volume (L)
gasoline, 15 gallon tank	41	57
compressed hydrogen*	13	1,580
liquid hydrogen ( $T=20$ K)	13	185
2015 DOE target*	158	161
adsorbed in activated carbon*	590	1,480

binding substrates, thus generally the goal has been to invent materials with increased surface area or binding energy. Conferences in this field are often theory-heavy, with much discussion of topics like quantum chemical calculations which find improved binding energies for a wide variety of chemically modified adsorbants [10]. However, experimental methods to produce these chemical structures are often out of practical reach, and even when achieved, theoretical predictions may turn out to have been overly optimistic. But theoretical work of this type is relatively inexpensive and the attractiveness of a solution to the problem makes this path continue to be desirable. The main difficulty is in choosing which of the many theoretical options proposed is worthy of the more expensive experimental work. If significant experimental advances continue to remain out of reach, at some point in the future theoretical predictions based merely on small modifications of well-known theory are likely to lose their appeal.

The second path is to serendipitously achieve a new and desirable experimental result which is not well explained by the current theory. If some new theory can then be derived to explain that result, it may reveal a technique to create an even more impressive experimental result. Nature often provides options which are unlikely to occur to a theorist with no provocation. Of course, one must be lucky enough to

stumble across the trailhead and astute enough to recognize it, but once the unusual experimental result has been achieved it is possible for research carried out with the proper detective spirit to make accelerated progress. Fortuitously, ALL-CRAFT has achieved just such an experimental result (discussed in Chapter 5).

In order to understand the performance of samples, a number of characterization techniques are used. Hydrogen adsorption obviously gives the overall performance of the sample. However it is often also done at cryogenic temperatures even if storage is not planned at this temperature, because further information about the material can be obtained via this method [11]. The next most commonly used characterization technique is nitrogen adsorption [12]. Nitrogen is liquid at 77 Kelvin and 1 atmosphere and isotherms are taken at 77 K and pressures up to 1 atmosphere. The excess amount of nitrogen which has liquefied in the micropores of the sample at 0.995 atm gives the micropore volume. More sophisticated analysis of the adsorption isotherm at lower pressures gives the surface area and even a pore size distribution, though this is quite model dependent [13, 14]. These are well-understood techniques which have been at use for many years. However, nitrogen adsorption is unable to probe the smallest pores because of the larger size of  $N_2$  as compared to  $H_2$ , and offers only general information about pore structure. While useful, these common characterization techniques do not provide enough information to understand any new adsorption phenomena.

There are other less common characterization techniques which, while having a long history, have still not reached the same level of reliability. The isosteric heat or enthalpy of adsorption, which is the heat released by the hydrogen as it undergoes the adsorption process, is an important value because of its relation to the binding energy. It can be estimated from hydrogen adsorption isotherms or measured directly via calorimetry, but both of these methods are difficult and prone to error. Inelastic neutron scattering is a technique which scatters neutrons from the hydrogen molecules

as they occupy the adsorption sites, with the resultant energy loss giving information about the quantum states. However, analysis of the spectra is quite difficult and so far only very general information about the homogeneity of the adsorption sites has been obtained from this method. This bulk of this work discusses some advances which have been made in these less common characterization techniques. Then a case study is presented on ALL-CRAFT's unusual sample and all of the characterization techniques are used to explore its performance.

Chapter 2, entitled "Best Methods for Determining the Coverage-Dependent Iso-steric Heat of Adsorption for a Hydrogen Adsorbate," has been submitted for publication in the journal *Langmuir* [15]. This chapter begins with a theoretical section which reviews and defines the different types of adsorption isotherms currently in common use and discusses the correct calculation of the isosteric heat of adsorption from these isotherms. A number of unphysical experimental isosteric heat results from the literature are discussed and some possible reasons for the wide variety of unusual results are given. A robust procedure for determining both the isosteric heat and the volume of the adsorbed film solely from experimental cryogenic hydrogen adsorption data is proposed, and experimental data from ALL-CRAFT is used as a demonstration. Correct data fitting methods are also discussed.

Chapter 3, entitled "Calculation of Theoretical Inelastic Neutron Scattering Spectra from Hydrogen Adsorbed in Slit-Shaped Pores" was published under the title "Sub-Nanometer Characterization Of Activated Carbon by Inelastic Neutron Scattering" in the journal *Carbon* in December of 2010 [16]. This chapter introduces the use of inelastic neutron scattering (INS) as a pore characterization technique which uses the adsorbate molecules themselves as the probe, thus obtaining highly accurate information about the actual quantum states which the hydrogen molecules occupy when adsorbed. Adsorption potentials, wavefunctions, transition energies, and INS spectra are calculated for slit-shaped pores of variable size and are shown to be highly

variable for pores under 9 Å in width. While other similar works in the literature have used more sophisticated techniques or more reasonable pore models, this paper addresses several new issues which have turned out to be invaluable in the analysis of experimental data. Firstly, whereas previous works [17–19] have calculated only the energies of rotational excitations, this work also calculates the energies of roto-vibrational excitations, allowing for more robust interpretation of experimental spectra. Secondly, the inherent anisotropy of the problem, which in previous works has been used solely for calculating the splitting of the rotational transitions, has been robustly accounted for in both the Debye-Waller values and the form factors, calculations which were based on a proof that the molecular axis of the excited rotational state tends to be aligned with the momentum transfer.

Recently collected experimental INS spectra from hydrogen adsorbed in several different carbon based adsorbents is presented in Chapter 4, entitled “Analysis of Experimental Inelastic Neutron Scattering Spectra from Hydrogen adsorbed in Carbon Adsorbents.” A shortened version of this chapter is in preparation for submission to the journal *Physical Review Letters*. The most significant difference between the experimental and theoretical spectra is the presence of transitions between the expected rotational and roto-vibrational peaks which we have ascribed to excitations of the translational motion of the hydrogen molecules parallel to the adsorption plane. Despite initially appearing to be simply a nuisance background signal which must be removed in order to analyze the main peaks, it is shown that in fact these free recoil transitions can be used to separate the experimental spectra into two parts, where the momentum transfer is either parallel or perpendicular to the adsorption plane. Not only does this analysis seem to suggest that the diffusive behavior of adsorbed hydrogen molecules along the adsorption plane is highly dependent on their molecular spin state, but a particular sample whose spectra initially seemed to be explained by a significant heterogeneity, is shown to in fact have significantly different spin behavior.

This sample is discussed in depth in Chapter 5, entitled “Anomalous Characteristics of a Saran Carbon Adsorbant.” This chapter is in preparation for submission to the journal *Carbon*. This sample is of high interest, not only because of its anomalously high hydrogen uptake, but because every single experiment which is performed on it has highly unusual results. While one unusual result or two may simply suggest some type of user error, the correlation of all of these results, which are difficult to explain using classical adsorption theory, suggests that there may be some novel adsorption phenomenon at work in this sample. Some qualitative hypotheses are presented.

Finally, a summary of this work is presented in Chapter 6. The hypothesis of the novel hydrogen adsorption phenomena which I consider to be both the most effective at explaining all of the experimental data most consistently as well as offering the most likely possibility for further improvement is discussed in more depth. It is made clear that extensive theoretical and experimental work remains to be done in this area, but there also appears to be an exciting possibility for a solution to the problem of hydrogen storage.

# Chapter 2

## Best Methods for Determining the Coverage-Dependent Isosteric Heat of Adsorption for a Hydrogen Adsorbate

### 2.1 Introduction

The isosteric heat or enthalpy of adsorption is equal to the magnitude of the change in energy upon adsorption, plus the amount of work done to compress the adsorbed molecules to a smaller volume. Although it is possible to measure this quantity directly, the experiment is quite delicate. Thus it is typically calculated using the Clausius-Clapeyron equation [11, 20, 21], which compares experimental adsorption isotherms at nearby temperatures. The isosteric heat is equal to the binding energy plus an offset, which depends on factors such as the vibrational frequencies of the adsorbed molecules and their specific volume. Because of its relation to the binding energy, the isosteric heat is an important experimental measurement that, along with surface area and pore volume, allows for full characterization of a sample. Often, only

one value for the isosteric heat is reported, typically corresponding to low coverage. However, because this value is only for the pores with the highest binding energies which are preferentially filled at low coverage, it can often mislead as to the full performance of the sample. Instead, it is desirable to calculate the isosteric heat over the entire range of interest. Unfortunately, common assumptions used for its determination may not be correct, and important sources of error lurk at both low and high coverage. This chapter addresses the main sources of error in the determination of isosteric heats from experimental hydrogen adsorption isotherms and describes the best methods to minimize their impact.

One of the most common sources of error comes from the improper use of excess adsorption or total storage isotherms (which include adsorbate molecules in the gas phase) to calculate the isosteric heat. In Section 2.2 we will demonstrate that absolute adsorption isotherms should be used instead for correct results. Using the incorrect isotherms affects the results significantly, particularly at high coverage. Using the excess adsorption results in isosteric heats which rise at increasing coverage, an unphysical result suggesting that sites with higher binding energy are filled last. A number of papers in the literature show isosteric heats that rise as a function of coverage for simulated [22–24] and experimental [25–32] data, suggesting that the excess adsorption was incorrectly used. Conversely, using the total storage results in isosteric heats which drop too quickly [24, 33–37], usually resulting in unusually low heats at high coverage.

To correctly calculate the isosteric heat, the absolute adsorption must be calculated from the excess adsorption. Methods which are currently used include assuming that the adsorbed film is at the liquid density [25, 37–39] or making the thickness of the film proportional to the surface area [40, 41]. However, these methods do not take into account the effects of the adsorption potential, which can act to increase the film density beyond the liquid density by causing adsorbed molecules to be closer together

along the surface of the adsorption plane, while broadening the width of the adsorption layer due to its finite size. In Section 2.3 we will show that the volume of the film may be estimated by assuming the thermodynamic condition that the isosteric heat should fall to a constant at high coverage. This procedure gives a lower bound to the volume of the adsorbed film, based solely on experimental data. In Section 2.4.2, by making the assumption of adsorption on a nominally flat surface, we estimate that the width of the adsorption layer for hydrogen adsorbed on several activated carbons is  $\approx 5 \text{ \AA}$ , which is in good agreement with simulations [42].

Several other issues can significantly affect the determination of isosteric heats. Pan et al. [43] have reviewed the assumptions that are used to derive the Clausius-Clapeyron equation and find that for room temperature adsorption of methane, using the real specific volume of the adsorbed film is an important correction at high coverage; we find the same result for cryogenic adsorption of hydrogen. Additionally, in Section 2.4.2 we show how critical the fitting procedures used to numerically calculate the isosteres is in the determination of correct isosteric heats, with an incorrect fit increasing the heat by up to 5 kJ/mol.

We show experimental data for hydrogen adsorbed on carbon in Section 2.4.1. Then, in Section 2.4.2 we discuss a set of best methods to calculate isosteric heats and apply them to the experimental data. The resultant isosteric heats range from 6–3 kJ/mol over the full range of coverage, quite comparable between our different samples, as well as similar carbon samples in the literature [44, 45]. However, one sample which has a number of unusual features is discussed and compared with similar samples in the literature.

## 2.2 Adsorption isotherms

Adsorption isotherms can be given in terms of absolute adsorption, excess adsorption, or total storage. The absolute adsorption gives the number of adsorbate molecules that are actually adsorbed to the surface. The excess adsorption is the excess amount of adsorbate present in the pores above the gas density. The total storage includes all of the adsorbate present in the pores, whether or not it is adsorbed. (See Figure 2.1.) We will now discuss these different isotherms in detail.

Absolute adsorption includes the adsorbate molecules which are held near the surface at a higher density than the gas phase by an adsorption potential. Theoretically, absolute adsorption is calculated using some particular model. We have chosen to use the Langmuir-Freundlich [46] adsorption isotherm, which is given as

$$\theta_a = \frac{(\chi P)^c}{1 + (\chi P)^c}, \quad (2.1)$$

where  $\theta$  is in dimensionless units of fractional coverage and gives the probability that an adsorption site is occupied. When  $c = 1$ , this reduces to the Langmuir isotherm, which has the advantage of following Henry's law  $\theta \propto P$  at low pressure, but does not generally describe heterogeneous adsorbents well.

Adsorption isotherms are typically reported in units of grams of adsorbate, per kilogram of adsorbent. To go between these units and units of fractional coverage, the following expression is used,

$$m_a = \theta_a \frac{\Sigma m}{\alpha N_a}, \quad (2.2)$$

where  $m_a$  is the specific absolute adsorption,  $m$  is the molar mass of the adsorbate,  $N_a$  is Avagadro's number, and  $\Sigma$  is the surface area of a kilogram of adsorbent, which is typically measured by nitrogen adsorption. The surface area per adsorption site,

$\alpha$ , must also be known. For hydrogen adsorbed on graphite, this value has been measured using low temperature diffraction studies as  $10.7 \text{ \AA}^2$  [47].

The absolute adsorption is not experimentally accessible by any direct means. Instead, what can be most easily measured is the Gibb's excess adsorption [11,21,48,49], which is defined as the absolute adsorption minus the amount that would be in the adsorption site at the gas density. If the volume of the adsorbed film is known, the absolute adsorption as well as the density of the film can be calculated using

$$m_a = m_e + \rho_g V_a = \rho_f V_a, \quad (2.3)$$

where  $\rho_g$  is the gas density,  $\rho_f$  is the film density,  $V_a = \Sigma l$  is the volume of the adsorbed film, and  $l$  gives the proportionality factor between the surface area and film volume. If the adsorption surface is assumed to be nominally flat,  $l$  can be interpreted as the width of the adsorbed film. Figure 2.1 gives a pictorial representation of the density of the center of mass of adsorbate molecules inside of an idealized pore of width  $w$ . The pore begins one adsorbent molecular radius away from the center of mass of the molecules which compose the surface. In the adsorption layer, the adsorption potential results in a high density, with  $l$  being the width of this film. The molecules which are in region I represent the excess adsorption, while the absolute adsorption contains the molecules in both regions I and II. Between the adsorption layers in region III, over a width  $w - 2l$ , molecules are at the gas density.

Sircar [21] has shown that excess quantities may be used in place of absolute quantities with no significant error as long as  $\rho_g/\rho_f \ll 1$ . While there are many cases where this condition is met, for cryogenic hydrogen adsorption  $\rho_g/\rho_f = 0.1$  at a pressure of 5.5 bar. Current interest in medium to high pressure sorption characteristics makes it necessary to work beyond this regime.

Calculating the absolute from the excess is a difficult task as  $V_a$  is not generally a

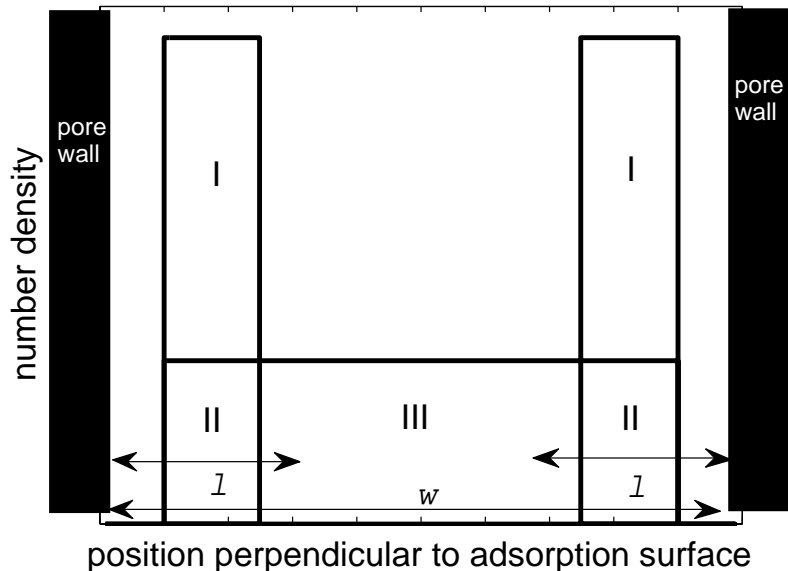


Figure 2.1: A schematic representation of the density inside of an idealized slit pore of width  $w$ . There are two adsorption layers, each with width  $l$ , which contain molecules at a high adsorption density. The molecules in regions I and II represent the theoretical absolute adsorption, while the molecules above the gas density in region I represent the excess adsorption. The total storage also includes the molecules in region III which are not adsorbed, but simply present in the pore at the smaller gas density.

quantity which can be measured. To get an estimate, we can look at simulations of adsorption. However, in contrast to the idealized situation in Figure 2.1, it is difficult to define exactly where the adsorption layer ends [22]. In addition, there is significant variation of these values with pore size and shape. For reference, simulations of hydrogen in slit-shaped carbon pores estimate that  $l \approx 3\text{--}6 \text{ \AA}$  [42].

Even though excess and absolute adsorption have been commonly used terms in adsorption theory for many years, there is still a great deal of confusion in the literature about how they can be related. A number of authors [25, 38–40] use some equation of the form,

$$m_v = \frac{m_e}{(1 - \rho_g V_a \theta_a / m_a)}, \quad (2.4)$$

which differs significantly from Eq. 2.3. In essence, Eq. 2.4 assumes that the volume of the adsorbed film varies with coverage and is given by  $\theta V_a$ ; this includes only the

part of the adsorption layer which is currently occupied. However, it is simple to show that this expression is incorrect. Let us take a surface that has an adsorption potential of exactly zero. By definition, in this case the excess adsorption should be zero. While it may be a bit of a misnomer to use the term "absolute adsorption," seeing as how there is no adsorption potential, if we think of the absolute adsorption as simply giving the density of molecules near the surface, we can see that in this case the "adsorbed" density is equal to the gas density. Using Eq. 2.3, we find that indeed  $m_a = \rho_g V_a$  when  $m_e = 0$ . However, using Eq. 2.4 we find that  $m_v = 0$  when  $m_e = 0$ ; therefore  $m_v$  can not be the absolute adsorption. Though it does not correspond to any useful theoretical or experimental value, we will refer to this quantity as the *variable volume* adsorption to reflect the fact that the film volume is taken to vary with coverage in this equation.

Another equation which is often used [23, 24] to calculate the absolute from the excess is

$$\theta_t = \theta_e + \rho_g V_p N_a, \quad (2.5)$$

where  $V_p$  is the volume of the entire pore, not just the fraction of the pore volume in which adsorption occurs. This value has been referred to previously [9] as the total storage and we will continue with that convention. Returning again to Eq. 2.1, this quantity includes molecules which are in regions I, II, and III. This quantity is certainly useful, as it gives the total amount of gas inside the pores of the sample and can also be easily found experimentally, with  $V_p$  typically measured by subcritical nitrogen adsorption. However, it does not correspond to the absolute adsorption, as it contains many molecules which are merely at the gas density.

## 2.3 Clausius-Clapeyron equation

The Clausius-Clapeyron equation is typically used to calculate the isosteric heat of adsorption by comparing two (or more) different adsorption isotherms, taken at closely adjacent temperatures,  $T_1 < T_2$ . The isosteric heat is given as a function of absolute coverage [11, 20],

$$\Delta h(\theta) = \frac{RT_1T_2}{T_2 - T_1} \ln \left[ \frac{P_2(T_2, \theta)}{P_1(T_1, \theta)} \right], \quad (2.6)$$

where  $P(T, \theta)$  is the pressure at which the coverage is  $\theta$  for a given temperature  $T$ . In order to discuss the effects of using the wrong adsorption isotherms and examine the assumptions built into this equation, we will show how it is derived.

It is assumed that the adsorbed phase and the gas phase are in equilibrium, meaning that their chemical potentials are equal,  $\mu_g(\theta) = \mu_a(\theta)$ . Because this is true at any point along the isotherm, their derivatives are also equal,  $d\mu_g = d\mu_a$ . Using the Gibbs-Duhem equation, we may write

$$v_g[T, P(T, \theta)]dP + s_g[T, P(T, \theta)]dT = v_a(\theta)dP + s_a(T, \theta)dT. \quad (2.7)$$

The differential enthalpy is given by

$$\Delta h(\theta) = T\Delta s(\theta) = T[s_g(T, P(T, \theta)) - s_a(T, \theta)], \quad (2.8)$$

where  $\Delta h$  is the difference in specific enthalpy between the gas phase and the adsorbed phase, also known as the isosteric heat of adsorption. This value may be understood as the heat released by the adsorption process, which is equal to the change in energy minus the amount of work done to compress the adsorbed molecules to their new volume. Substituting this expression in Eq. 2.7 and rearranging, the Clausius-Clapeyron

relation is obtained

$$dP[v_g(T, \theta) - v_a(\theta)] = \Delta h(\theta) \frac{dT}{T}. \quad (2.9)$$

At this point, the gas is assumed to be ideal, with  $v_g(\theta) = RT/P(T, \theta)$ . Additionally, the specific volume of the adsorbed phase is assumed to be much smaller than the specific volume of the gas phase,  $v_a(\theta) \ll v_g(\theta)$  such that it may be set to 0. With these substitutions, the relation becomes

$$Rd(\ln P) = -\Delta h d(1/T). \quad (2.10)$$

This expression may be integrated to obtain the Clausius-Clapeyron equation (Eq. 2.6), as long as  $\Delta h$  is constant. Experimental data has generally found the isosteric heat to vary little with temperature for many types of systems [50]. Referring to Eq. 2.8, the first term can be taken as constant so long as the changes in temperature and pressure are small. The second term can only be taken as constant so long as  $\theta$  also remains constant. We assert that the absolute adsorption is the quantity which should remain constant, rather than the excess adsorption or total storage. Referring again to Figure 2.1, the division of molecules into region I and II is theoretically arbitrary, as there is no difference in the position, energy, or entropy of the molecules in these two regions. This division is made only because of experimental convenience. If instead of holding  $\theta_a$  constant,  $\theta_e$ ,  $\theta_t$ , or  $\theta_v$  is held constant, the number of molecules in the adsorption layer and thus their entropy will not be constant and Eq. 2.6 will give an incorrect isosteric heat, as we will show below.

Other authors [43,51,52] have looked at assumptions used in deriving the equation, such as that the gas is ideal and that the specific volume of the adsorbed phase can be taken as zero. To do this, Eq. 2.9 is rearranged using the chain rule,

$$\Delta h(\theta) = T[v_g(T, \theta) - v_a(\theta)] \frac{(\partial\theta/\partial T)_P}{(\partial\theta/\partial P)_T}, \quad (2.11)$$

and actual values for  $v_g$  and  $v_a$  are used. Pan et al. [43] found that for adsorbed alkanes at room temperature, the ideal gas assumption was found to result in a negligible error, while the actual volume of the adsorbed film was an important factor at high coverage. When using this equation with isotherms at two different temperatures  $T_1$  and  $T_2$ , we have calculated the isosteric heat using the data at one temperature,  $(\partial\theta/\partial P)_{T_1}$  and the gas volume at the same temperature  $v_g(T_1, \theta)$  and averaged with the isosteric heat calculated using the data and gas volume at  $T_2$  to find the end result. We shall refer to values calculated with this method as the ‘assumptionless isosteric heat.’

To demonstrate the effects of using the incorrect adsorption quantity, we consider first a simple theoretical model of an idealized homogeneous surface with no interaction between the adsorbate molecules, using discrete adsorption sites with a typical binding energy for a graphite surface [53].

The Langmuir adsorption isotherm gives the coverage as

$$\theta = \frac{\chi(T)P}{\chi(T)P + 1}, \quad (2.12)$$

where  $\chi(T)$  is known as the Langmuir constant. When  $\chi(T)P \ll 1$ , the isotherm can be approximated as a linear function

$$\theta \approx \chi(T)P. \quad (2.13)$$

The Clausius-Clapeyron relation can be rewritten as

$$\frac{d(\ln(P))}{d(1/T)} = \frac{-\Delta h}{R}. \quad (2.14)$$

Replacing  $P = \theta/\chi(T)$  and holding  $\theta$  constant, the isosteric heat as a function of the

Langmuir constant can be written as

$$\Delta h = R \frac{d(\ln(\chi(T)))}{d(1/T)}. \quad (2.15)$$

Theoretical isotherms were calculated using the localized adsorption model [54], which treats the adsorbed layer as consisting of independent adsorption sites of fixed size. Adjacent molecules are assumed to not interact with one another. The motion parallel to the plane is assumed to be that of a harmonic oscillator, with vibrational frequency  $\nu$ . The Langmuir constant is given by

$$\chi(T) = \frac{\exp(-E_b/RT)}{\sinh(h\nu_z N_a/2RT) \sinh(h\nu_x N_a/2RT) \sinh(h\nu_y N_a/2RT)} \frac{h^3}{\sqrt{(8\pi m)^3 (kT)^5}}, \quad (2.16)$$

The isosteric heat for localized adsorption is then given by

$$\Delta h(T) = E_b - \coth\left(\frac{h\nu_z}{2kT}\right) \frac{h\nu_z N_a}{2} - \coth\left(\frac{h\nu_x}{2kT}\right) \frac{h\nu_x N_a}{2} - \coth\left(\frac{h\nu_y}{2kT}\right) \frac{h\nu_y N_a}{2} + \frac{5}{2} RT. \quad (2.17)$$

The binding energy is typically  $E_b = 5$  kJ/mol [53]. At a temperature of 80 K, the term  $\frac{5}{2} RT$  is equal to 1.66 kJ/mol and, using an estimated value of  $\nu_z = \nu_x = \nu_y = 3 \times 10^{12}$  Hz [9, 54], the terms of the form  $\coth(h\nu_z N_a/2RT) h\nu_z N_a/2$  are equal to 0.84 kJ/mol. All of these terms are of the same order, but their net effect is that the isosteric heat is about 0.83 kJ/mol smaller than the binding energy. Theoretical absolute isotherms were calculated from the coverage using a surface area of  $\Sigma = 2630$  m<sup>2</sup>/g. Excess isotherms were calculated from absolute isotherms using Eq. 2.3 and a volume of the adsorbed film equal to  $V_a = \Sigma l$  where  $l = 4$  Å. Total storage isotherms were calculated from excess isotherms using Eq. 2.5 and a pore volume equal to  $V_p = \Sigma w$  where  $w = 6$  Å. Variable volume isotherms were also calculated using Eq. 2.4

For each type of isotherm, Eq. 2.6 was used to calculate the isosteric heat of adsorption. The results are shown in Figure 2.2. Because the surface is homogeneous

and interactions are ignored, the isosteric heat should be independent of coverage. Using the absolute adsorption, the expected result is obtained. However, using the excess or variable volume adsorption, the isosteric heat rises as a function of coverage, becoming divergent at the maximum of the excess adsorption. Conversely, using the total storage, the isosteric heat drops as a function of coverage.

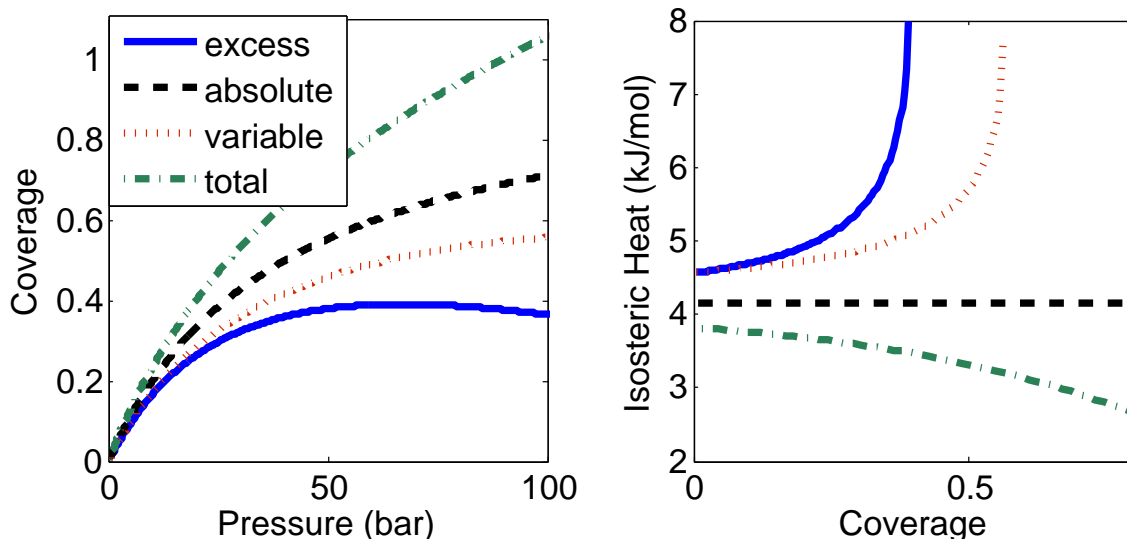


Figure 2.2: (Left) Absolute, excess, variable volume adsorption, and total storage at 90 K for localized Langmuir adsorption on a homogeneous surface with no interaction between adjacent adsorbate molecules. Coverage at 80 K (not shown) was also calculated. (Right) Isosteric heat calculated with Eq. 2.6 using the different adsorption variables. As expected, the isosteric heat calculated from the absolute adsorption is a constant function of coverage. When using any of the other adsorption variables, the isosteric heat changes with coverage.

Theoretical isotherms were also used to compare the isosteric heat calculated using the Clausius-Clapeyron equation to the isosteric heat calculated using the assumptionless Clausius-Clapeyron relation. The results are shown in Figure 2.3. Because the assumptionless isosteric heat calculated using the relation takes into account the changing specific volume of the film, it is not a constant function of coverage, unlike the isosteric heat calculated using the equation.

Often, the isosteric heat is calculated using low pressure data and only one value is reported [55]. In this regime, there is little difference between excess, absolute, and

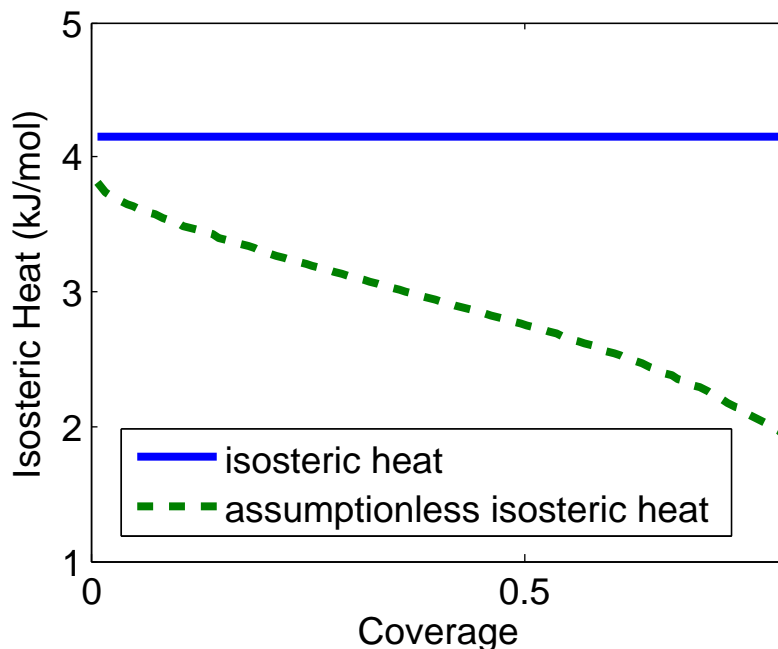


Figure 2.3: Isosteric heat calculated using the Clausius-Clapeyron equation or assumptionless Clausius-Clapeyron relation for a theoretical isotherm. The isosteric heat calculated using the Clausius-Clapeyron equation is a constant function of coverage, whereas the isosteric heat calculated using the assumptionless Clausius-Clapeyron relation is not constant, due to the changing specific volume of the adsorbed film.

total amount stored. However, for heterogeneous samples, a definition which encompasses most real samples, this gives results only for the sites with the highest binding energy, a partial and biased result which may mislead as to the overall expected performance of the sample. To characterize more of the binding sites, it is desirable to calculate the isosteric heat over the entire range of coverages using experimental data over a large pressure range. In this regime, the difference between different adsorption quantities affects the isosteric heat results significantly.

Theoretically, the isosteric heat should only rise as a function of coverage in the case of a homogeneous adsorbent where there are strong attractive forces between adsorbate molecules [56]. For supercritical adsorption on most real materials these conditions are not met, and isosteric heat should not rise as a function of coverage. There are several examples in the literature of isosteric heats calculated using simu-

lated excess isotherms which rise as a function of coverage for hydrogen or methane adsorbed on carbon [22–24]. Because simulations typically result in data on a single pore size and shape, the effects of using the wrong quantity to calculate the isosteric heat can be seen explicitly, without the complication of pore heterogeneity. There are also a large number of cases where reported isosteric heats determined from experimental data rise as a function of coverage [25–32]. Authors do not always provide enough details about their methods to be sure that the reason is an incorrect use of the excess adsorption in the isosteric heat calculation, but we assert that it is a likely explanation in most of these cases.

Isosteric heats calculated using simulated total storage isotherms are also reported in the literature [24, 33], and they are observed to drop off as a function of coverage for most pore types. For real adsorbents, heterogeneity is typically large enough that the isosteric heat should drop as a function of coverage as the pores with the highest binding energy are filled first, even when the correct absolute adsorption isotherms are used. However, beyond the smallest nanopores, surfaces are essentially independent with the binding energy changing very little as a function of pore size [42]. Therefore, for most real materials where there are a large distribution of pore sizes, one would expect the isosteric heat to fall off to the constant for an independent surface at high coverage. There are experimental examples in the literature where it is specified that the total storage (or absolute adsorption calculated using too large of a film volume) was used, and the resultant isosteric heat still has a significant negative slope at high coverage [34–37], often resulting in unusually low heats for the given system.

To correctly calculate the isosteric heat, the absolute adsorption must be calculated from the excess. Previous authors have used several approximations for  $V_a$ . One method [25, 37–39] is to assume that a full adsorbed layer at infinite pressure is at the liquid density.

$$V_a = \frac{m_a}{\rho_L}. \quad (2.18)$$

Another method [40,41] is to make the nominal width of the adsorbed film  $l$  proportional to the surface area per adsorption site.

$$l = d\sqrt{\alpha}, \quad (2.19)$$

where  $d$  depends on the packing geometry and pore geometry assumed. However, both of these methods suffer from several problems. Firstly, the adsorption potential often forces adsorbed molecules to be closer together than they might otherwise be, whether in the liquid or gas phase. Additionally, neither takes into account the width of the adsorption potential perpendicular to the adsorption plane. Values obtained from these methods range from  $l = 3.2 - 51 \text{ \AA}$  for hydrogen adsorbed on carbon. The lower bound [25] is likely too small as it is only about the size of a hydrogen molecule [42,57], whereas the upper bound [40] is certainly too large as it gives  $V_a > V_p$  for this sample, which is theoretically impossible.

We propose that the value of  $V_a = \alpha l$  may be estimated with experimental data by varying  $l$  and observing the changes in the isosteric heat calculated using the absolute adsorption  $\theta_a(l)$  of Eq. 2.3. For hydrogen on activated carbon, adsorbate interactions are not strong and the adsorbent is heterogeneous, therefore a rising isosteric heat indicates that  $l$  is too small. Conversely, if  $l$  is too large, the isosteric heat would always drop as a function of coverage (though this may also be caused by a particularly heterogeneous sample). Thus we will look for the value of  $l$  where the isosteric heat falls to a constant value at high coverage, which will give a lower bound for the actual value of  $l$ .

## 2.4 Hydrogen adsorbed on nanoporous carbon

We now consider the application of the arguments and methods presented in the previous sections. Three different samples will be considered in this study: (i) Sample AX-21 MSC-30, a commercially available activated carbon with high surface area and a large proportion of nanopores; (ii) Sample 3K, a KOH activated carbon from a carbonized corncob precursor; and (iii) Sample HS;0B, a nanoporous carbon produced by the pyrolysis of polyvinylidene chloride (PVDC). Sample AX-21 MSC-30 is produced by the Kansai Coke and Chemicals Co. Ltd., Japan. Samples 3K and HS;0B were produced at the University of Missouri.

### 2.4.1 Experimental Methods

The specific surface area  $\Sigma$  is determined from sub-critical nitrogen isotherms measured by an Auorosorb-1C (Quantachrome Instruments), using Brunauer-Emmett-Teller (BET) theory in the pressure range of 0.01 to 0.03  $P/P_0$  suitable for microporous materials. The pore volume  $V_p$  is determined at a pressure of 0.995  $P/P_0$ . Table 2.1 gives the surface area and pore volume for each sample. MSC-30 and 3K have surface areas and pore volumes typical of high end activated carbons. Sample HS;0B has much smaller values, consistent with the lack of activation. Quenched solid density functional theory (QSDFT) is used to calculate pore size distributions (PSDs). Competing methods, such as non-local density functional theory (NLDFT), assume flat graphitic pore structure without taking into account the effects of surface roughness. QSDFT, provided by Quantachrome's data reduction software, is a modified version of (NLDFT) that takes into consideration surface roughness and heterogeneity, making this method suited for disordered carbon materials [13, 14].

Figure 2.4 shows the pore size distribution for each sample calculated using QSDFT. MSC-30 and 3K have a broad distribution of pore sizes, whereas HS;0B contains

mainly a narrow distribution of pores in the 6-10 Å range. Simulations of hydrogen adsorbed in slit-shaped pores composed of graphene [42] have shown that above 10 Å, the binding energy is essentially the same as a single sheet of graphene. Since MSC-30 and 3K have a significant number of pores with widths above 10 Å, we should expect the isosteric heat to fall to the constant value of graphene at high coverage, as discussed in Section 2.3. At low coverage, the higher binding energy of the small pores will cause the isosteric heat to be higher. Conversely, HS;0B, which has the majority of its pores with widths under 10 Å, would be expected to have a higher isosteric heat even at high coverage.

Table 2.1: Sample Characteristics: Specific surface area  $\Sigma$  and micropore volume  $V_p$ , determined by nitrogen adsorption. Nominal width of the adsorption layer  $l$  and film volume  $V_a$  determined by analysis of the high coverage isosteric heat. \*This value represents the maximum value for which 100% of the pore volume is in the adsorbed film.

sample	MSC-30	3K	HS;0B
$\Sigma$ (m <sup>2</sup> /g)	2600	2700	700
$V_p$ (cm <sup>3</sup> /g)	1.86	1.68	0.34
$l$ Å	5.4	5.1	4.9*
$V_a$ (cm <sup>3</sup> /g)	1.40	1.38	0.34

Hydrogen (99.999% purity) adsorption isotherms were measured volumetrically using an HTP-1 Volumetric sorption analyzer (Hidden Isochema Ltd). Hydrogen measurements were performed at temperatures of 80 and 90 K and at pressures ranging from 1 to 100 bar. Dry sample mass was determined by measuring the sample mass under vacuum after heating to 400 C for two hours under vacuum ( $\sim$ 20 torr). Excess isotherms are shown in Figure 2.5. Samples MSC-30 and 3K show qualitatively similar isotherms, consistent with their qualitatively similar pore characteristics. Remarkably, the isotherms for HS;0B are quite unusual. The excess isotherm do not have a peak, a feature which is normally seen at cryogenic temperatures as the gas density

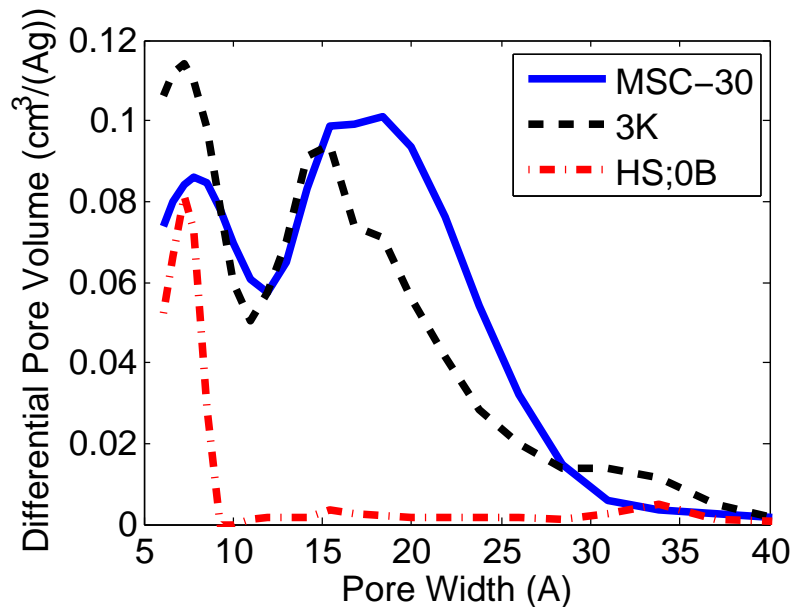


Figure 2.4: Pore size distributions calculated using QSDFT methods.

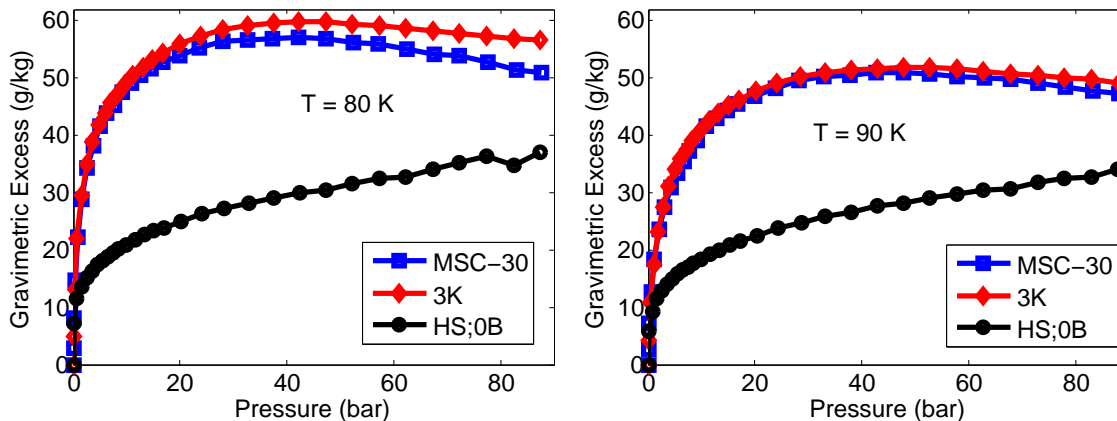


Figure 2.5: Excess adsorption hydrogen isotherms taken at temperatures of 80  $K$  (left) and 90  $K$  (right).

begins to grow faster than the density of the adsorption layer. In addition, the cryogenic adsorption is nearly double what would be expected from “Chahine’s rule” [58], which predicts a maximum of about 10 g/kg per 500 m<sup>2</sup>/g. All isotherms were run multiple times to confirm these results.

## 2.4.2 Results

Calculation of the isosteric heat requires the determination of differences between adsorption isotherms taken at nearby temperatures, in this case at 80 and 90 K. The small numerically determined differentials used in Eqs. 2.6 and 2.11 make the process quite sensitive to the fits that are required to both interpolate between the data points of the isotherms and smooth experimental error. Even fits which look barely different to the eye can have drastically different results. We have chosen to use a Langmuir-Freundlich fit, Eq. 2.1 due to its ability to model the typical behavior of hydrogen isotherms without using too many parameters. However we found that using the entire pressure range of the data resulted in isosteric heats at low coverage that were up to 5 kJ/mol higher than if the fit was done only over the low pressure range. This effect was found to be particularly pronounced for isotherms which begin to level off at low pressure. Since real samples have significant heterogeneity, it would be highly improbable that a single fit would work for a broad pressure or coverage range, hence this sharp increase seen is an obvious methodological artifact. Therefore we adopted a fitting procedure in which a moving window [59] of  $N$  data points around the pressure of interest were used for the fit. Figure 2.6 shows the effects of window size on the resultant isosteric heat of hydrogen adsorbed on MSC-30. When the window size is too small, experimental error is amplified. Conversely, for large window sizes, the isosteric heat becomes significantly different, particularly at low coverage. We find that a window of size  $N = 13$  yields the most robust results for a variety of sample and adopt this for the remainder of this work.

While there are many types of fit to choose from [54, 60, 61] that would also work well using a moving window, we found the use of a virial-type fit [61] to be particularly prone to error. 2.7 shows isosteric heats calculated for sample 3K using either Langmuir-Freundlich fits or virial fits. The latter method assumes that the function  $m_s$  vs.  $\ln(p/m_s)$  can be described in the most general way by a polynomial

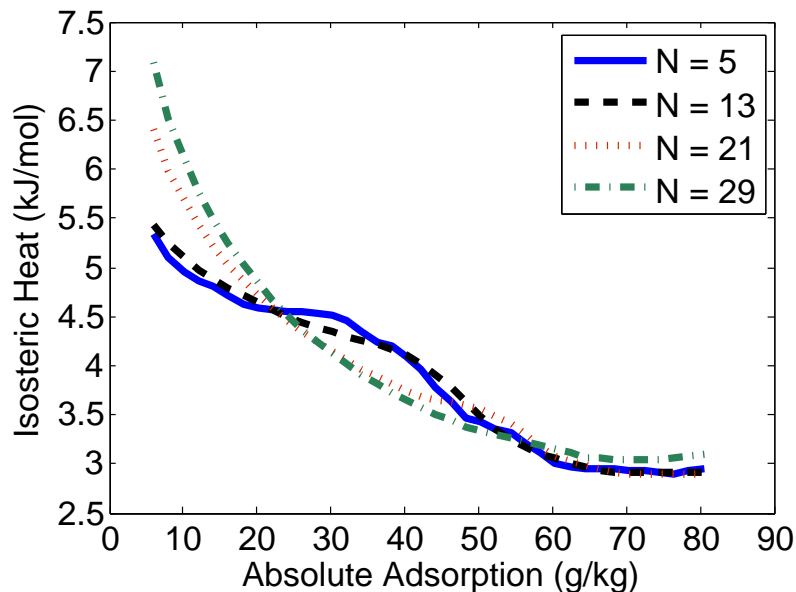


Figure 2.6: Results of varying  $N$ , the size of the fitting window, on the isosteric heat calculated using the Clausius-Clapeyron equation (Eq. 2.6) for sample MSC-30. The absolute adsorption has been calculated using Eq. 2.3 from the excess adsorption, with  $l = 5 \text{ \AA}$ . A small window results in large variations in the isosteric heat as a function of coverage. When the window is large, the isosteric heat at low coverage increases dramatically.

function. Czepirski et al. [61] show that 3–5 fitting parameters are typically needed. As is often the case with polynomial fits, the larger number of fitting parameters used can introduce curvature to the function, particularly between the experimental data points. When differential values are taken, this effect becomes quite pronounced, significantly affecting the resultant isosteric heat. Conversely, the assumptions built into the Langmuir-Freundlich fit ensure more reasonable interpolation between data points, and sample heterogeneity can be dealt with by the moving window technique. Using a moving window with a virial fit merely exacerbates the problem of artificial curvature between the data points. Additionally, at high coverage this type of fit can diverge, making the determination of the width of the adsorption layer quite difficult. In addition, changing  $l$  significantly affects the isosteric heat at low coverage. This is in contrast to the Langmuir-Freundlich fits, where changing  $l$  significantly affects

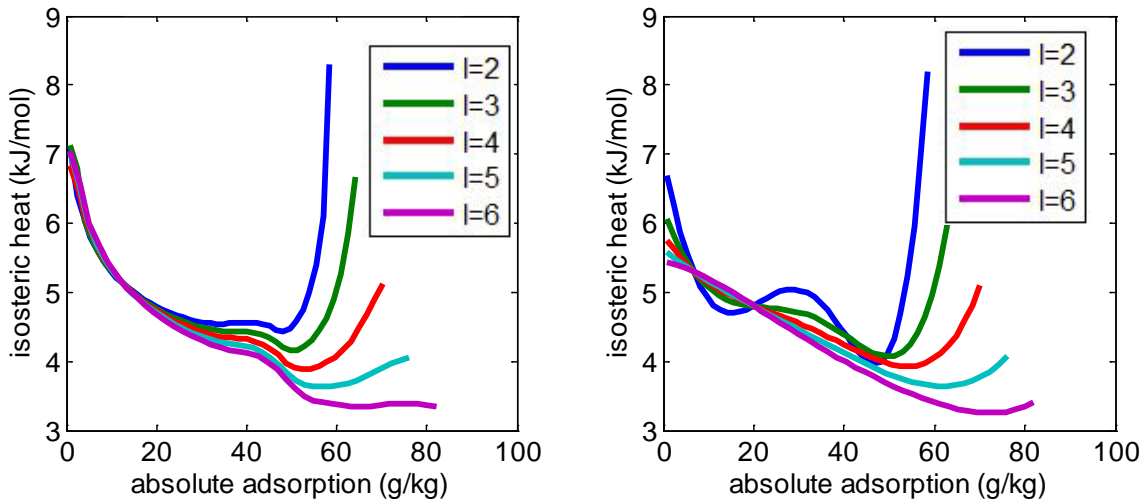


Figure 2.7: Isosteric heat calculated for sample 3K using either Langmuir-Freundlich fits (left) or virial fits (right). In addition, the calculation has also been done for different values of  $l$ , the nominal width of the adsorption layer.

only the high coverage isosteric heat.

For all of the fits we tried, extension of a fit below the lowest non-zero data point in order to extrapolate the isosteric heat at zero coverage can result in widely varying results from sample to sample, even when there is very little difference in any of the other characteristics of the samples which would suggest a real effect. Therefore we do not suggest the use of this practice.

Figure 2.8 shows the effects of varying the value of  $l$  used to calculate the absolute adsorption on the isosteric heat calculated for hydrogen adsorbed on MSC-30. In addition, to see the effects of the assumptions used to derive the Clausius-Clapeyron equation (Eq. 2.6), the isosteric heat is also calculated using the assumptionless Clausius-Clapeyron relation (Eq. 2.11). The ideal gas assumption was found to not have a significant effect; however it is evident that the use of the actual specific volume of the adsorbed film does have a significant effect on the results, particularly at high coverage. However, given the results shown in Figure 2.3 and discussion in Section 2.2, we will use the Clausius-Clapeyron equation to determine  $l$ .

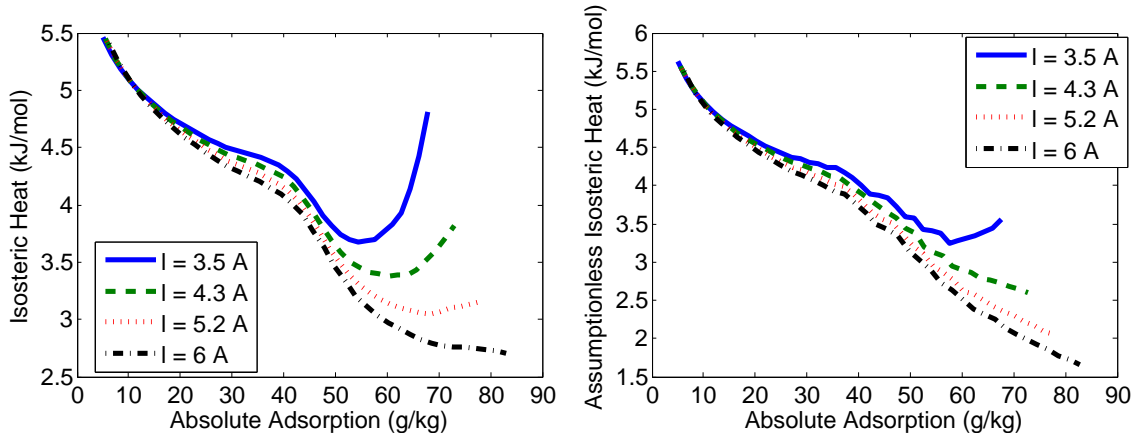


Figure 2.8: Isosteric heat calculated for MSC-30 using the Clausius-Clapeyron equation (Eq. 2.6, left) or the assumptionless Clausius-Clapeyron relation (Eq. 2.11, right), for different values for  $l$ , the nominal width of the adsorption layer.

For each sample,  $l$  was varied over a finer scale until the isosteric heat calculated with the Clausius-Clapeyron equation (Eq. 2.6) fell off to a constant value at high coverage. The resultant values of the volume of the adsorbed film  $V_a$  and the nominal width of the adsorption layer  $l$  are given in Table 2.1, and Figure 2.9 shows the isosteric heat for each sample as a function of coverage. For the activated carbon samples MSC-30 and 3K,  $l \approx 5 \text{ \AA}$ . This value is quite sensible, as it is about equal to the size of a hydrogen molecule, plus the width of the adsorption potential at several  $kT$  above the minima [42]. The isosteric heats range from about 6 kJ/mol at low coverage to 3 kJ/mol at high coverage, similar to what has been theoretically predicted for flat carbon pores [62] and experimentally found for graphene and MSC-30 [44, 45].

We have used data for other activated carbons, shown in Figure 2.10, to help refine our methodology. For some of these samples, isotherms did not cover such a large pressure range. Because we have many samples which have been manufactured in similar ways and have similar adsorption, we expect their isosteric heats to be similar as well. It can be seen that the results for all the samples are quite comparable, deviating from one another by less than 1 kJ/mol over the entire coverage range.

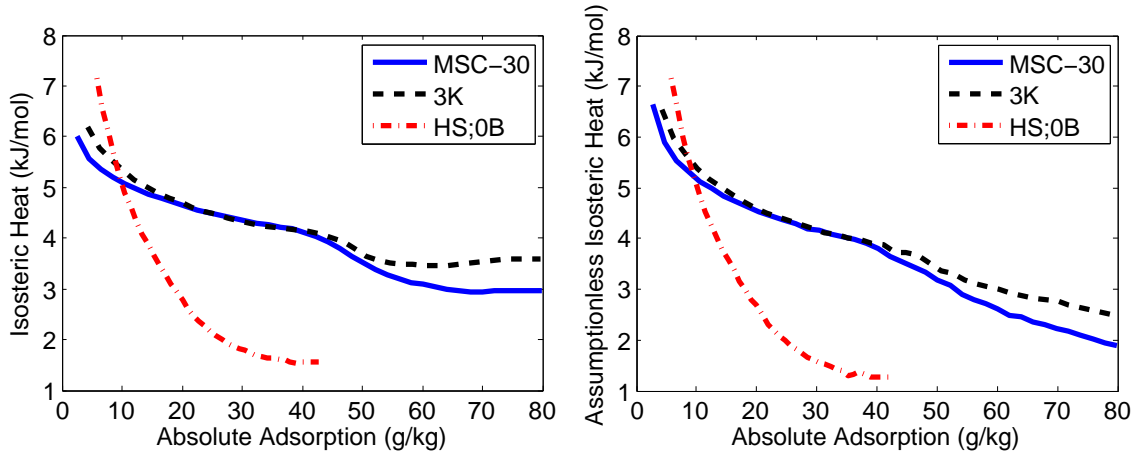


Figure 2.9: Isosteric heat calculated for each sample using the Clausius-Clapeyron equation (Eq. 2.6, left) or assumptionless Clausius-Clapeyron relation (Eq. 2.11, right), using the values of  $l$  reported in Table 2.1.

Because these samples are all quite similar, both in manufacturing methods and adsorption properties, this result reflects the robustness of our methodology.

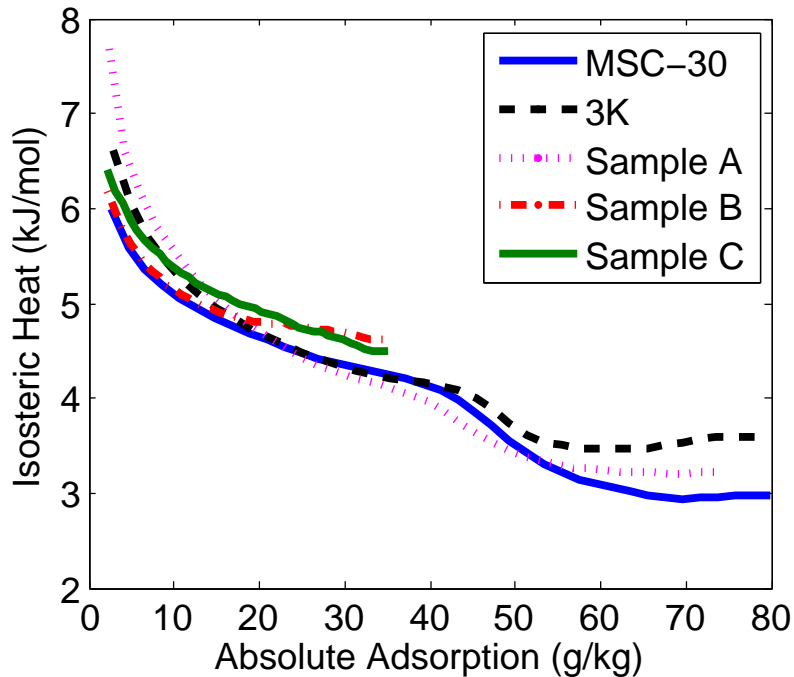


Figure 2.10: Isosteric heat calculated for a number of activated carbon samples with the Clausius-Clapeyron equation using the value of  $l$  for which the isosteric heat at high coverage falls to a constant.

Because most isosteric heat results reported in the literature use the Clausius-Calpyeron equation, without addressing the assumptions used to derive this equation, the results calculated with this method should be used for comparison purposes. In addition, these results are also more likely to be equal to the binding energy plus an offset which is independent of coverage, as the actual volume of the film is taken as constant. However, the values calculated with the assumptionless Clausius-Clapeyron relation, which take into account the actual work done to compress the molecules, should be used to compare with calorimetry measurements.

The results were quite different for HS;0B. For this sample, there was no value of  $l$  and no fitting procedure that produced a constant isosteric heat at high coverages. For the results shown in Figure 2.9, the value of  $l = 4.9 \text{ \AA}$  used was the maximum value for which 100% of the pore volume is in the adsorbed film. Because this value is slightly smaller than the other samples, it seems to indicate the pores in this sample are just below the width where exactly two layers of hydrogen can fit. While the larger value for the isosteric heat of 7.2 kJ/mol at low coverage is consistent [42] with the many small pores seen in the pore size distribution (Figure 2.4); the value of 1.6 kJ/mol at high coverage is significantly lower than would be expected for any type of pores composed of carbon [62, 63] and, since most of the sites seem to have isosteric heats less than those of activated carbons, does not explain the excellent cryogenic excess adsorption.

This is not the first time an unusually low isosteric heat has been reported, likewise coupled with a lack of a peak in the excess up to 100 bar and unusually high adsorption at cryogenic temperatures [38, 39, 64]. Table 2 summarizes the characteristics of these samples and compares them to MSC-30. Where given, a smaller value for the isosteric heat at high coverage roughly corresponds to a higher excess adsorption at cryogenic temperatures. It is surprising that this unusual trio is observed in such different types of samples, which also have widely varying surface areas. We speculate that there

may be some new adsorption phenomena at work.

Table 2.2: Maximum excess adsorption per surface area at cryogenic temperatures, and isosteric heat of adsorption for MSC-30, 3K, HS;0B, and samples in the literature with similar characteristics to HS;0B. Values of  $\Delta h$  are given at low coverage and high coverage, where available.

sample	type	$m_e/\Sigma$ ( $\mu\text{g}/\text{m}^2$ )	$\Delta h$ (kJ/mol)
MSC-30	activated carbon	19.6	6.0–3.0
3K	activated carbon	21.0	6.2–3.6
[39]	MOF-5	28.1	2.6–2.1
[64]	zeolite NaX	29.3	4.1– ?
[38]	MOF-177	33.6	4–0.5
[64]	activated carbon	47.8	2.1– ?
HS;0B	PVDC	52.8	7.2–1.6

## 2.5 Summary

In conclusion, we have shown that correctly calculating the isosteric heat of adsorption at any coverage requires careful attention to detail. The absolute adsorption, rather than the excess adsorption or total storage must be used and the correct equation to calculate the absolute adsorption from the excess is needed. At high coverages, the actual volume of the adsorbed film is an important correction; therefore for best results the assumptionless Clausius-Clapeyron relation should be used. In addition, we have found that the fitting procedure used is quite important. In particular an incorrect fit can significantly overestimate the isosteric heat at low coverage. We also found that the extension of the fit beyond the lowest non-zero data point is not a suggested practice. Given that many papers report only one value of isosteric heat at low coverage, it is important that robust methods be adopted and authors report details of the methods used, especially when unusually high isosteric heats are

claimed.

We have used the assumption that for hydrogen adsorbed on carbon materials, the isosteric heat of adsorption should fall to a constant value at high coverage to estimate the film volume. This method gives the nominal width of the film as  $l \approx 5 \text{ \AA}$ , which is about equal to the size of a hydrogen molecule plus the width of the adsorption potential. Using an incorrect value for  $l$  significantly affects the results at high coverage.

Using these robust methods, we found that isosteric heats for hydrogen adsorbed on several samples. We will compare isosteric heats measured directly via calorimetry to these results in Chapter 5. The isosteric heats for the activated carbon samples were quite similar to one another, even as a function of coverage, ranging from  $\approx 6\text{--}3 \text{ kJ/mol}$ . However, we also found a sample that had an unusually low isosteric heat. In addition, this sample did not have a peak in its excess at 80 K, and its maximum excess adsorption was significantly higher than what would be expected for its surface area. Four other samples with this unusual trio of features were found in the literature, suggesting that there may be some new adsorption phenomena at work in some samples.

# Chapter 3

## Calculation of Theoretical Inelastic Neutron Scattering Spectra from Hydrogen Adsorbed in Slit-Shaped Pores

### 3.1 Introduction

Hydrogen storage by adsorption in porous carbon materials such as activated carbon (AC), amorphous carbon nanotubes, single-wall carbon nanotubes (SWCNT) and porous carbon has been previously studied [65]. Traditionally AC has been modeled as being composed of slit-shaped pores, composed of two flat parallel graphene sheets, both for adsorption simulations [42,66] and for obtaining pore size distributions from nitrogen adsorption data [12]. Simulations [42,67–69] show that slit-shaped pores with widths between 6–10 Å have the widest range of properties for hydrogen adsorption, as the depth and width of the potential well varies significantly. As the width increases beyond 10 Å, the pore begins to behave simply as two independent sheets. Commonly used methods of pore characterization, such as nitrogen adsorption [12], are unable

to probe the smallest pores because of the larger size of  $N_2$  as compared to  $H_2$ . Conversely, small angle X-ray scattering [70] characterizes all of the pore volume, including pores which  $H_2$  is unable to access. To characterize samples as accurately as possible, it is desirable to use  $H_2$  itself as the probe. In addition, both of these commonly used techniques rely on a large number of approximations to interpret the results, thus a more robust understanding of a sample is gained by comparing results from several different techniques.

Incoherent inelastic neutron scattering (IINS) has been used as just such a complementary characterization technique on samples of  $H_2$  adsorbed on SWCNT [71–74], AC [75], other carbon materials [76, 77], and various other adsorbents [78–86]. Because of the high incoherent cross section of  $H_2$ , IINS is able to detect the hydrogen molecules as they occupy the variety of adsorption sites present in each sample, offering information about energy levels and quantum states occupied. This information is a helpful complement to techniques which probe the carbon itself. All previous work using this method has been focused on an analysis of the rotational transitions, which give information about the anisotropy of the  $H_2$  adsorption potential. The rotational energy levels are given by

$$E_J = J(J + 1) \frac{\hbar^2}{2\mu a^2}, \quad (3.1)$$

where  $J$  is the molecular angular momentum quantum number of the molecule,  $\mu = 1.008u$  is the reduced mass of the molecule, and  $a = 0.741 \text{ \AA}$  is the distance between the two atomic nuclei. Experiments are typically done at temperatures near 14 K, the triple point of bulk para-hydrogen, so that the majority of the hydrogen is adsorbed and the high-density 2D liquid phase constrains movement of a hydrogen molecule along the adsorption plane. The low temperature and the use of para-hydrogen ( $J = 0, 2, 4, \dots$ ) instead of ortho-hydrogen ( $J = 1, 3, 5, \dots$ ) ensures that all

molecules are initially in the ground  $J = 0$  rotational state. Transitions to even  $J$  states are proportional to the coherent cross section of hydrogen, which is quite small. Transitions to odd  $J$  states are proportional to the incoherent cross section of hydrogen and are easily visible. In the  $J = 0$  state, denoted as the  $\alpha = s$  state, the molecule axis is equally likely to be in any direction. In the  $J = 1, J_z = 0$  state, denoted as the  $\alpha = p_z$  state, the molecule axis tends to be aligned perpendicular to the graphene plane. In the  $J = 1, J_z = \pm 1$  states, denoted as the  $\alpha = p_x, p_y$  states, the molecule axis tends to be aligned parallel to the graphene plane. In the gas phase, the first rotational transition occurs at  $\Delta E_{s \rightarrow p} = 14.7$  meV and is triply degenerate. For adsorbed  $\text{H}_2$ , the rotational anisotropy of the adsorption potential partially removes this degeneracy and the transitions now occur at a 2/1 intensity ratio at energies which are highly dependent on the slit characteristics. Roto-vibrational transitions, where the rotational state as well as the vibrational state changes, are also possible.

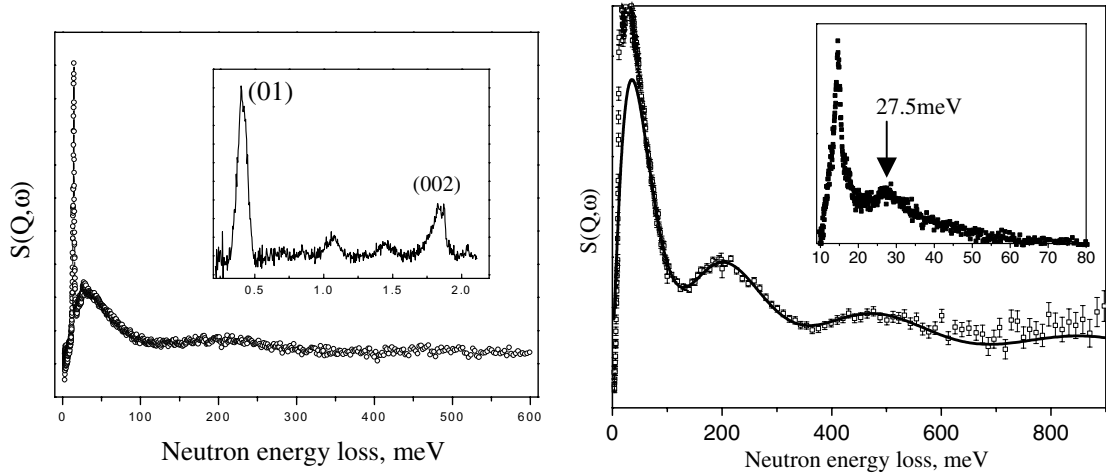


Figure 3.1: IINS spectra measured at 13 K from a nearly complete monolayer of adsorbed p- $\text{H}_2$  on SWCNT (left, after Ref. [72]) and AC (right, after Ref. [75]). The solid lines are a fit of the Young and Koppel [87] model to experimental data (85–600 meV). The inset on the right shows the spectrum after subtraction of the solid line. The fits and subtraction were done by Georgiev *et al.* [72, 75]. Both spectra show a peak around 14.7 meV, which can be attributed to the first rotational transition. The SWCNT spectra also has a peak at around 30 meV, which is likely the first roto-vibrational transition. The AC spectra has roto-vibrational transitions at a variety of energies (10–60 meV).

Up until now, most of these IINS experiments on adsorbed hydrogen have been done with an adsorbent which is more ordered, such as SWCNT. A comparison of a typical spectra at near monolayer coverage, Figure 3.1, for SWCNT [72] and AC [75] reveals a possible reason for the dearth of experimental results for AC. The spectrum from SWCNT, after the subtraction of the free recoil contribution, shows a sharp peak at about 14.5 meV, the first rotational transition for which the spectrum can be easily analyzed, as well as a much smaller, but still well-defined peak at around 30 meV, which is likely the first roto-vibrational transition (but could also be due to multiple scattering). In contrast, the spectrum from AC shows a sharp peak at 14.6 meV as well as a broad complex peak extending from 10 to 60 meV. This complex peak, which is likely due to the heterogeneity of activated carbon, makes the analysis of the spectrum more difficult. However it might also offer a powerful characterization technique.

Previous work has calculated transition energies and/or spectra using a cylindrical pore model [17–19]. This work calculates transition energies and spectra using the slit-shaped pore model. Using this model, in Section 3.2 we calculate the energy levels and wavefunctions of an  $H_2$  molecule adsorbed in pores of variable width. The energy levels are used to calculate the transition energies between different states. The perturbation of intermolecular interactions is also considered, both its effect on the transition energies and its tendency to force bi-layer adsorption in larger slits. In Section 3.3, the wavefunctions are used to calculate the double differential scattering cross section. In contrast to previous work, the scattering cross section is not treated as isotropic, but form factors and Debye-Waller factors are calculated for momentum transfer perpendicular and parallel to the adsorption plane. In Section 3.4, these results are combined to calculate IINS spectra for hydrogen adsorbed on graphite and activated carbon composed of a uniform distribution of slit-shaped pores, where the direction of the momentum transfer has been isotropically averaged. The calculated

spectra are compared with previously collected experimental data. A shift in the center of gravity of the first rotational transition is observed in the calculated spectra, similar to the shift observed experimentally. Several different factors contribute to this shift. The usefulness of the slit-shaped pore model is discussed.

## 3.2 Energy Levels and Wavefunctions of Adsorbed $\text{H}_2$

We wish to calculate the energy levels and wavefunctions  $\psi_{\alpha,n}(x, y)$  of an adsorbed  $\text{H}_2$  molecule in a quantum state  $(\alpha, n)$ , where  $n$  is the quantum number for motion perpendicular to the adsorption plane. To do this, it is necessary to calculate the potential between an  $\text{H}_2$  molecule and a graphene sheet for each position  $\vec{r}$  of the molecular center of mass and orientation  $\theta, \phi$  of the molecular axis relative to the graphene plane. We fully quantize the rotational molecular motion, and the vibrational motion perpendicular to the adsorption plane (in the  $z$ -direction). The rotational and vibrational degrees of freedom are approximated as independent with  $\Psi_{\alpha,n}(\vec{r}, \theta, \phi) = \Phi_{\alpha}(\theta, \phi)\psi_{n,\alpha}(\vec{r})$ . Lu et al. [17] similarly separate rotational and translational coordinates. The molecule is assumed to be in its molecular vibrational ground state. Lennard-Jones (LJ) potentials are commonly used for inter-atomic potentials.

$$V_{LJ}(r) = 4\epsilon \left[ \left(\frac{\sigma}{r}\right)^{12} - \left(\frac{\sigma}{r}\right)^6 \right], \quad (3.2)$$

where  $\epsilon$  is the depth of the potential and  $\sigma$  is the distance between atoms at which the potential is equal to zero.

Xu et al. [88] have proposed a form for the potential between a classical hydrogen molecule and carbon atom that takes into account the fact that most of the electronic

density is centered between the two protons.

$$V_{H_2-C}(\vec{r}, \hat{n}) = V_{LJ}(|\vec{r} + \frac{\vec{a}}{2}|) + V_{LJ}(|\vec{r} - \frac{\vec{a}}{2}|) + vV_{LJ}(|\vec{r}|), \quad (3.3)$$

where  $(\vec{r}, \hat{n})$  give the position and orientation of the hydrogen molecule relative to the carbon atom and  $\vec{a}$  is the vector between the two hydrogen atom centers. Xu et al. determined  $\epsilon = 0.371$  meV,  $\sigma = 2.95$  Å, and  $v = 7.5$  ( $v$  is a dimensionless parameter that gives the proportion of the H<sub>2</sub>-C interaction that is centered between the two hydrogen atoms) by matching experimental and theoretical values for the roto-vibrational transitions of an H<sub>2</sub> molecule inside of a C<sub>60</sub> fullerene [88].

Using the Xu H<sub>2</sub>-C potential, the matrix element of the potential between a graphene sheet and an H<sub>2</sub> molecule using the rotational states as a basis set can be calculated as

$$V_{\alpha, \alpha'}^{H_2-g}(\vec{r}) = \langle \Phi_{\alpha}(\theta, \phi) | \sum_{i=1}^N V_{H_2-C}(\vec{r}_i, \hat{n}_i) | \Phi_{\alpha'}(\theta, \phi) \rangle, \quad (3.4)$$

where  $N$  is the number of carbon atoms in the graphene sheet and  $(\vec{r}_i, \theta_i, \phi_i)$  give the center-of-mass position and orientation of the hydrogen molecule relative to the  $i^{\text{th}}$  carbon atom. The rotational wavefunctions are given by the spherical harmonics, where the  $p_x, p_y$  states have been formed from linear combinations of the  $J = 1, J_z = \pm 1$  states.

$$\begin{aligned} \Phi_s(\theta, \phi) &= \frac{1}{\sqrt{4\pi}}; \\ \Phi_{p_z}(\theta, \phi) &= \frac{3}{\sqrt{4\pi}} \cos \theta; \\ \Phi_{p_x}(\theta, \phi) &= \frac{3}{\sqrt{4\pi}} \sin \theta \cos \phi; \\ \Phi_{p_y}(\theta, \phi) &= \frac{3}{\sqrt{4\pi}} \sin \theta \sin \phi. \end{aligned} \quad (3.5)$$

The off-diagonal matrix elements vanish due to symmetry except between the  $p_x$  and  $p_y$  states, where the amount of coupling varies depending on the position above the graphene plane. This means that the molecular axis of a  $\text{H}_2$  molecule in a  $p$  rotational state does indeed tend to align in a direction perpendicular or parallel to the graphene plane. In the center of a hexagonal cell of graphite, the breaking of the rotational symmetry due to the external potential results in different energies for  $p$  states aligned parallel ( $p_x, p_y$ ) or perpendicular ( $p_z$ ) to the adsorption plane. The potential was also calculated at several different (x,y) locations relative to the graphene plane. At these sites, the  $p_x$  and  $p_y$  states do not have the same potentials. However, the differences were small enough that all further calculations use the potential above the center of a hexagonal cell.

We now consider a hydrogen molecule in a particular rotational state adsorbed inside of a slit-shaped pore composed of two graphene sheets separated by a width  $w$ . The potential can be calculated by simply adding the potential from each of the two graphene sheets. Figure 3.2 shows the potentials for each rotational state for  $w = 6 \text{ \AA}$  and  $w = 8 \text{ \AA}$ , where 14.7 meV has been added to the potentials for molecules in  $p$  states to account for their rotational energy [Eq. (3.1)]. Notice that the potentials for the  $p$  states split, with the  $p_x, p_y$  states having a deeper potential than the  $p_z$  state. Because the molecular axis of a molecule in the  $p_x, p_y$  states tends to be parallel to the graphene plane, it can approach the graphene plane closer resulting in an enhanced interaction. We can also see from these potentials that coupling between the rotational and vibrational degrees of freedom should not be significant. If, for instance, the  $p_z$  potential was above the  $p_x$  potential at some distances and below the  $p_x$  potential at other distances, coupling would be an important consideration. Referring to our Figure 3.2, one can see that for these potentials this is not the case, and thus coupling is not a significant issue, supporting our separation of these degrees of freedom.

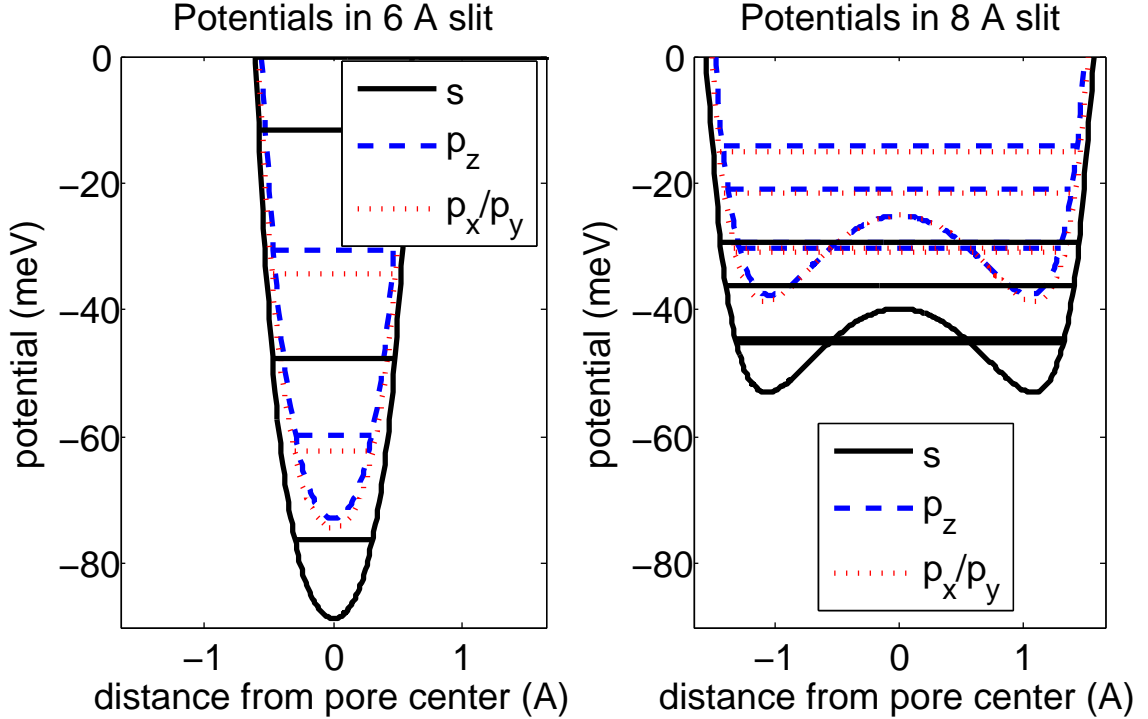


Figure 3.2: Calculated potentials and energy levels for the  $s$ ,  $p_z$ , and  $p_x, p_y$  rotational states in a 6 Å (left) and 8 Å (right) slit.

The vibrational part of the wavefunction,  $\psi_{n,\alpha}(\vec{r})$ , was then calculated for each slit width by numerically solving the one dimensional time-independent Schrödinger equation for the corresponding potential. Figure 3.2 also shows the first few energy levels for each rotational state. In the  $w = 6$  Å slit, these are widely spaced. In the  $w = 8$  Å slit, the first two states are nearly degenerate.

Based on these calculations, for a flat graphene sheet one would expect rotational transitions at energies  $\Delta E_{s,1 \rightarrow p_x, p_y, 1} = 14.34$  meV and  $\Delta E_{s,1 \rightarrow p_z, 1} = 15.37$  meV with an intensity ratio of 2:1. However, we have not yet taken into account the effects of the adjacent hydrogen molecules. For the liquid densities at which IINS experiments are performed, the intermolecular interactions are a non-negligible perturbation. Wang et al. [89] give values of  $\epsilon = 2.94$  meV and  $\sigma = 2.96$  Å for the LJ H<sub>2</sub>-H<sub>2</sub> interaction. In order to calculate the potential between two H<sub>2</sub> molecules in different rotational states, it is again necessary to have an H<sub>2</sub>-H<sub>2</sub> potential that depends on the orientation

of the H<sub>2</sub> molecules. The H-H interaction was calculated by fitting the Wang potential to a potential between two hydrogen molecules composed of two hydrogen atoms in the  $s$  state, given by

$$V_{j,j'}^{H_2-H_2}(\vec{r}) = \sum_{i,k=1}^2 \langle \Phi_\alpha(\theta_i, \phi_i) \Phi_{\alpha'}(\theta_k, \phi_k) | \times \quad (3.6)$$

$$V_{H-H}(\vec{r}_i - \vec{r}_k, \theta_i, \theta_k, \phi_i, \phi_k) | \Phi_\alpha(\theta_i, \phi_i) \Phi_{\alpha'}(\theta_k, \phi_k) \rangle,$$

where  $(\vec{r}_i, \theta_i, \phi_i)$  give the position and orientation of the  $i^{\text{th}}$  atom in the first molecule and  $(\vec{r}_k, \theta_k, \phi_k)$  give the position and orientation of the  $k^{\text{th}}$  atom in the second molecule. The H-H potential is also approximated by a LJ potential. The best-fit parameters were calculated to be  $\epsilon = 1.0$  meV and  $\sigma = 2.73\text{\AA}$ , using  $v = 0$ . A more accurate determination of these parameters would require experimental data which probes the H<sub>2</sub>-H<sub>2</sub> interaction.

If we assume that all of the neighbors of a particular hydrogen molecule are in the  $s$  state, we can also calculate the average potential between a molecule in the state  $\alpha$  and its six neighbors, assuming hexagonal close packing with  $d_{H_2H_2}$  being the average in-plane distance between neighbors. Similar to the H<sub>2</sub>-graphene potential, the potentials for the  $p$  states split, except that now the  $p_x, p_y$  states have the shallower potential and the  $p_z$  state has the deeper potential than the  $s$  state. The  $p_z$  state has the molecular axis tending to be perpendicular to the adsorption plane, which means it is parallel to the other hydrogen molecules. This means it can approach adjacent molecules more closely and feels a deeper potential. Using  $d_{H_2H_2} = 3.38\text{\AA}$ , the average distance between adjacent hydrogen molecules found with high-density molecular dynamics simulations, we can now correct the rotational transition energies for the perturbation of adjacent H<sub>2</sub> molecules and find them at energies  $\Delta E_{s \rightarrow p_x, p_y = \pm 1} = 14.51$  meV and  $\Delta E_{s \rightarrow p_z} = 14.92$  meV at a 2:1 intensity ratio. While the numerical results of this calculation are highly dependent on the H-H potential used and the positioning

of adjacent H<sub>2</sub>, it is interesting to note that this perturbation has the ability to shift the mean of the first rotational transition for adsorbed H<sub>2</sub> from the 14.7 meV at which it is observed for gaseous hydrogen. This issue will be discussed further in the results section.

The same correction can be applied for all slit widths, and now the transition energies for  $s, 1 \rightarrow \alpha', n'$  can be plotted for each slit width, as shown in Figure 3.3. At a width of about 8.4 Å, the  $n' = 1$  and  $n' = 2$  energy levels differ by less than 0.8%, so close that we consider them degenerate. For slits above this size, the intermolecular interactions will result in “left-adsorbed” [ $\psi_l = (\psi_1 + \psi_2)/\sqrt{2}$ ] or “right-adsorbed” [ $\psi_l = (\psi_1 - \psi_2)/\sqrt{2}$ ] wavefunctions being lower in energy; essentially molecules are adsorbed in two layers. Because the intermolecular interactions are added only as a perturbation, this cutoff cannot be calculated exactly. However, these results match the findings of classical Monte Carlo simulations which show two complete layers form at  $w = 8.5$  Å [42]. Below this size, the transition energies are very dependent on slit width.

### 3.3 Scattering Cross Section

For momentum transfers up to  $q = 4\text{--}5$  Å<sup>-1</sup>, the double differential scattering cross-section is given by [71]

$$\frac{d^2\sigma}{d\Omega dE} = \frac{k_f}{k_i} F_{j,n \rightarrow j',n'}(\vec{q}) e^{-2W} \delta(E - \Delta E), \quad (3.7)$$

where  $k_i$  and  $k_f$  give the initial and final neutron wave vector,  $F_{\alpha,n \rightarrow \alpha',n'}(\vec{q})$  is the molecular form factor, and  $2W$  is the Debye-Waller factor. Given our separation of the rotational and vibrational parts of the wavefunction, the form factor, which is the overlap integral between the momentum transfer and the initial and final wavefunc-

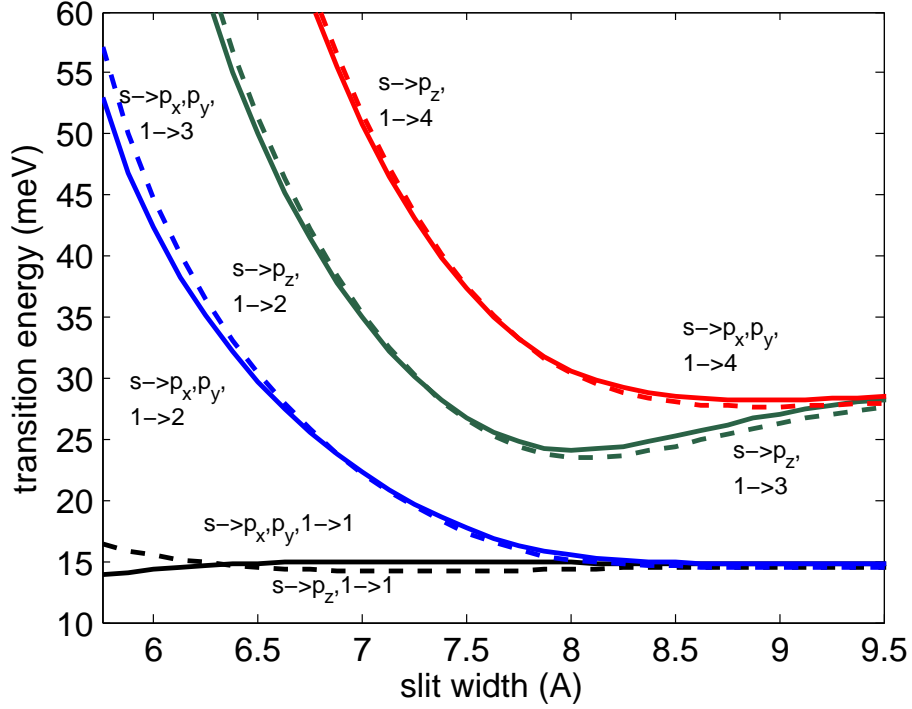


Figure 3.3: Neutron energy losses for  $s, 1 \rightarrow \alpha', n'$  transitions of adsorbed  $\text{H}_2$  as a function of slit-width. The solid lines are the  $s \rightarrow p_x, p_y$  transitions, while the dashed lines are the  $s \rightarrow p_z$  transitions. The bottom pair of curves represent the pure rotational transitions, while the other lines are roto-vibrational transitions. The energies are quite variable up to slit widths of 9 Å. Above this range, the energy levels become degenerate and the slits behave more as two independent graphene sheets.

tions, can be further broken up into rotational and vibrational parts:

$$F_{\alpha, n \rightarrow \alpha', n'}(\vec{q}) = b_{inc}^2 |\langle \psi_i | e^{i\vec{q}\vec{r}} | \psi_f \rangle|^2 = F_{\alpha \rightarrow \alpha'}(\vec{q}) F_{n \rightarrow n'}(\vec{q}). \quad (3.8)$$

If  $J_q$  is defined as the component of the angular momentum aligned with the momentum transfer, Young and Koppel [87] give the rotational part of the form factor for  $s \rightarrow p$  transitions of hydrogen in the gas phase as

$$F_{s \rightarrow J'=1, J'_q}(q) = b_{inc}^2 |\langle \psi_s(\theta, \phi) | \sin \frac{\vec{q} \cdot \vec{a}}{2} | \psi_{J'=1, J'_q}(\theta, \phi) \rangle|^2, \quad (3.9)$$

where  $\vec{a}$  is the vector between the two atomic nuclei. Yildirim and Harris [18] give

a similar expression for the  $s \rightarrow p$  scattering cross section following the formalism of Elliott and Hartmann [90]. If the wavefunctions are given by the spherical harmonics, the form factors for  $J_q = 0$  and  $J_q = \pm 1$  can be calculated as

$$\begin{aligned}
 F_{s \rightarrow J'=1, J'_q=0}(q) &= b_{inc}^2 \left| \frac{\sqrt{3}}{4\pi} \int \sin\left(\frac{qa \cos \theta}{2}\right) \cos \theta \, d\Omega \right|^2 \\
 &= 12b_{inc}^2 j_1^2\left(\frac{qa}{2}\right),
 \end{aligned} \tag{3.10}$$

$$\begin{aligned}
 F_{s \rightarrow J'=1, J'_q=\pm 1}(q) &= b_{inc}^2 \left| \frac{\sqrt{3}}{4\pi} \int \sin\left(\frac{qa \cos \theta}{2}\right) \sin \theta \, e^{\pm i\phi} \, d\Omega \right|^2 \\
 &= 0,
 \end{aligned} \tag{3.11}$$

where  $j_1$  is the first order spherical Bessel function. Based on these results, one can see that the neutron tends to push the  $H_2$  molecule into a rotational wavefunction where the molecule axis is aligned with the momentum transfer. Classically, this can be understood by imagining the  $H_2$  molecule as a dumbbell. If the neutron hits the dumbbell perpendicular to its axis, the dumbbell will gain rotational energy and tend to rotate to align with the transferred momentum. However, if the neutron hits the dumbbell parallel to its axis, it will not be able to transfer rotational energy to the bar. These new theoretical results could be confirmed by taking neutron scattering spectra from hydrogen adsorbed on graphite with a given orientation relative to the momentum transfer at a high enough energy transfer to see the roto-vibrational transitions. If the momentum transfer is perpendicular to the adsorption plane, vibrational transitions of the adsorption potential will be observed. If the momentum transfer is parallel to the adsorption plane, vibrational transitions of the adsorption potential will not be observed. However, it is likely that transitions of the translational motion

parallel to the adsorption plane will still be observed; but it is not known what form they will take. If our treatment of classical motion along the plane is an accurate approximation, these transitions may be well approximated by free recoil scattering. Q-dependent experimental data is needed to address this issue. If free recoil scattering is not adequate, a more sophisticated theoretical treatment would need to be developed.

When hydrogen is adsorbed, its rotational wavefunctions are aligned in the  $z$ -direction (perpendicular to the graphite plane) or parallel to the  $xy$  plane. If the momentum transfer is at an angle  $\vartheta$  to the  $z$  axis, the form factors for the  $p_z$  and  $p_x, p_y$  states are given by

$$F_{s \rightarrow p_z}(q) = 12b_{inc}^2 j_1^2\left(\frac{qa}{2}\right) \cos^2 \vartheta. \quad (3.12)$$

$$F_{s \rightarrow p_x, p_y}(q) = 12b_{inc}^2 j_1^2\left(\frac{qa}{2}\right) \sin^2 \vartheta. \quad (3.13)$$

The vibrational part of the form factor must be calculated numerically using the wavefunctions calculated in the previous section

$$F_{n \rightarrow n'}(\vec{q}) = |\langle \psi_{n, \alpha, w}(z) | e^{-izq \cos \vartheta} | \psi_{n', \alpha', w}(z) \rangle|^2, \quad (3.14)$$

where  $w$  is the width of the slit. The complete form factors as calculated using Eqs. (3.8), (3.12), (3.13), and (3.14) for a 6 Å and 8 Å slit are shown in Figure 3.4 for the momentum transfer parallel to the  $z$ -axis.

The Debye-Waller factor is given by

$$2W = \frac{1}{3}q^2 \langle U^2 \rangle = (q_z^2 \langle z^2 \rangle + q_{xy}^2 \langle x^2 + y^2 \rangle). \quad (3.15)$$

The value of  $\langle z^2 \rangle = \langle \psi_{n, w}(z) | (z - \langle z \rangle)^2 | \psi_{n, w}(z) \rangle$  gives the variance of position perpendicular to the adsorption plane and is calculated based on the wavefunctions for

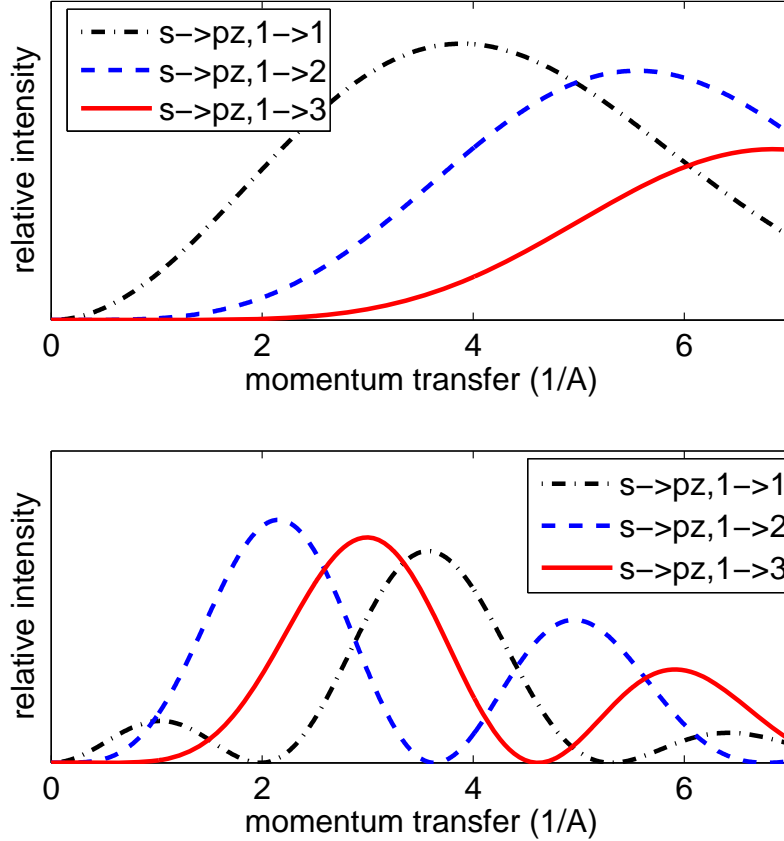


Figure 3.4: Form factors for the first three roto-vibrational transitions for a 6 Å slit (top) and a 8 Å slit (bottom) where the momentum transfer is parallel to the z-axis. The oscillatory nature of the latter set of form factors reflects the fact that the wavefunctions are bimodal.

each slit width. For a single sheet, this value was calculated to be  $0.066 \text{ \AA}^2$ . Figure 3.5 shows  $\langle z^2 \rangle$  as a function of slit width. The discontinuity at  $w = 8.4 \text{ \AA}$  is due to the double-layer adsorption that occurs above this size, which was discussed in the previous section. For pores below this width, the variance increases significantly with pore size.

The value of  $\frac{1}{2}\langle x^2 + y^2 \rangle$  describes the variance of position parallel to the adsorption plane and we approximate it as independent of slit width. Nielsen and Ellenson [47,91] did inelastic scattering from para-hydrogen adsorbed on Grafoil oriented parallel with the scattering plane and found this value to vary from  $0.14 \text{ \AA}^2$  at low coverage to  $0.094 \text{ \AA}^2$  at high coverage. We will use the latter value, as the experimental neutron

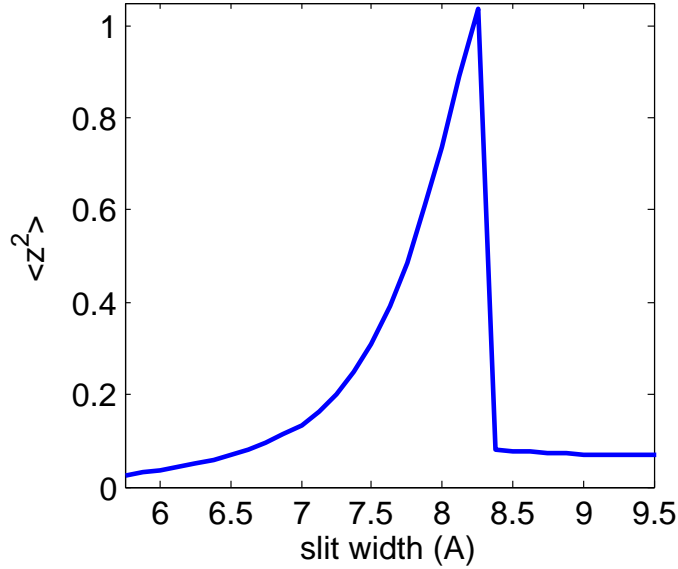


Figure 3.5: The variance of position perpendicular to the adsorption plane as a function of slit width. The discontinuity at  $w = 8.4$  Å is due to double-layer adsorption, which localizes the molecules motion perpendicular to the plane more strongly and results in a smaller variance.

scattering data for hydrogen adsorbed on activated carbon shown in Figure 3.1 is shown for a nearly complete monolayer.

### 3.4 Results

Using the transition energies and scattering cross section calculated in the previous sections, spectra were calculated for different slit-shaped pores for the range  $w=7-9.5$  Å. The measurements shown in Figure 3.1 were performed on the inverted geometry crystal analyzer instrument TOSCA [92] at ISIS. The instrument has a fixed final energy of 3.98 meV and collects scattered neutrons at angles of  $42.5^\circ$  for forward-scattering and  $137.5^\circ$  for back-scattering. At a neutron energy transfer of  $\hbar\omega = 14.7$  meV, where the first rotational transition for free  $\text{H}_2$  molecules occurs, the momentum transfer is  $q_b = 4.1\text{\AA}^{-1}$  for back-scattering. For comparison purposes, spectra were calculated to match these back-scattering conditions.

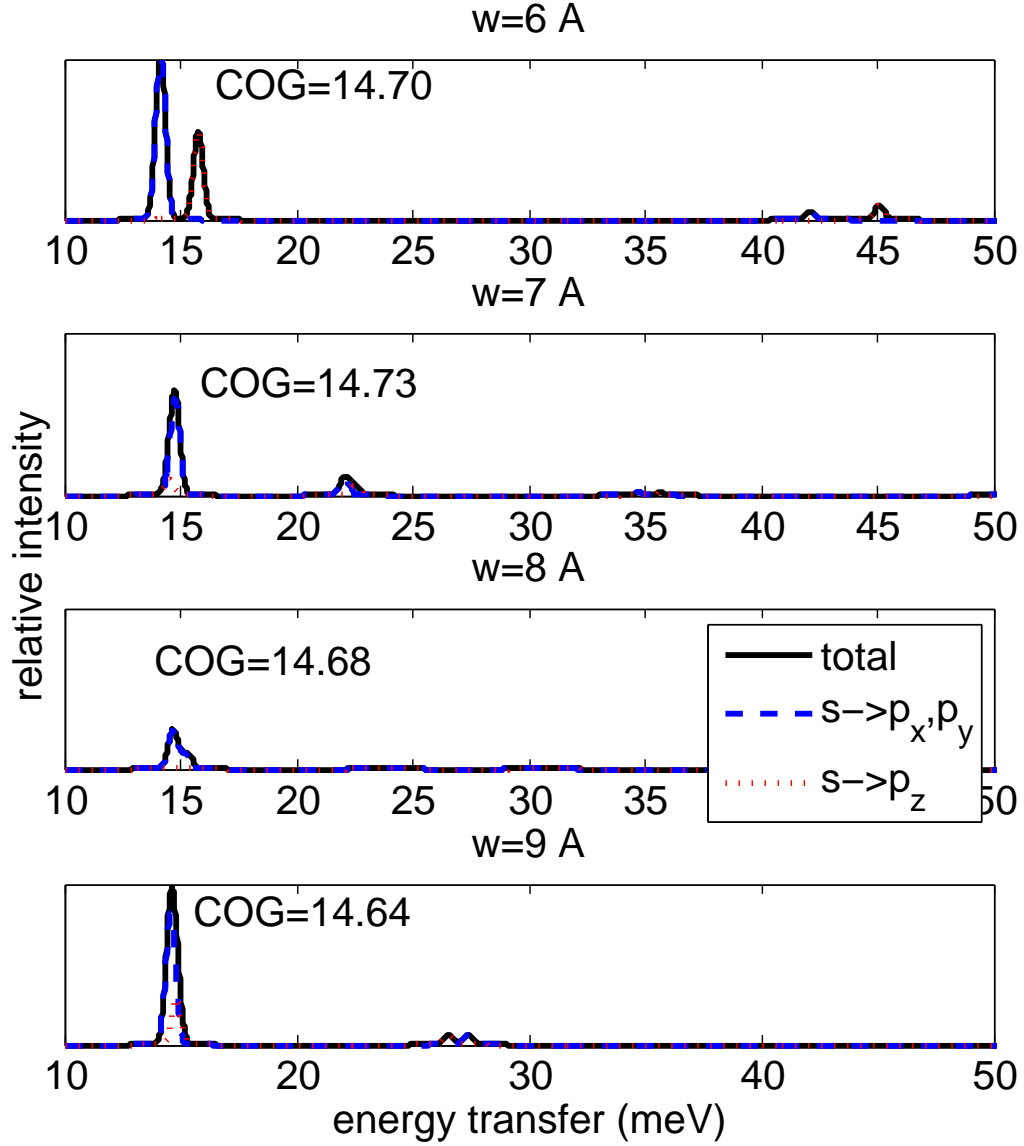


Figure 3.6: Calculated neutron scattering spectrum at monolayer coverage for  $\text{H}_2$  adsorbed in slit-shaped pores with widths  $w=6,7,8,9 \text{ \AA}$ . The spectra, shown in solid black, is split up into  $s, 1 \rightarrow p_z, n'$  and  $s, 1 \rightarrow p_x, p_y, n'$  transitions. The center of gravity (COG) for the pure rotational transitions is shown on each.

Figure 3.6 shows calculated spectra for hydrogen adsorbed in slit shaped pores with widths  $w=6,7,8,9 \text{ \AA}$ , where the relative orientation of  $\vec{q}$  and the graphene plane has been taken to be isotropic by averaging over  $\vartheta$  in Eqs. (3.12) and (3.13). The center of gravity (COG) for the pure rotational transitions is shown for each. The COG is shifted from the 14.7 meV at which it is observed for gaseous hydrogen. A

similar shift of 0.05-0.2 meV downwards has been observed experimentally [47, 71–75] for  $\text{H}_2$  adsorbed on SWCNT, AC, and Grafoil. In our calculations, this shift is attributable to several factors. Firstly, the adsorption potentials for the different rotational states have different zero-point energies. This effect is heavily dependent on pore size, but not on the magnitude of the momentum transfer. Secondly, the effects of adjacent hydrogen molecules act to further shift the transition energies of different rotational states. This effect is likely independent of pore size and the magnitude of the momentum transfer, but should be dependent on the coverage. Finally, the Debye-Waller factor for momentum transfer perpendicular to the adsorption plane is also different for different sizes of slits, and generally acts to reduce the magnitude of the  $s \rightarrow p_z$  transitions, lowering the COG. This effect strongly depends on the pore size and the magnitude of the momentum transfer. Experimentally, taking data which is q-dependent and coverage dependent from a variety of samples may help to differentiate between these effects.

For the  $w = 6 \text{ \AA}$  slit (Figure 3.6, top), the rotational transitions are strongly split and the vibrational transitions are at a high energy transfer. This is due to the very narrow adsorption potential that occurs at this pore size. For the  $w = 7 \text{ \AA}$  slit (Figure 3.6, second from top), the  $s \rightarrow p_z$  transition now occurs at a lower energy than the  $s \rightarrow p_x, p_y$  transitions. This shift is caused by effects of the adjacent hydrogen molecules. In addition, the wider pore results in a larger Debye-Waller factor, reducing the magnitude of the  $s \rightarrow p_z$  transitions. The sum effect is an increase in the COG for this size slit. For the  $w = 8 \text{ \AA}$  slit, which is nearly large enough for bi-layer adsorption to occur, (Figure 3.6, second from bottom), the Debye-Waller factor in z direction is so large that the  $s \rightarrow p_z$  transitions are barely visible. In addition, the energy levels are so close that the first roto-vibrational transition is now at nearly the same energy as the pure rotational transition, resulting in the appearance of a split rotational transition. For the  $w = 9 \text{ \AA}$  slit (Figure 3.6, bottom),

bi-layer adsorption now occurs. There is no observable splitting of the rotational transition, and the COG now occurs at 14.64 meV, comparable to the 14.65 meV at which Georgiev [75] finds a peak for hydrogen adsorbed in activated carbon. The vibrational transitions occur at an average energy of 27 meV, comparable to the 27.5 meV at which Georgiev et al. [75] also finds a peak. It is likely, then, that the sample of activated carbon used for their experiment contained a significant proportion of pores that are wide enough for two full layers of hydrogen to adsorb.

Figure 3.7 shows the calculated spectra for a sample of activated carbon that has a uniform pore size distribution for  $w = 5.75\text{--}9.5 \text{ \AA}$ . This spectrum again shows a large narrow peak for the  $(s, 1) \rightarrow (p, 1)$  transition at 14.6 meV as well as a broad band from 14.7 to 60 meV that covers the  $(s, 1) \rightarrow (p, n' \neq 1)$  transitions. Comparing with the experimental data for activated carbon, shown on the right of Figure 3.1, the shape appears to be similar. Differences in shape could be explained by a non-uniform pore size distribution. However, the ratio of the intensity of the second broad peak (the roto-vibrational transitions) to the intensity of the first narrow peak (the pure rotational transition) seems to be considerably larger in the experimental data than in the calculated spectra.

There are some possible reasons for this disparity. Firstly, this calculation has neglected the possibility of transitions of the vibrational motion parallel to the adsorption plane. However, these transitions would likely be observed in the experimental data. There are two possibilities for these transitions. Either the approximation of classical motion parallel to the adsorption plane is accurate and free recoil scattering would be observed, or the hydrogen molecules could be localized along the adsorption plane, not just by the graphene potential, but by the effects of adjacent hydrogen molecules. The latter type of transitions would vary heavily with coverage, as adjacent molecules are squeezed more closely to one another. In addition, calculations of these transitions would be more complex, as the effects of adjacent molecules can not

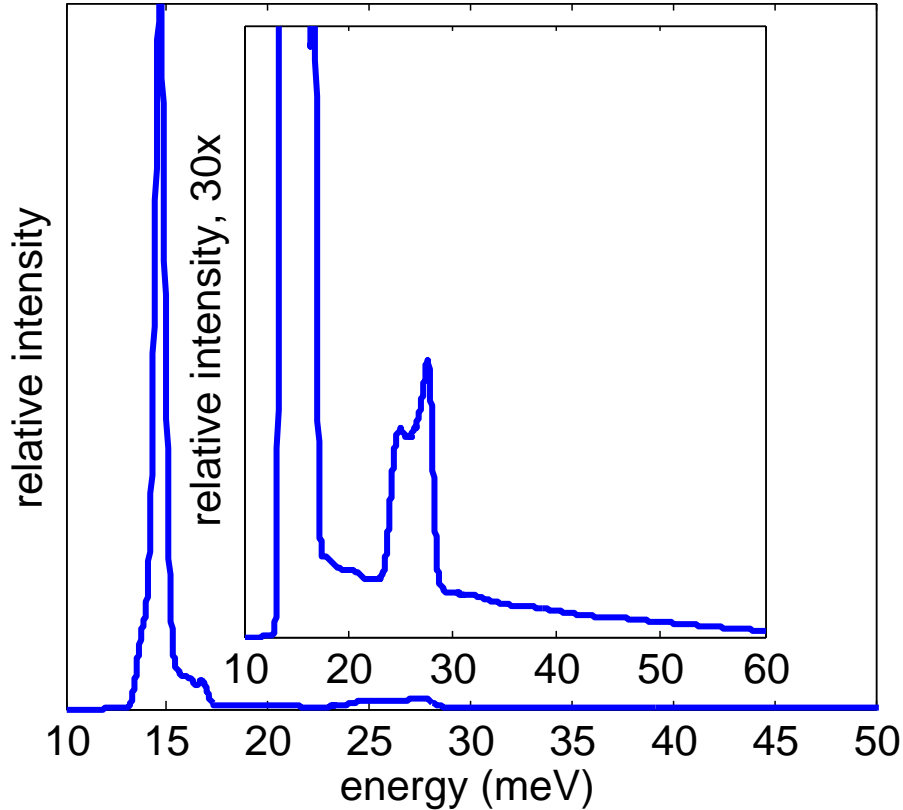


Figure 3.7: Calculated neutron scattering spectrum at monolayer coverage for  $\text{H}_2$  adsorbed on activated carbon composed of a uniform distribution of slit-shaped pores with widths  $w=5.75\text{--}9.5$  Å. The inset shows the same spectra at a magnification of 30.

be treated simply as a first-order perturbation. Experimental data which addresses this issue is shown in the next chapter.

Another reason for this disparity could be the approximation that the pores are infinite and slit-shaped, i.e., they are formed of parallel planar graphene structures of relatively large dimensions. Transmission electron microscopy images of activated carbon [93] show evidence of non-hexagonal rings in the carbon structure, which results in substantial curvature of the surface in all directions. Terzyk et al. [94,95] have proposed a fullerene-like fragment model which takes into account the random curvature that would be expected in such structures. In cases where the pores are drastically different than the slit-shaped pores considered in our calculations, the rotational and

vibrational degrees of freedom can no longer be treated as independent. Because the form factor depends heavily on the wavefunctions, the transition probabilities will change significantly as the structure changes. On the other hand, the energies at which the transitions occur are less dependent on the details of the structure and seem to be in the same range for the calculated and experimental spectra.

Another issue that could affect the form factors significantly is the form of the potentials used. We have used the Xu H<sub>2</sub>-C potential [88] because it allows for calculation of the potential as a function of the orientation of the hydrogen molecule. However, this potential assumes the form of a quasi Lennard-Jones potential which may result in an incorrect shape, again an issue that would affect the form factors more significantly than the transition energies. Obtaining q-dependent measurements may help to determine the accuracy of the form factors calculated here.

### 3.5 Summary

In conclusion, we have calculated both the vibrational and rotational transition energies for slit-shaped pores of a variety of widths. In pores with widths on the order of 8 Å, the vibrational and rotational transition energies are very close to one another, calling into question analysis techniques which consider only the rotational transitions. In contrast to previous works which have treated the problem as isotropic, we have calculated form factors and Debye-Waller factors as a function of the relative angle between the adsorption plane and the momentum transfer. The resulting spectra are most heavily influenced by this anisotropy when the pore is slightly too small for bi-layer adsorption. We have also found a shift in the center of gravity of the rotational transitions, which has also been observed experimentally. This shift is dependent on the pore size, and results from a combination of three factors: the different shape and thus zero-point energies of the different rotational states, the effects

of adjacent adsorbed hydrogen molecules , and the anisotropy of the Debye-Waller factor. A spectrum was calculated for a uniform distribution of pores and compared with previously published experimental data. Only qualitative agreement was found, suggesting the theory is not yet complete. Likely explanations for the observed disparity include the neglect of transitions in the translational motion parallel to the adsorption plane, a significantly different pore shape, or incorrect potentials.

It seems that even at the current level of theoretical understanding, IINS may provide useful information about important length scales for sub-nm pore characterization. Experimental work is shown in Chapter 4 that compares samples with significantly different adsorption characteristics, providing the opportunity to directly learn more about the adsorption environment of the hydrogen molecules in these samples based on the difference between their spectra.

# Chapter 4

## Analysis of Experimental Inelastic Neutron Scattering Spectra from Hydrogen adsorbed in Carbon Adsorbents

### 4.1 Introduction

Previous work on incoherent inelastic neutron scattering as a complementary characterization technique for hydrogen adsorbents, both theoretical [16–19] and experimental [71–86], has been focused on an analysis of the rotational transitions, which occur at an energy of approximately 14.7 meV and give information about the anisotropy of the H<sub>2</sub> adsorption potential. Only one previous experimental paper [75] has shown spectra at high enough energy transfers, around 29 meV, at which roto-vibrational transitions can be observed. Pure vibrational transitions, which should occur at an energy of approximately 14 meV, are not observed because they occur with a probability which is proportional to the coherent cross section, which is 40 times smaller than the incoherent cross section. In addition, very little mention has been made of

the possibility of free recoil transitions. If such transitions occur, a robust knowledge of their character is required in order to properly subtract them from the background of the spectra, enabling a correct analysis of the rotational and roto-vibrational peaks. We have previously published theoretical calculations [16], discussed in Chapter 3, which find the transition energies of roto-vibrational transitions. In addition, we demonstrated that the neutron tends to excite the molecule to rotational states in which the molecule axis tends to be aligned with the momentum transfer and use this fact to address the anisotropy of the form factors. Continued theoretical work in this area is needed to develop IINS as a robust characterization technique, particularly for heterogeneous materials.

In this chapter, we present experimental IINS spectra for  $\text{H}_2$  adsorbed in four different carbon samples. The carbon samples and experimental procedure are discussed in Section 4.2. This data extends to high enough energy transfers to easily observe roto-vibrational transitions, as well as a tail of transitions extending from the main rotational peak which we attribute to free recoil, though with an effective mass which is only about a third of the mass of a free hydrogen molecule. The possibility of interference between the different types of transitions is discussed in Section 4.3. Spectra were measured as a function of both energy transfer and momentum transfer, a fact which aids considerably in the fitting of the data. Details of the data analysis are given in Section 4.3, where the anisotropy of the problem is used to effectively split the spectra into transitions in which the momentum transfer is parallel or perpendicular to the adsorption plane. In Section 4.4 results are presented which compare spectra from different samples and at different coverages, and conclusions are discussed in Section 4.5.

## 4.2 Experimental Methods

Four carbon adsorbents were studied. Sample AX-21 MSC-30 is a KOH-activated carbon produced commercially by Kansai Coke and Chemicals which is widely used in the adsorption community as a standard sample because of its high surface area of  $2600 \text{ m}^2/\text{g}$  (as measured by nitrogen adsorption [12, 15]) and a large proportion of nanopores. Sample 3K is a KOH activated carbon produced at the University of Missouri from a corncob precursor which has a surface area of  $2700 \text{ m}^2/\text{g}$ . Sample HS;0B is also manufactured at the University of Missouri in a two stage process by the pyrolysis of poly(vinylidene chloride-co-vinyl chloride) (PVDC) and has a surface area of  $700 \text{ m}^2/\text{g}$ . Hydrogen and nitrogen adsorption data for these samples are given in Chapter 2 [15]. Sample 3K outperforms MSC-30 in cryogenic excess adsorption by about 15%, an enhancement which is explained in part by its slightly larger surface area. Because these two activated carbon samples are so similar, only spectra for 3K will be presented. On the other hand, the cryogenic excess adsorption of HS;0B is about 80% of MSC-30, despite having nearly a quarter of the surface area. This odd behavior is discussed further in Chapter 5. Multi-Wall Carbon Nanotubes (MWNT) of outer diameter  $>8\text{nm}$  with a surface area of  $500 \text{ m}^2/\text{g}$  were purchased commercially. Because the nanotubes are capped and have a large outer diameter, they offer a nominally flat and relatively homogeneous adsorption surface which can be used to compare with our previous calculations in Chapter 3 [16] and the other samples.

Samples were prepared by out-gassing at  $125 \text{ }^\circ\text{C}$  in a vacuum oven at a pressure of  $10^{-7}$  bar for 12 hours. Approximately 0.5 g of the sample was transferred under a helium atmosphere into an aluminum sample cell of cylindrical geometry with an inner diameter of 0.6 cm and height of 6 cm. The lid of the sample cell was fitted with capillary tubing to allow the addition of hydrogen gas in situ. Glass wool was

added to the top of the cell to prevent migration of carbon grains.

The experiments were performed on the wide-angular range chopper spectrometer (ARCS) at the Spallation Neutron Source at Oak Ridge National Laboratory. This spectrometer provides a monochromatic beam with tunable incident energy and is able to measure intensity as a function of both energy transfer  $w$  and momentum transfer  $Q$ . The sample cell was loaded into a closed-cycle refrigerator and connected to a gas handling system. After a leak test was performed with helium, the system was flushed with molecular hydrogen three times, pumping down to  $10^{-7}$  bar between each flushing. The sample cell was loaded into the beam path and the temperature was set to 30 K. After the temperature was reached, a background signal of the aluminum can and carbon sample was taken at incident energies of 30 and 90 meV.

Hydrogen gas was loaded into the sample by filling a known volume at room temperature to a given pressure, which was calculated based on the number of adsorption sites. The number of adsorption sites was calculated using the sample mass, sample specific surface area, and a surface area per adsorption site of  $\alpha = 10.7 \text{ \AA}^2$ , a value taken from neutron diffraction studies of solid  $\text{H}_2$  adsorbed on Grafoil [47]. Data was taken at estimated coverages of 60% and 90% of a full monolayer. For two samples, data was also taken at loadings of 120% coverage. After the room temperature volume was filled, a valve to the sample was opened. Because the sample was at 30 K, gas quickly condensed as observed by the drop in pressure of the room temperature volume. After approximately 20 minutes, the temperature of the sample was lowered to 15 K and more gas was allowed to condense. The pressure of the room temperature volume was recorded at the beginning of data collection in order to calculate the actual coverage, which was typically within 1% of the desired coverage.

The neutron beam was then turned on with an incident energy of 30 meV and short successive spectra were collected. The spectra were compared to observe the population of spin states as a function of time. The  $J = 0 \rightarrow 1$  peak at an energy

transfer of  $w = 14.7$  meV was observed. Over time, its height increased as more of the molecules reached the ground spin state. In addition, the  $J = 1 \rightarrow 0$  peak at  $w = -14.7$  meV was observed and its height decreased over time as molecules decayed from the first excited state. When the difference between successive runs was within error bars, final data collection was begun. The process took 0.5-2 hours depending on the sample and coverage.

After the conversion process, signals were taken at incident energies of 30 and 90 meV. Typical spectra, with the sample can and carbon powder background subtracted are shown in Figure 4.1.

### 4.3 Data Analysis

The peak intensity as a function of energy transfer for the MWCNT sample at 60% coverage is shown in Figure 4.2. This function has a peak at an energy transfer of  $w = 14.5$  meV, which we identify as the first rotational  $J = 0, N = 1 \rightarrow J = 1, N = 1$  transition. Its location is at a slightly lower energy transfer than the  $w = 14.7$  meV of the free gas and the  $w = 14.6$  meV which we found in Chapter 3 [16] for adsorption on a flat graphite sheet. A similar downward shift of 0.1-0.2 meV from the free gas position has been measured by other groups [47, 71–75] for H<sub>2</sub> adsorbed on SWCNT, AC, and Grafoil. In addition, a peak is also observed at an energy transfer of  $w = 28.6$  meV, which we confidently identify as the first roto-vibrational  $J = 0, N = 1 \rightarrow J = 1, N = 2$  transition due to the fact that its position is within 1 meV of the  $w = 27.7$  meV which we found in Chapter 3 [16] for adsorption on a flat graphene sheet. Both of these peaks are observed in all of the spectra.

Another feature common to all of the spectra is a tail extending from the first rotational transition which passes through the roto-vibrational transition. Figure 4.2 also shows the momentum transfer of the peak intensity for each energy transfer along

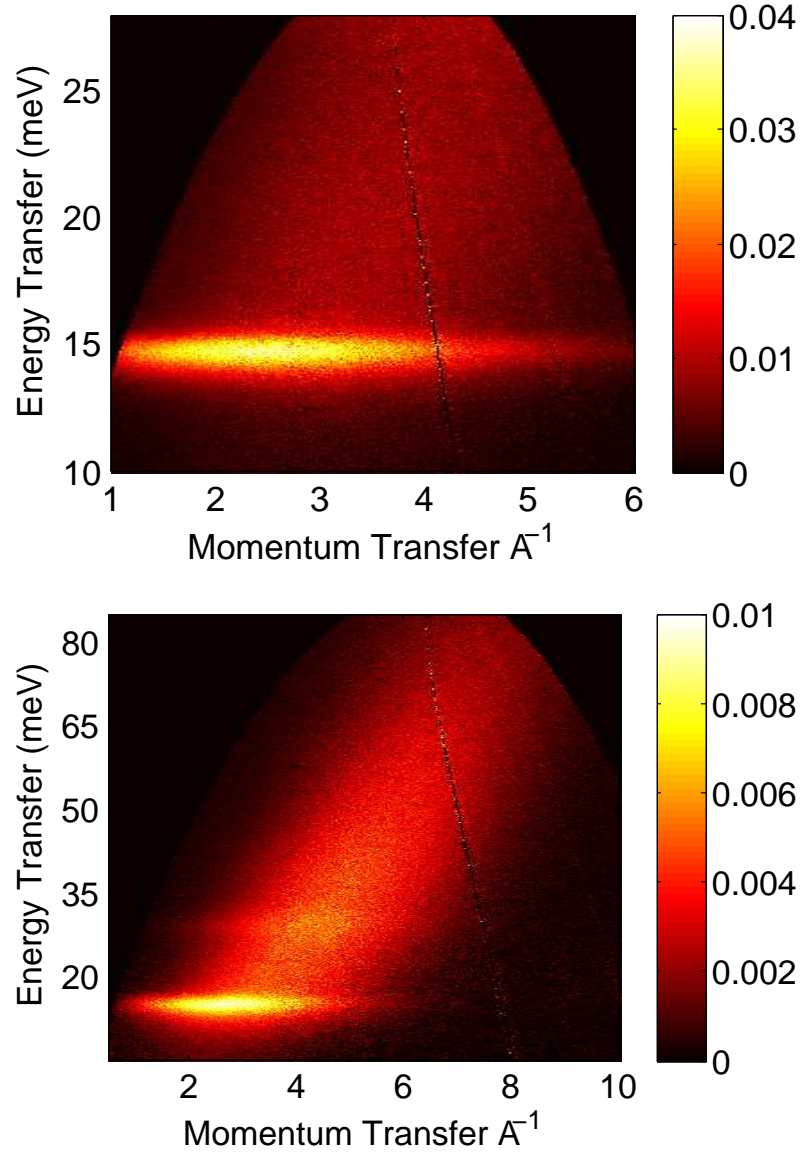


Figure 4.1: Inelastic neutron scattering spectra for the MWCNT sample at 60% coverage with incident energies of 30 meV (top) and 90 meV (bottom).

with a quadratic fit to this data over the energy transfer ranges  $w = 17\text{--}23$  and  $w = 32\text{--}63$  meV, ranges chosen to exclude the main rotational and roto-vibrational peaks. Because a quadratic function is a reasonably good fit, one might hypothesize that this part of the spectra represents free recoil transitions in the translational motion of the adsorbed  $\text{H}_2$  molecules parallel to the adsorption plane, in addition to a rotational transition. Based on this reasoning, we will henceforth refer to this tail as roto-recoil

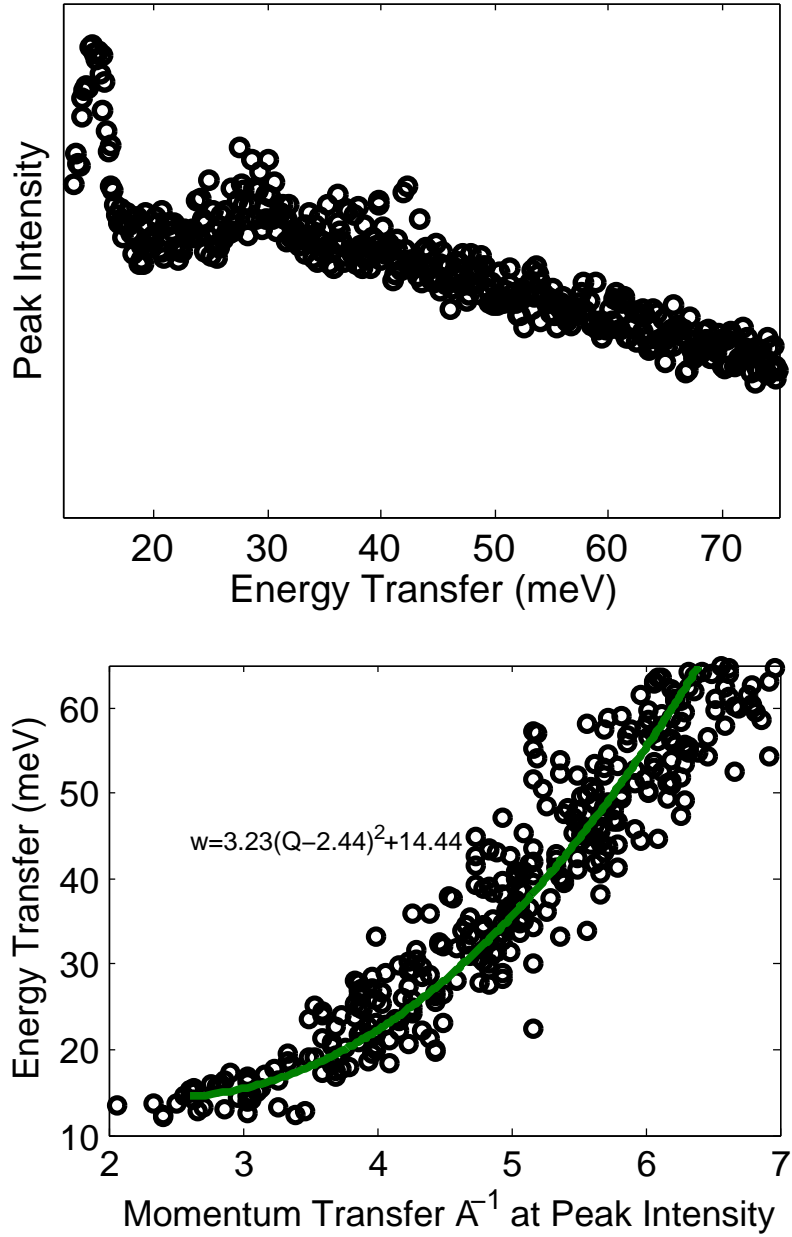


Figure 4.2: Peak intensity as a function of energy transfer (top) and momentum transfer of the peak intensity (bottom) calculated from the spectra for the MWCNT sample at 60% coverage with incident energy of 90 meV.

transitions. However, using the free recoil energy of  $(\hbar Q)^2/2M$ , the effective mass of this fit is  $M = 0.62 m_p$  where  $m_p$  is the mass of a proton, significantly smaller than the mass of a hydrogen molecule. Previous experimental work [75,96] at high enough momentum transfers that the impulse approximation holds have demonstrated

a free recoil spectrum with mass  $2 m_p$ . However, our spectra are at smaller values of momentum transfer where the impulse approximation does not apply. Previous theoretical work in the slow neutron limit [97] calculates an effective mass using mass tensor formalism for  $H_2$  of  $1.23 m_p$ , still quite different than our value. An effective mass of  $3.40 m_p$  was also calculated for methane, significantly different than the experimental value of  $2.71 m_p$  found for methane hydrate [98]. Therefore it is clear that theoretical work remains to be done in this area.

Another hypothesis is that there is some interference [99] between the roto-recoil states and the roto-vibrational state, meaning that the final state of the  $H_2$  molecule is some linear combination of a molecule which has undergone a roto-recoil and a roto-vibrational transition. This effect would clearly be highly dependent on the direction of the momentum transfer relative to the adsorption plane, as for  $Q$  parallel to the adsorption plane one would expect only roto-recoil transitions and likewise for  $Q$  perpendicular to the adsorption plane one would expect only roto-vibrational transitions. However, for intermediate directions of  $Q$ , interference is theoretically possible. Thus it may be that the presence of the roto-vibrational transition modifies the effective rotational mass of the molecule. This possibility is supported by the fact that the roto-recoil tail overlaps the roto-vibrational peak in both energy and momentum transfer in Figure 4.1(b). In addition, it is clear from Figure 4.2(a) that a single function does not well describe the peak intensity of the tail. It may be possible to resolve this question by collecting comparative spectra from free liquid hydrogen, where a roto-vibrational peak is not expected, and observing the roto-recoil tail would help to understand this feature.

Because of this complication, we will not perform any analysis of the roto-vibrational peak other than to note its nominal location in each spectra (keeping in mind the ability of interference to move peak locations). Instead we will limit our analysis to energies less than 23 meV, which are too small to observe a roto-vibrational transi-

tion. In Chapter 3 we showed [16] that the neutron tends to excite the H<sub>2</sub> molecule into a rotational state which is aligned with the momentum transfer. Thus the analysis of the rotational peak will be done by making the simplifying assumption that the momentum transfer either tends to be parallel to the adsorption plane, in which case free recoil transitions in addition to a rotational transition in which the molecular axis is parallel to the adsorption plane occur, or tend to be perpendicular to the adsorption plane, in which case a rotational transition in which the molecular axis is perpendicular to the adsorption plane occurs. In doing this, we ignore the possibility of observing a free recoil transition when the excited rotational state has the molecular axis perpendicular to the adsorption plane, which using our previous theoretical treatment [16] that separates the rotational and translational degrees of freedom, should be theoretically possible for intermediate orientations of  $Q$ . This assumption is supported by the fact that the quadratic fit shown in Figure 4.2 extends from  $w_0 = 14.4$  meV. This value corresponds more closely to the  $w_{\parallel} = 14.6$  meV at which we calculated the rotational transition for  $Q$  parallel to the adsorption plane for a flat graphene sheet than the  $w_{\perp} = 14.8$  meV at which we calculated the rotational transition for  $Q$  perpendicular to the adsorption plane.

We find that the following function describes the  $Q$ -dependence of the roto-recoil transitions well,

$$S_{\parallel}(Q, w) = A(w)F_{\parallel} \left( Q - \frac{1}{\hbar} \sqrt{\frac{w - w_0}{2M}} \right) e^{-B(w)Q^2}, \quad (4.1)$$

where  $F_{\parallel}$  is based on our previous calculations [16] and is found by integrating the form factors over all possible orientations of  $Q$ , assuming cylindrical symmetry

$$F_{\parallel}(Q) = F_{J=0 \rightarrow 1}(Q) \frac{3}{4} \int_0^{\pi} F_{J=0, J_{\perp}=0, N=1 \rightarrow 1, \pm 1, 1}(Q \cos \theta) \sin^3 \theta d\theta. \quad (4.2)$$

The angle  $\theta$  is given relative to the normal of the adsorption plane. The values of

$A(w)$  and  $B(w)$  are determined by a fit of Eq. 4.1 to the spectrum at each value of the energy transfer in the ranges  $w = 17\text{--}23$  and  $w = 32\text{--}63$  meV, which are outside of the main rotational and roto-vibrational peaks. The Debye-Waller factor  $B(w)$  is well described over both of these ranges by an exponentially decaying function of  $w$ . A significant difference in the slope of  $A(w)$  is observed between the two ranges as expected given Figure 4.2(a), supporting the possibility of interference between the roto-recoil tail and roto-vibrational transition. However, within the range  $w = 17\text{--}23$  meV, a linear function describes  $A(w)$  well. The fits of  $A(w)$  and  $B(w)$  are then used to calculate  $S_{\parallel}(Q, w)$  over the range  $w = 14\text{--}23$  meV and subtracted from the experimental spectrum.

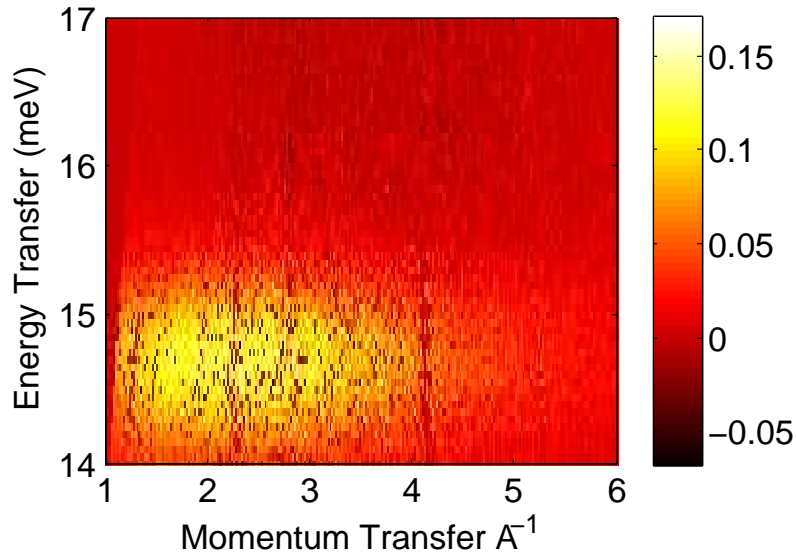


Figure 4.3:  $S_{\perp}(Q, w)$ , found by extending fits to  $S_{\parallel}(Q, w)$  into the main rotational peak and subtracting from the spectrum for the MWCNT sample at 60% coverage with incident energy of 30 meV.

The result  $S_{\perp}(Q, w)$  is shown in Figure 4.3 and appears to be a well defined peak centered at  $w_{\perp} = 14.7$  meV, corresponding well to our calculated value for  $w_{\perp}$ . It appears that our simplifying assumption is well-supported, with both  $w_{\parallel}$  and  $w_{\perp}$  found to be about 0.1–0.2 meV smaller than our calculated values [16]. In a similar

manner, the following function can then be used to fit  $S_{\perp}(Q, w)$

$$S_{\perp}(Q, w) = C(w)F_{\perp}(Q)e^{-D(w)Q^2}, \quad (4.3)$$

where  $F_{\perp}$  is similarly given by

$$F_{\perp}(Q) = F_{J=0 \rightarrow 1}(Q) \frac{3}{2} \int_0^{\pi} F_{J=0, J_{\perp}=0, N=1 \rightarrow 1, 0, 1}(Q \cos \theta) \cos^2 \theta \sin \theta d\theta, \quad (4.4)$$

and the fit subtracted from the experimental spectrum in order to determine  $S_{\parallel}(Q, w)$  below  $w_0 = 14.5$  meV. The function  $C(w)$  is found to be well described by a gaussian and  $D(w)$  by a constant.

## 4.4 Results

Figure 4.4 shows the results of the analysis for the MWCNT sample at 60% coverage. For both incident energies, the analysis reveals a sharp peak with a gaussian shape centered at 14.7 meV for  $Q$  tending to be perpendicular and a peak centered at 14.0 meV which appears to have a lorentzian shape with a free recoil tail extending from the high energy side for  $Q$  tending to be parallel.

The gaussian shape of the  $S_{\perp}(Q, w)$  peak implies that molecules which are in an excited rotational state and have their molecular axis tending to be perpendicular to the adsorption plane are bound and do not diffuse along the plane. The lorentzian shape of the  $S_{\parallel}(Q, w)$  peak, as well as the fact that the free recoil tail extends from it, implies that molecules which are in an excited rotational state and have their molecular axis tending to be parallel to the adsorption plane are not bound and do diffuse along the adsorption plane. This is a very surprising result. In our previous theoretical treatment [16] in which we have treated the rotational and translation degrees of freedom as separate, there is no particular reason why the rotational state

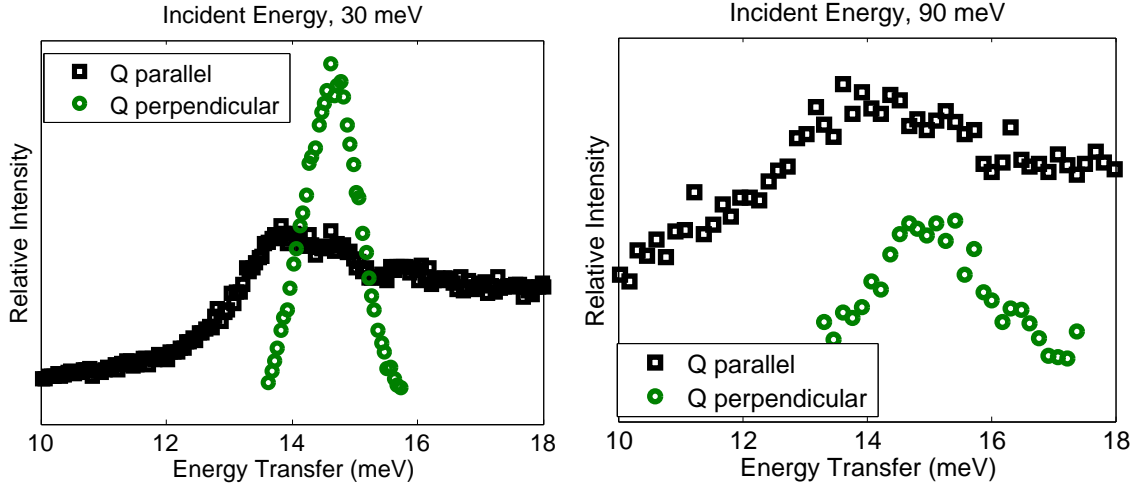


Figure 4.4: Maximum intensity as a function of energy transfer of  $S_{\parallel}(Q, w)$  and  $S_{\perp}(Q, w)$  for the MWCNT sample at 60% coverage at incident energies of 30 meV (left) and 90 meV (right).

should be related to the diffusive motion of a molecule. Because we have shown that the molecular axis of a rotational state that has been excited by a neutron tends to align with the momentum transfer, and because free recoil states are excited only when the momentum transfer has a significant component parallel to the adsorption plane, the probability of an incoming neutron exciting a state in which the molecular axis is perpendicular to the adsorption plane, but the molecule recoils parallel to the plane should be low, but still non-zero. But in fact, the significantly different shape of the two peaks implies that the probability is exactly zero and that the alignment of the rotational state is inextricably linked to the direction of translational motion of a molecule.

For an incident energy of 30 meV, the resolution of the instrument is 0.7 meV around the region of the rotational peak. For an incident energy of 90 meV, the resolution of the instrument is 2.3 meV, which is over three times as large. The resultant increased broadening of the peaks for the 90 meV incident energy can clearly be seen in Figure 4.4, therefore we will use the 90 meV incident energy spectra only to compare the position of the roto-vibrational peak. Another significant difference

lies in the relative probability of the two types of transitions. For an incident energy of 30 meV, the intensity of  $S_{\perp}(Q, w)$  is much larger, whereas for an incident energy of 90 meV, the intensity of  $S_{\parallel}(Q, w)$  is significantly increased. This is sensible because  $S_{\parallel}(Q, w)$  includes the free recoil part of the spectrum and higher energy neutrons are more likely to excite free recoil transitions.

The maximum intensity as a function of energy transfer of the spectra before the analysis described in the previous section is applied, is plotted in Figure 4.5 for each sample. The spectra have been normalized by the amount of hydrogen in the sample cell. For an incident energy of 90 meV, the roto-vibrational peak is observed at  $w \approx 29$  meV for all of the samples. Our calculations [16] have shown that the position of the roto-vibrational peak moves quite significantly for pores under 9 Å in width. Thus the results imply that 3K and HS;0B both contain few very small pores. The main rotational peak at 14.5 meV is slightly broadened for 3K, consistent with the hypothesis that this sample is slightly more heterogeneous than the MWCNT sample, but still contains very few small pores. The rotational peak of sample HS;0B is significantly broadened, implying a highly heterogeneous sample with many very small pores, a hypothesis which is entirely inconsistent with the position of the roto-vibrational peak. In addition, despite normalizing by the amount of hydrogen in the sample cell, all of the transitions appear to be more likely for HS;0B.

Let us turn to the analysis technique described in the previous section to see if the conflicting results for HS;0B can be understood. The maximum intensity as a function of energy transfer of  $S_{\perp}(Q, w)$  and  $S_{\parallel}(Q, w)$  for each sample is shown in Figure 4.6. The  $S_{\perp}(Q, w)$  peak is quite similar for all samples, being centered at an energy transfer of  $w_{\perp} = 14.7$  meV. It is slightly broadened for samples 3K and HS;0B, suggesting more heterogeneous samples with few very small pores, entirely consistent with the roto-vibrational peak. The area under the curve is also similar for all of the samples. Instead, the major difference in the spectra of HS;0B is found

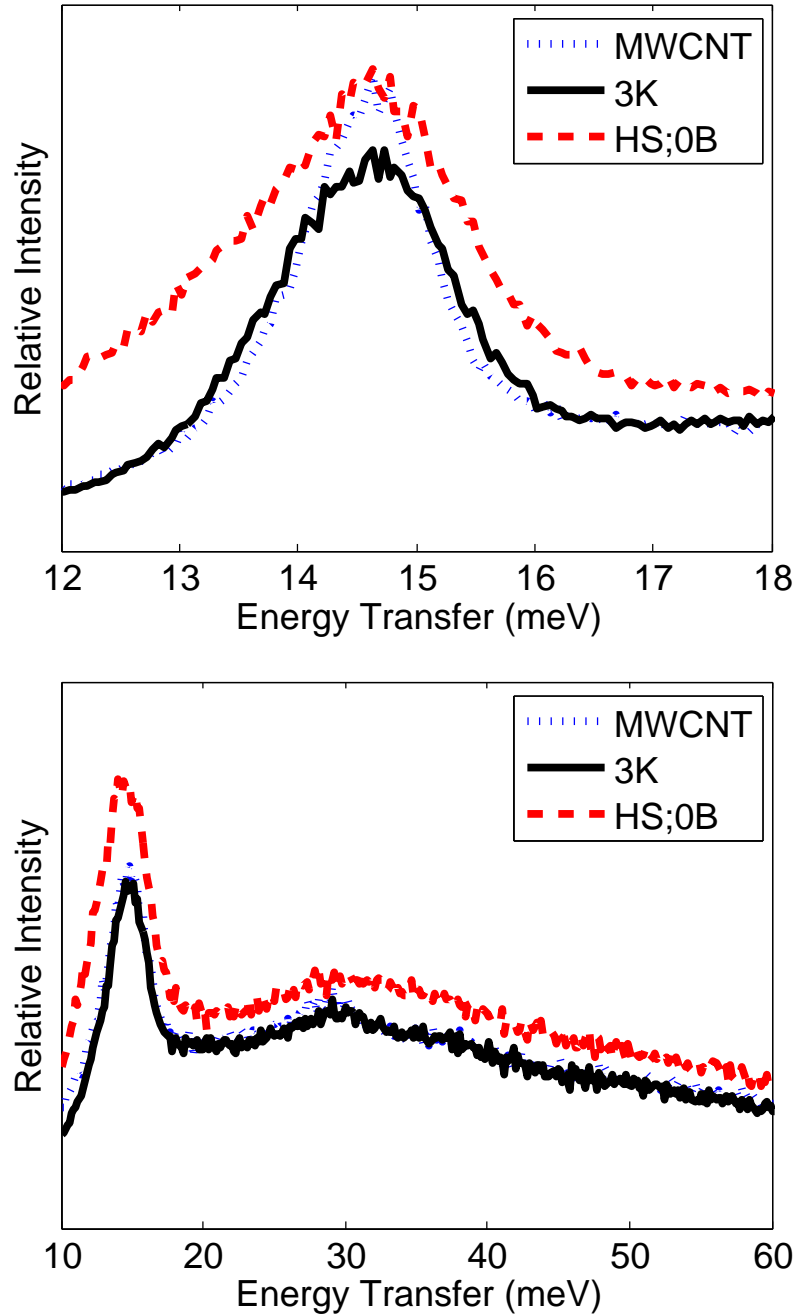


Figure 4.5: Maximum intensity as a function of energy transfer at incident energies of 30 meV (top) and 90 meV (bottom) for samples MWCNT, 3K, and HS;0B at a coverage of 60%. Spectra have been normalized by the amount of hydrogen in the sample cell.

to be contained in the  $S_{||}(Q, w)$  peak. While it is quite similar for the MWCNT sample and 3K, being centered at an energy transfer of  $w_{\perp} = 14.0$  meV, for HS;0B it

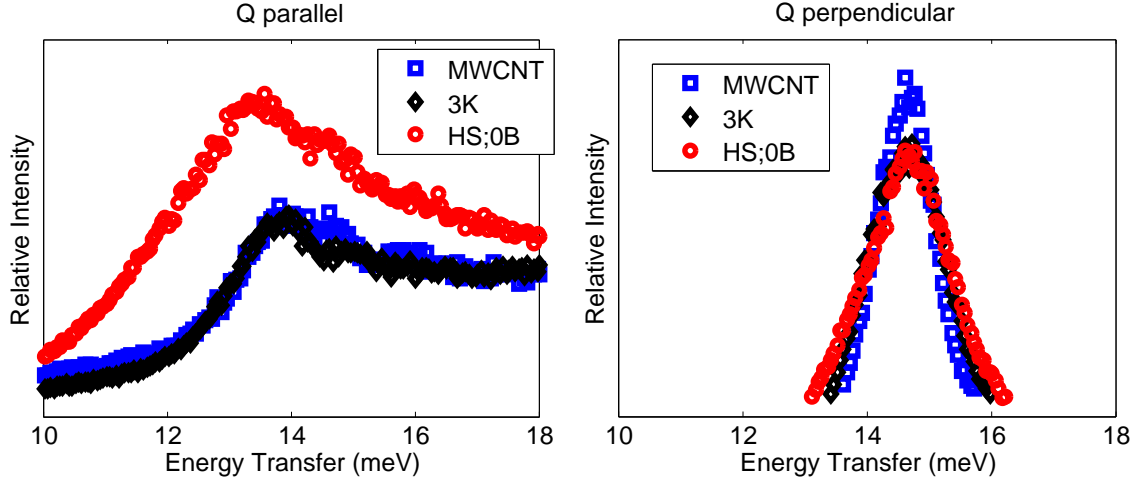


Figure 4.6: Maximum intensity as a function of energy transfer of  $S_{\parallel}(Q, w)$  (left) and  $S_{\perp}(Q, w)$  (right) at an incident energy of 30 MEV for samples MWCNT, 3K, and HS;0B.

is shifted to an energy transfer of  $w_{\perp} = 13.5$  meV as well as being significantly larger with an average  $\approx 40\%$  larger intensity, an increase which is asymmetrically found on the low-energy side.

Asymmetrical broadening of scattering peaks has been previously explained by Fano [99] as an interference between a discrete state and a continuum. In this case, the discrete case is the rotational peak, and the continuum would be the free recoil states. Under normal circumstances, the two do not interfere because the rotational state is independent of position. However, one could imagine that in contiguous curved pores, the rotational state varies slowly as a function of position along the pore, thus it is possible that the asymmetrical broadening seen in the spectrum of HS;0B indicates the presence of long curved pores. We will return to this issue in Chapter 5, where other experimental evidence of the structure of this sample will be presented.

The  $Q$  dependence of the different types of transitions is shown in Figure 4.7. Eqs. 4.2 and 4.4 were used to analyze the rotational peaks. In a similar manner, the

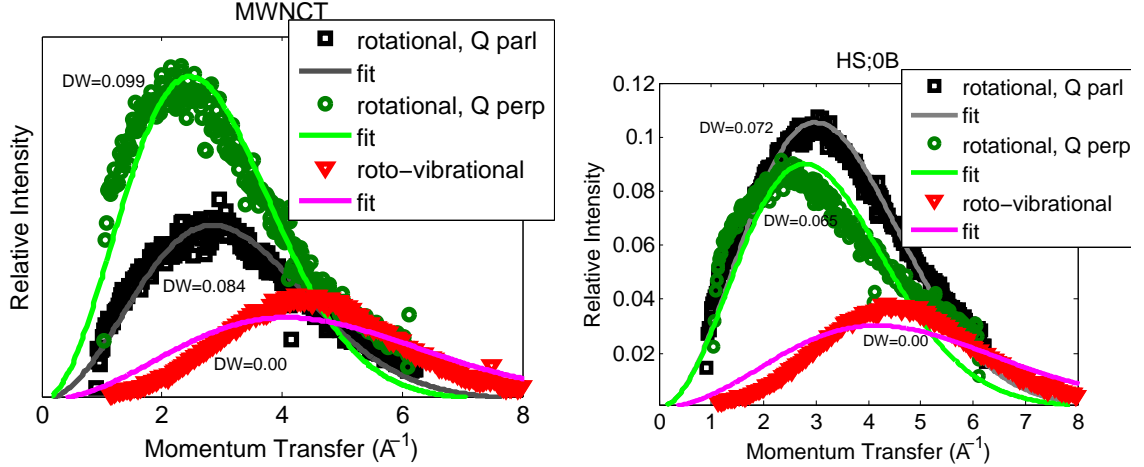


Figure 4.7: Q dependence of rotational peak of  $S_{\parallel}(Q, w)$  and  $S_{\perp}(Q, w)$  and the roto-vibrational peak for the MWCNT (left) sample and HS;0B (right) at 60% coverage.

vibrational peak has been analyzed using

$$F_v(Q) = F_{J=0 \rightarrow 1}(Q) \frac{3}{2} \int_0^{\pi} F_{J=0, J_{\perp}=0, N=1 \rightarrow 1, 0, 2}(Q \cos \theta) \cos^2 \theta \sin \theta d\theta. \quad (4.5)$$

The fits to the rotational peaks are fairly good shown in Figure 4.5, with minor differences in shape which are primarily on the large  $Q$  side. The fact that these differences in shape are similar for both the parallel and perpendicular peaks indicate that a main component of the difference between the theoretical calculations and the experimental spectra lies in  $F_{J=0 \rightarrow 1}$ . A likely reason for this difference lies in our assumption that the rotational states can be approximated by the free rotor wavefunctions. This hypothesis could be examined by obtaining similar spectra for unadsorbed hydrogen for comparison purposes. Conversely, the fit to the vibrational peak is not as good. Because all of the results seem to indicate the presence of few very small pores, it is unlikely that the reason for this is based on the pore model, since as the pore size increases, the effect of pore shape on the results diminishes. Instead, we hypothesize that a likely explanation lies in the  $H_2$ -C potential used. Minor differences in the potential create only small errors in the transition energies,

but affect the wavefunctions and thus form factors much more significantly.

Table 4.1: Debye-Waller factors for the rotational peak of  $S_{||}(Q, w)$  and  $S_{\perp}(Q, w)$  for each sample at each coverage.

coverage	$  $ 60%	$  $ 90%	$  $ 120%	$\perp$ 60%	$\perp$ 90%	$\perp$ 120%
MWCNT	0.084	0.079		0.099	0.091	
MSC-30	0.087	0.079		0.103	0.090	
3K	0.088	0.079	0.078	0.099	0.086	0.081
HS;0B	0.072	0.070	0.0666	0.065	0.066	0.056

The Debye-Waller factors for each fit are also shown in Figure 4.7, and Table 4.1 gives them for all of the samples and coverages for the rotational peaks. For the MWCNT and activated carbon samples, the results are all quite similar. In general, as the coverage increases from 60% to 90%, the Debye-Waller factor decreases by about 10%, indicating the molecules are more localized at higher coverages. However, the results are quite different for HS;0B. The Debye-Waller factors are on average 25% smaller, but do not decrease significantly as the coverage increases to 90%, although they do then decrease as the coverage increases to 120%.

The coverage dependence of the results can be correlated with absolute adsorption isotherms which are given in Figure 4.8. These isotherms have been calculated from excess hydrogen adsorption isotherms taken at 80 K, using methods which we have previously described in Chapter 2 [15]. The adsorption isotherm for HS;0B is unusually large. We will leave a discussion of this for the next chapter, however it is interesting to note that for 3K, at 60% coverage, the isotherm is in the low pressure regime where the slope of the adsorption is still large and interactions of adjacent hydrogen molecules theoretically have a small effect. For HS;0B, the isotherm is in this regime at both 60% and 90% coverage, so this may explain the fact that there is little change in the Debye-Waller factors between these two coverages. Collecting

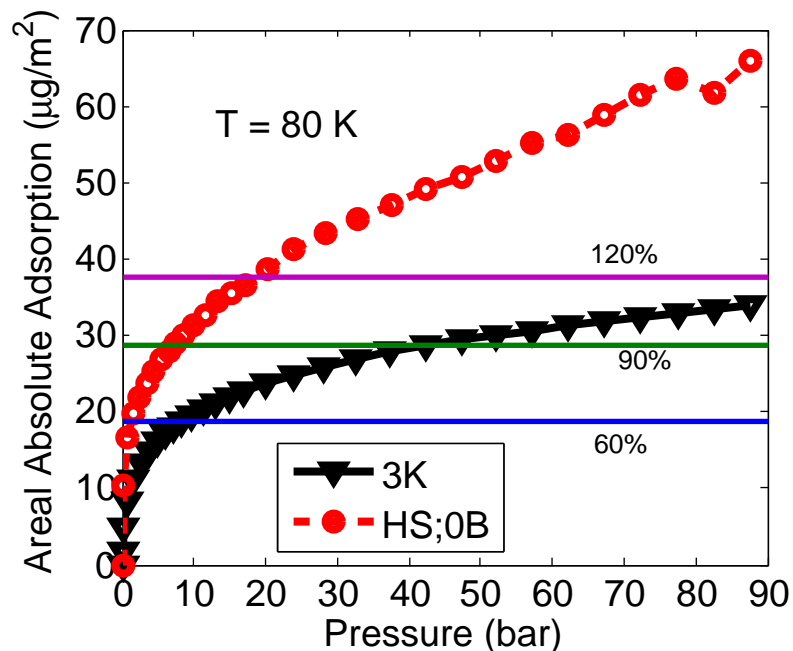


Figure 4.8: Areal absolute adsorption hydrogen isotherms calculated from excess adsorption isotherms taken at a temperature of 80 K.

experimental spectra at a wider variety of coverages, particularly in the low coverage regime may help to elucidate this difference.

The maximum intensity as a function of energy transfer of  $S_{\perp}(Q, w)$  and  $S_{\parallel}(Q, w)$  at each coverage for samples 3K and HS;0B is shown in Figure 4.6. For sample 3K, it is apparent that the analysis technique becomes less effective at separating the two components as the coverage increases. This likely reflects increasing heterogeneity in the adsorption sites occupied as the coverage increases. For HS;0B this is only a small issue. In general, the peak locations do not vary as a function of coverage and the area under the curve for  $S_{\perp}(Q, w)$  is also largely consistent. However, the area under the curve for  $S_{\parallel}(Q, w)$  decreases as a function of coverage. This may reflect the increasing effect of adjacent hydrogen molecules on the likelihood of free recoil transitions.

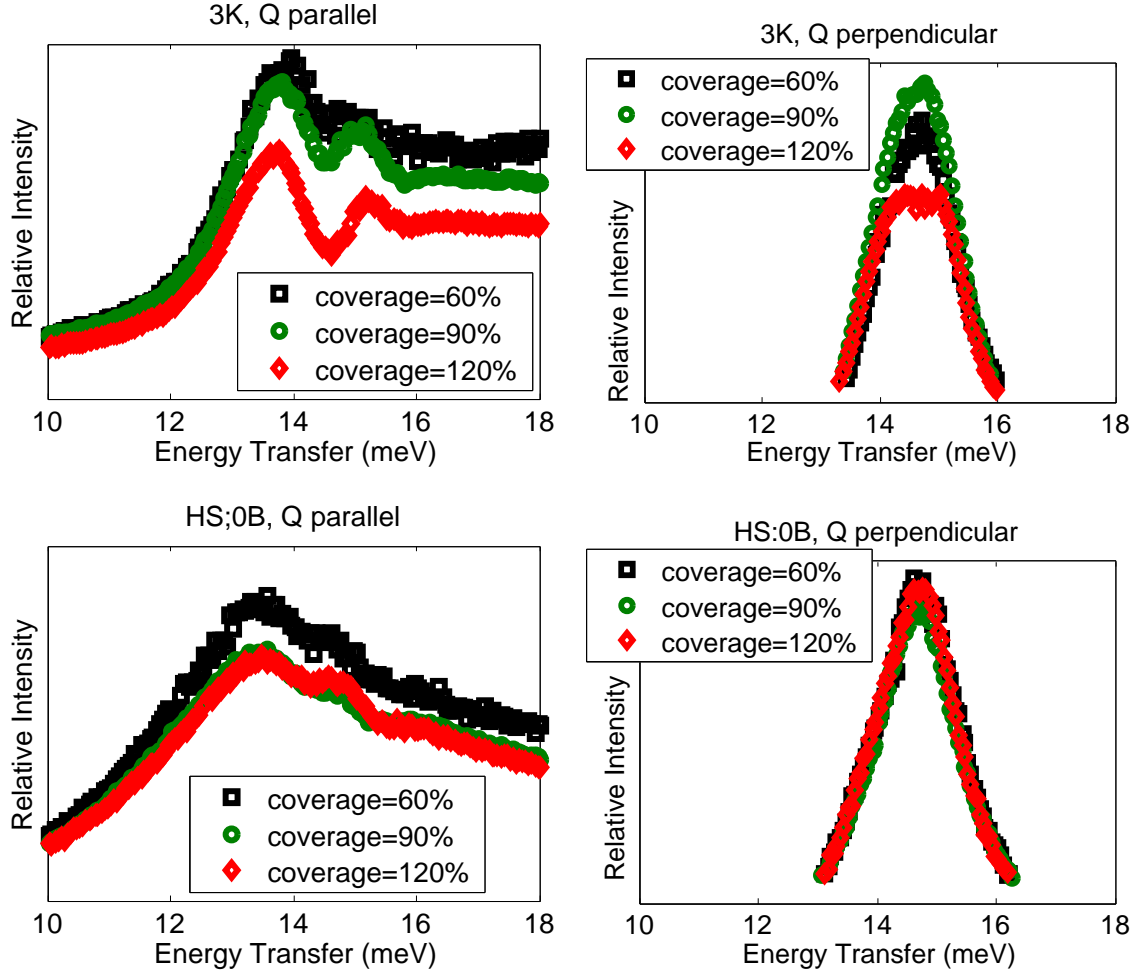


Figure 4.9: Maximum intensity as a function of energy transfer of  $S_{\parallel}(Q, w)$  (left) and  $S_{\perp}(Q, w)$  (right) at an incident energy of 30 meV for samples 3K (top), and HS:0B (bottom). Curves are shown for each value of the coverage, and have been normalized by the amount of hydrogen in the sample cell.

## 4.5 Summary

We have shown experimental inelastic neutron scattering spectra for a number of samples. The results compare well with the theoretical calculations of Chapter 3, with less than 1 meV difference in the locations of the main peaks. The most significant difference between the theoretical calculations and experimental results is in the presence of transitions between the main rotational and roto-vibrational peaks, which we ascribe to excitations of the translational motion of the adsorbed  $H_2$  molecules along

the adsorption plane. However, it seems likely that either a change in the effective rotational mass or some interference between the different types of transitions modifies their behavior significantly, thus there is still much work to be done in understanding these transitions.

We have also described a novel analysis technique which separates the spectra into two different parts, with the momentum transfer tending to be either parallel or perpendicular to the adsorption plane. This analysis technique is based on the assumption that the recoil transitions occur only when the momentum transfer tends to be parallel to the adsorption plane, thus rather than being simply a complicated background signal that must be removed, the recoil transitions are shown to be an important part of the spectra that is integral to its proper analysis. The transitions for  $Q$  tending to be perpendicular have a gaussian shape suggesting a bound state, whereas the transitions for  $Q$  tending to be parallel have a lorentzian shape, suggesting that these states are the ones which tend to undergo diffusive motion along the plane.

Most of the spectra are very similar to one another, with the main differences reflecting slightly greater sample heterogeneity for the activated carbon samples and an increased effect of adjacent hydrogen molecules as a function of coverage. However, the spectra for sample HS;0B are greatly different. Naively, this suggests a highly heterogeneous sample, but more sophisticated analysis shows that in fact all of the difference between the spectra is in the diffusive states. The location of the main rotational peak for this part of the spectrum is shifted to a significantly lower energy, and in addition, transitions to all of the states are more likely. This would seem to suggest that molecules adsorbed in this sample undergo much more diffusive motion along the plane. However, this is exactly contrary to the fact that the Debye-Waller factors for this sample are smaller, which generally suggests that the molecules are more localized. As we will show in the next chapter, contradictory conclusions about this sample are not unusual, and it is clear that much work remains to be done

to understand the structure of this sample and how it affects both the adsorption characteristics and its INS spectrum.

# Chapter 5

## Anomalous Characteristics of a PVDC Carbon Adsorbant

### 5.1 Introduction

Hydrogen storage by adsorption in porous carbon materials such as activated carbon (AC), amorphous carbon nanotubes, single-wall carbon nanotubes (SWCNT) and porous carbon has been previously studied by many research groups [65]. Carbon based adsorbants are attractive due to their low cost, chemical stability, and ease of use. Currently, room temperature storage in carbon based adsorbants is far from meeting both gravimetric and volumetric DOE targets. Classical adsorption theory [11] says that adsorption can be significantly improved by either increasing the surface area or the binding energy of the adsorbant. Current carbon based samples have achieved surface areas as high as  $3100 \text{ m}^2/\text{g}$ , a value which is above the theoretical limit of the surface area of a sample composed of infinite sheets of graphene, but still do not come close to reaching the targets. Theoretically, the only way to increase the binding energy of pure carbon samples is to create very small pores in which the binding potential created by both walls overlap significantly [42, 67, 68]. However,

not only is this result difficult to achieve experimentally, but significant narrowing of the pores generally comes with an attendant decrease in effective surface area due to the ability of pores under 8.5 Å in width to hold only a single layer of hydrogen, rather than the bi-layer adsorption which occurs in larger pores. As a result, research has turned away from pure carbon adsorbants, with focus moving towards carbon adsorbants doped with materials such as boron [69,100] or materials with completely different chemical structures.

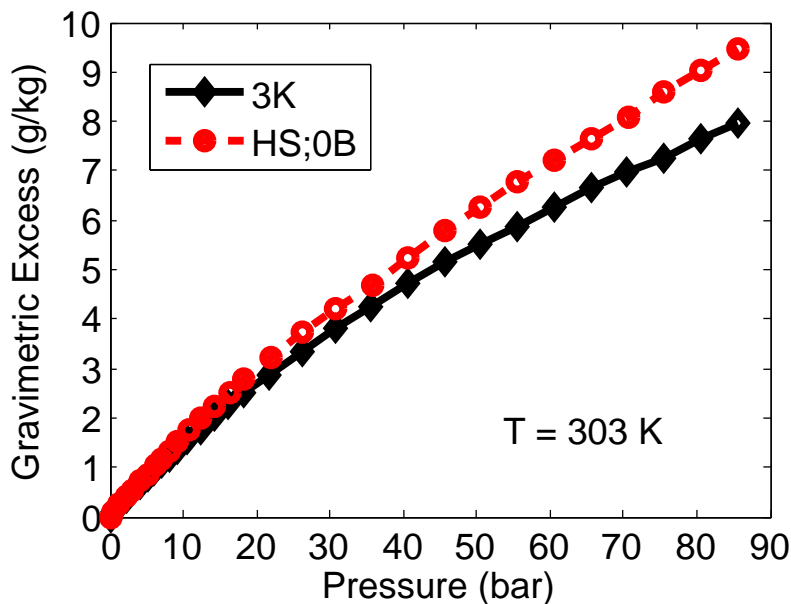


Figure 5.1: Gravimetric excess hydrogen adsorption at 303 Kelvin.

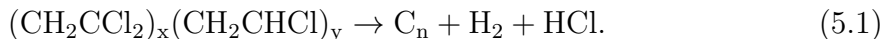
Figure 5.1 shows the room temperature gravimetric excess hydrogen isotherms for two carbon adsorbants produced by The Alliance for Collaborative Research in Alternative Fuel Technology (ALL-CRAFT) [8] at the University of Missouri. Sample 3K is a KOH activated carbon with a corncob precursor which slightly outperforms sample AX-21 MSC-30, the current industry standard activated carbon. Sample HS;0B is a carbon produced by the pyrolysis of poly(vinylidene chloride-co-vinyl chloride) PVDC, the manufacture of which is described in more detail in Section 5.2. Amazingly enough, HS;0B outperforms 3K in room temperature gravimetric storage despite

having a quarter of the surface area and a fifth of the pore volume. The structural characterization of this sample is discussed in more detail in 5.3. As a consequence of this latter fact, the room temperature volumetric storage of this sample is significantly larger than other samples. Isotherms were run multiple times to confirm these results, and details of the thermodynamic characterization are given in 5.4.

Sample HS;0B is of high interest not only because of its high room temperature adsorption, but because every single experimental result which has been obtained for this sample is quite unusual, and are often in contradiction with one another when classical adsorption theory is used to understand them. While one or two unique results may simply suggest experimental error, the confluence of all of these results suggests that there may be some novel adsorption phenomenon at work in this sample. If so, any new theory which explains these results might likewise reveal a pathway to create even more impressive experimental achievements. In Section 5.5 a number of competing hypotheses are given which attempt to explain all of the experimental data in a consistent manner.

## 5.2 Samples

HS;0B is manufactured at the University of Missouri and is prepared in a two stage process by the pyrolysis of poly(vinylidene chloride-co-vinyl chloride) (PVDC). The chemical formula for this process is



In the first stage, 10.0 g of powdered PVDC is placed in a 500 ml glass round-bottom schlenk flask under an inert atmosphere and capped. The flask is placed in a room temperature oven, and the temperature is set to 230 °C. A Teflon tube is fitted to

the flask stopcock and vented into a mineral oil bubbler outside of the oven. After the temperature is reached, it is maintained for 3 hours. During this stage, vigorous outgassing is apparent in the oil bubbler. The powder, initially dense and a light tan color, begins to melt and darken, then foam. By the end of the stage, outgassing has ceased and the sample is black and solid. Its volume has increased significantly, nearly filling the flask, and many macroscopic pores can be seen. The sample also has a shiny appearance. The sample is allowed to return to room temperature, and then is removed from the flask under an inert atmosphere. During the removal, the solid foamy block of the sample has to be broken up into a powder, which still has a very low density and is quite electrostatically charged. Approximately 4 g of sample remain. In the second stage, the sample is placed in a stainless steel tube. The end of the tube containing the sample is placed into a tube furnace, and the other end is connected to a vacuum pump. The furnace is then set to 900 °C and maintained at this temperature for 2 hours. After this stage, the tube is allowed to cool to room temperature, then the sample is removed under an inert atmosphere. Approximately 3 g of sample remain, but little difference in appearance is observed.

Data on other PVDC samples has been previously published, either for hydrogen adsorption [101] or for other applications [88]. However, there have been significant differences in the production method, resulting in unimpressive hydrogen adsorption and/or differences in the structure of the final material.

Elemental analysis was performed on HS;0B by Columbia Analytical Services. The sample exhibited significant variability, thus given mass weight percents are averages of multiple measurements. Carbon (83%), hydrogen (1.1%), and nitrogen (0.7%) percentages are determined concurrently using direct measurement that includes sample combustion at 935 °C followed by thermo-conductivity detection (TCD) or IR detection on resulting CO<sub>2</sub>, H<sub>2</sub>O, and N<sub>2</sub> gases. In addition oxygen (1.4%) and chlorine (5.2%) content are determined by O<sub>2</sub> flask/IC. Samples are prepared by acid di-

gestion and metal analysis is performed by ICP-OES. Metals found in significant amounts are, in decreasing order, aluminum, antimony, calcium, sodium, iron, and magnesium.

When preparing samples for measurements, it is usual practice to outgass the sample under vacuum at temperatures above 100 °C. A white film appears in the stopcock of the flask containing the sample at temperatures between 150 and 400 °C whenever this procedure is done for HS;0B. If the flask is then exposed to the atmosphere the film begins to turn orange, suggesting the presence of iron. A KimWipe was used to remove the film from the flask and the wipe was subjected to back-scattered electron energy density spectroscopy (BSE EDS) analysis [102] at an accelerating voltage of 20 kV and working distance of 10-12 mm using a FEI Quanta 600F Environmental scanning electron microscope (SEM) at high vacuum. Samples were mounted on standard SEM imaging stubs with double sided carbon stick tape. The results were compared with a clean wipe. Its spectra contained peaks for carbon and oxygen, with trace amounts of silicon, calcium, chlorine, and copper. The spectra for the wipe exposed to the film contained peaks for carbon and oxygen, larger peaks for chlorine and iron, and trace amounts of calcium, potassium, aluminum, silicon, and tantalum. Thus it appears the film is mainly composed of chlorine and iron. We hypothesize that during the second stage of the manufacturing process, iron sublimates from the stainless steel and combines with chlorine outgassing from the carbon matrix to form this film.

For comparison purposes, data will also be presented on 3K, a KOH activated carbon produced from a carbonized corncob precursor also manufactured at the University of Missouri, which we have shown in Chapter 2 [15] to be quite similar to MSC-30. When data on 3K is unavailable, AX-21 MSC-30, produced by the Kansai Coke and Chemicals Co. Ltd., Japan, will be used.

### 5.3 Structural Characterization

The specific surface area  $\Sigma$  is determined from sub-critical nitrogen isotherms measured at the University of Missouri by an Auorosorb-1C (Quantachrome Instruments), using Brunauer-Emmett-Teller (BET) theory in the pressure range of 0.01 to 0.03  $P/P_0$  suitable for microporous materials. The pore volume  $V_p$  is determined at a pressure of 0.995  $P/P_0$  and includes only pores with widths under approximately 300 nanometers. Table 5.1 gives the surface area and pore volume for each sample. 3K has a surface area and pore volume typical of high end activated carbons. Sample HS;0B has about a quarter of the surface area and a fifth of the pore volume of 3K. These smaller values are consistent with the lack of activation and typical for other PVDC samples in the literature [103]. Quenched solid density functional theory (QS-DFT) is used to calculate pore size distributions (PSDs). Figure 5.2 shows the pore size distribution for each sample calculated using QSDFT. 3K has a wide variety of pore sizes, perhaps resulting from its origins in biological materials or the aggressive activation process. On the other hand HS;0B, which is produced by a more controllable chemical process, has a much narrower distribution of pore sizes, with the main peak at 8 Å and a smaller peak at approximately 30 Å.

Competing methods of calculating pore size distributions such as non-local density functional theory (NLDFT) assume flat graphitic pore structure without taking into account the effects of surface roughness. QSDFT, provided by Quantachrome's data reduction software, is a modified version of (NLDFT) that takes into consideration surface roughness and heterogeneity, making this method suited for disordered carbon materials. Such a model has significant drawbacks if it is applied to activated carbons where layering transitions are obstructed due to geometrical and chemical heterogeneities. Consequently, this may lead to false minimums in the pore size distribution, an artifact which has been completely eliminated by QSDFT where the

solid is modeled using the distribution of solid atoms rather than the source of the external potential field. Pore size distributions calculated using NLDFT show false minimums for both samples. In addition, the small pore peak for both samples is shifted to about 12 Å, rather than 8 Å as in the QSDFT pore size distribution. Further details of these methods can be found in [13, 14].

Table 5.1: Sample Characteristics: Specific surface area  $\Sigma$ , micropore volume  $V_p$ , apparent density  $\rho_a$ , bulk density  $\rho_b$  and bulk density after compression  $\rho_c$ .

sample	$\Sigma$ (m <sup>2</sup> /g)	$V_p$ (cm <sup>3</sup> /g)	$\rho_a$ (g/cm <sup>3</sup> )	$\rho_b$ (g/cm <sup>3</sup> )	$\rho_c$ (g/cm <sup>3</sup> )
3K	2,700	1.68	0.46	0.14	0.34
HS;0B	700	0.34	1.19	0.15	0.95

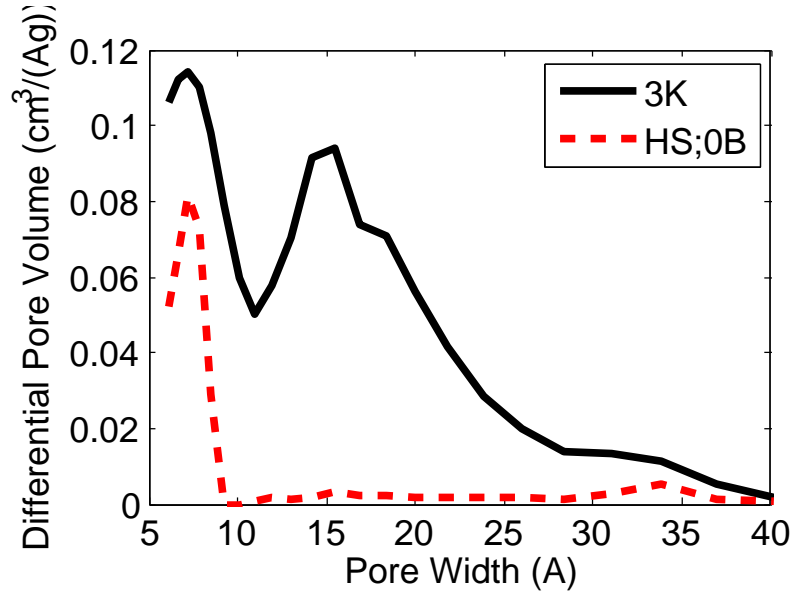


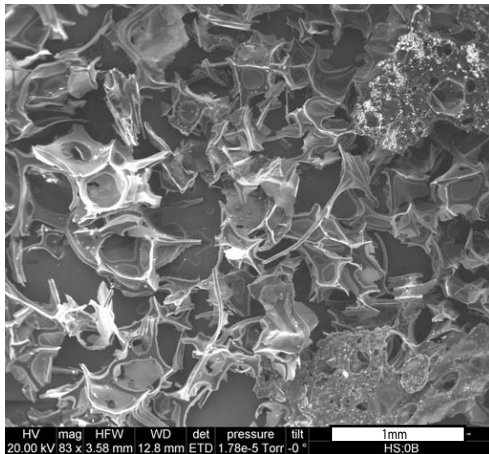
Figure 5.2: Pore size distributions calculated using QSDFT methods.

Table 5.1 also gives several densities for the samples. The apparent density  $\rho_a$  is the theoretical maximum density which assumes there are no macropores. It is calculated by adding the specific micropore volume to the specific volume of the

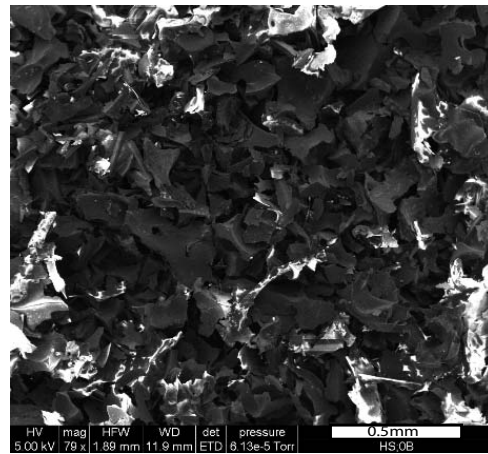
carbon, assuming the density of the carbon matrix is  $\rho_s = 2 \text{ g/cm}^3$ , and taking the inverse. The bulk density  $\rho_b$  is the density of the bulk material which is calculated by measuring the mass and volume of a given amount of sample which has been packed by hand. For both samples, the bulk density is significantly smaller than the apparent density, a fact which would significantly affect the volumetric density of hydrogen stored in these materials, as gas is stored in macropores simply at the ambient gas density. The density was measured again after the sample was packed under pressures of 7000 psi, giving the compressed bulk density  $\rho_c$ . For both samples, the compressed bulk density is about 75–80% of the apparent density and there was no significant change in the pore volume, surface area, or pore size distributions as measured by nitrogen adsorption. This suggests that the increase in density is mainly achieved by reducing the volume of macropores that exist between grain boundaries. In addition, this similarity between the apparent density and compressed bulk density for both samples suggests that neither has a significant amount of micropore volume or surface area which is being missed by nitrogen adsorption.

Scanning electron microscopy (SEM) and transmission electron microscopy (TEM) images give a real space picture of the samples at the micro and nano scale respectively. Figure 5.3 shows SEM images for 3K and HS;0B before and after the application of a small amount of mechanical pressure applied by hand. On the microscale, 3K is composed of grains of a wide variety of sizes, again likely representing its biological origins. HS;0B has much more regularly sized grains, especially after the application of mechanical pressure. Before the application of mechanical pressure, the sample has a flaky appearance, and evidence of the gas bubbles formed during the pyrolysis process can be clearly seen. In addition, white spots are seen on the outside of some of the flakes. EDS analysis shows that these spots contain significant amounts of chlorine and iron, suggesting that this is the white film which is observed on outgassing. The TEM image taken after the application of mechanical pressure

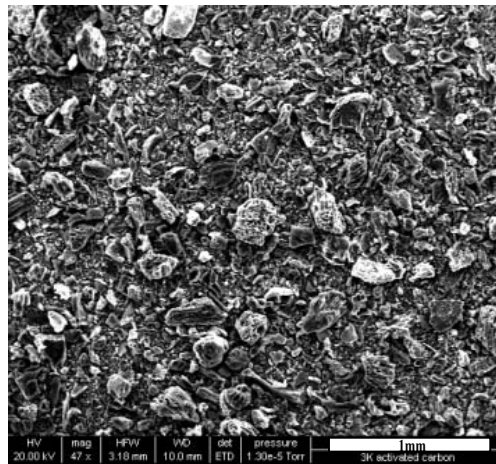
shows large areas that are lighter in color than the rest of the image. These are likely regions of charge accumulation [102], reflecting the observed electrostatic nature of the bulk sample. SEM images of another PVDC sample from the literature [88] look quite different than HS;0B, containing large grains that look very much like a hunk of burnt plastic. This sample was been heated to a higher temperature and the heat was applied more quickly.



(a) HS;0B



(b) HS;0B, mechanical pressure



(c) 3K

Figure 5.3: SEM images.

Figure 5.4 shows TEM images for both samples. Again, the samples are quite different. Despite its relatively heterogeneous pore size distribution, the TEM images

of 3K appear quite homogeneous, both within a single image and between different views (not shown). Randomly oriented irregularly shaped pores can be seen with widths on the order of 10 Å with lengths of several nanometers. On the other hand, the TEM images of HS;0B are quite heterogeneous with a wide variety of structures seen over different images, thus several views are shown. An image of a single flake (Figure 5.4(a)) shows that it is quite thin and contains a variety of structures. Structures which appear to be curved and tube shaped can be seen in Figure 5.4(b) The bulk of the image shows pores with widths on the order of 50 Å and lengths of tens of nanometers with dark regions within them which suggest they may be partially blocked. At the top of the image, pores with widths on the order of 10 Å and lengths of tens of nanometers can be seen. These smaller structures are much more faint. These two sizes of structures may correspond to the two peaks in the pore size distribution of this sample. Figure 5.4(b) shows an image which contains some of the larger tube like structures embedded in a region in which any pores present are difficult to distinguish from the background. The actual structure of these pores may be similar to the small faint pores in Figure 5.4(b) and simply be out of focus, or they may have some completely different structure. However, given the pore size distribution, it is clear that these areas which are out of focus contain many of the smallest pores.

While the TEM images of HS;0B are not of high enough quality that all of the pores can be visualized, it seems that at least some of the pores are long, contiguous, and tube shaped with randomly curved orientations. It is simple to see how this pore structure could arise as a result of the polymeric structure of the precursor and the manufacturing method. Because the sample is initially heated at a low rate and outgassing proceeds slowly while the polymer melts, one might imagine that long adjacent polymer strands in the melt which are slowly losing H and Cl atoms at random locations along their length end up cross-linking at points which are not

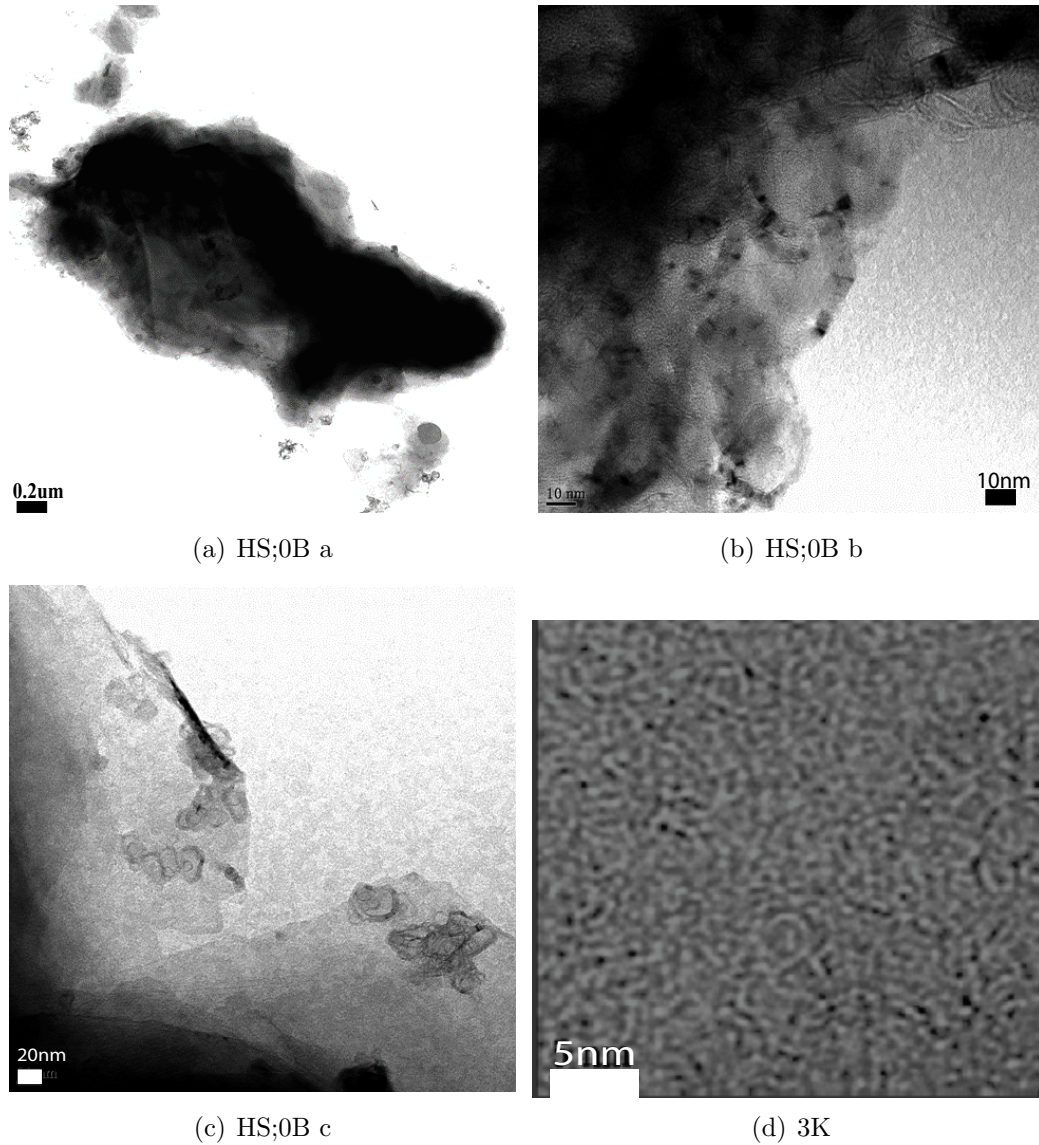


Figure 5.4: TEM images.

exactly colinear, creating curvature in the same way a bi-metallic strip curves due to the slightly different lengths of the two sections at a given temperature. This would leave some carbon atoms out of the cross-linking, causing the sample to be prone to the accumulation of electrostatic charge. Conversely, if heat were to be applied more quickly, the sample would not spend much time in the melted stage, giving the polymer strands little time to rearrange themselves relative to one another before the violent outgassing causes the sample to carbonize and harden.

## 5.4 Thermodynamic Characterization

### 5.4.1 Hydrogen Adsorption

Hydrogen (99.999% purity) adsorption isotherms were measured volumetrically at the University of Missouri using an HTP-1 Volumetric sorption analyzer (Hiden Isochema Ltd). Hydrogen measurements were performed at temperatures of 80, 90, and 303 K and at pressures ranging from 1 to 100 bar. Dry sample mass was determined by measuring the sample mass after outgassing at 400 °C for two hours under vacuum ( $\sim 20$  torr).

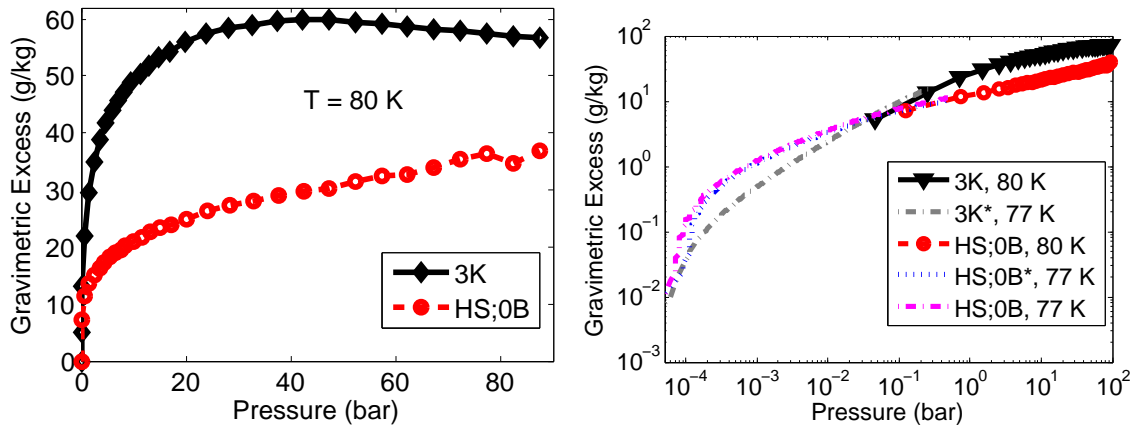


Figure 5.5: Excess hydrogen adsorption isotherms taken at 80 K (left). Shown on a log-log scale with low pressure isotherms taken at 77 K (right). \*Outgassing done at 150 °C.

Low pressure hydrogen adsorption isotherms were measured at the Laboratoire Chimie Provence at 77 K using a quasi-equilibrium procedure in which the gas is streamed into the sample cell at a constant rate  $f$ , which is on the order of  $\mu$ -moles per minute. The pressure  $P(t)$  is measured as a function of time  $t$ , and the amount adsorbed  $n_a$  in moles is calculated as,

$$n_a = ft - P(t)\left(\frac{V_r}{RT_r} + \frac{V_s}{RT_s}\right) \quad (5.2)$$

where  $V_s$  is the volume of the sample cell which is at a temperature of  $T_s = 77$  K and is measured by helium pycnometry, and  $V_r$  is the volume of the gas handling system which is at room temperature  $V_r = 295$  K and is measured by hydrogen pycnometry. Samples were outgassed at 150 or 400 °C for 12 hours under vacuum ( $\sim 20$  torr) and the dry sample mass after outgassing was estimated from the initial sample mass using typical mass loss values.

Room temperature gravimetric excess isotherms were shown in Figure 5.1. The room temperature isotherm for HS;0B is slightly larger than that of 3K, despite having nearly a quarter of the surface area. Cryogenic excess isotherms are shown in Figure 5.5, with low and high pressure hydrogen adsorption isotherms shown on a log-log scale in Figure 5.5(b). The isotherms for the two samples are quite different. The cryogenic excess isotherm for 3K has a peak at about 40 bar, a feature which is normally seen at cryogenic temperatures as the gas density begins to grow faster than the density of the adsorption layer. However, the isotherm for HS;0B is missing this typical feature. Because the excess amount adsorbed continues to grow, the adsorption at pressures above 90 bar is nearly double what would be expected from “Chahine’s rule” [58], which predicts a maximum of about 10 g/kg per 500 m<sup>2</sup>/g.

For both samples, the low pressure isotherms, which were taken at 77 K, are about 10% larger than the high pressure isotherms, which were taken at 80 K, a difference which is consistent with the temperature difference. Up to 0.1 bar, the isotherms for HS;0B have a larger slope than that of 3K, despite having the smaller surface area. In addition the isotherm for HS;0B which was prepared by outgassing at 400 °C is about 10% larger than the isotherm for HS;0B which was prepared by outgassing at 150 °C, suggesting the presence of the white film has a negative effect on the adsorption.

Absolute adsorption isotherms were calculated from excess isotherms using the methods of Chapter 2 [15] and divided by the specific surface area of each sample to give the areal absolute adsorption, shown in Figure 5.6. At both temperatures,

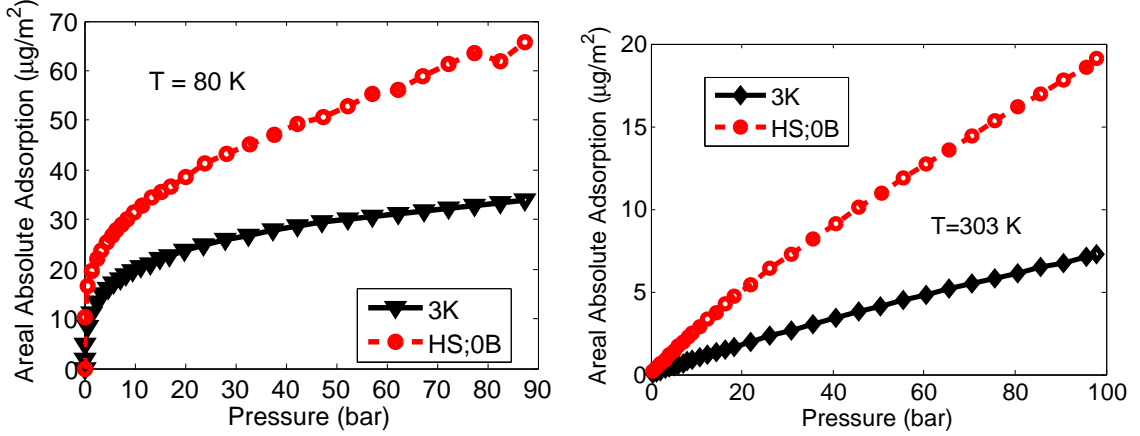


Figure 5.6: Areal absolute hydrogen adsorption isotherms taken at 80 K (left) and 303 K (right).

the areal adsorption is 2–3 times higher for HS;0B than for 3K. Using the absolute adsorption at 80 K and  $\sim 90$  bar, at which the film is typically near saturation, we can calculate the surface area per molecule and density of the adsorbed film. Assuming a hexagonal close packing structure, the average distance between hydrogen molecules in the film  $d$  can also be calculated. These values are given in Table 5.2.

Table 5.2: Surface area per molecule  $\alpha$  and density of the adsorbed film  $\rho_f$  at 80 K and  $\sim 90$  bar.

sample	$\alpha$ ( $\text{\AA}^2$ )	$d$ ( $\text{\AA}$ )	$\rho_f$ (g/L)
3K	9.77	3.35	67
HS;0B	5.04	2.41	136

For sample 3K, the average distance between hydrogen molecules is nearly equal to the position of the minima of a Lennard-Jones  $\text{H}_2\text{-H}_2$  potential [42]. Likewise, the film density is nearly equal to the density of liquid hydrogen,  $70.6\text{g/L}$  [5], suggesting the film is indeed near saturation. However, for HS;0B the average distance between hydrogen molecules is well into the repulsive regime of a Lennard Jones  $\text{H}_2\text{-H}_2$  potential and the film density is twice that of liquid hydrogen.

## 5.4.2 Isosteric Heat

The isosteric heats of adsorption were calculated with the Clausius Clapeyron equation and isotherms at 80 and 90 K by utilizing a set of best practices which we described in Chapter 2 [15] and are shown in Figure 5.7(a). The results for 3K are quite reasonable, ranging from about 6 kJ/mol at low coverage to 3 kJ/mol at high coverage, similar to what has been theoretically predicted for flat carbon pores [62] and experimentally found for graphene and MSC-30 [44, 45]. The results were quite different for HS;0B. While the larger value for the isosteric heat of 7.2 kJ/mol at low coverage is consistent [42] with the many small pores seen in the pore size distribution (Figure 5.2); the value of 1.6 kJ/mol at high coverage is significantly lower than would be expected for any type of pores composed of carbon [62, 63] and, since most of the sites seem to have isosteric heats significantly less than those of activated carbons, does not explain the excellent cryogenic excess adsorption.

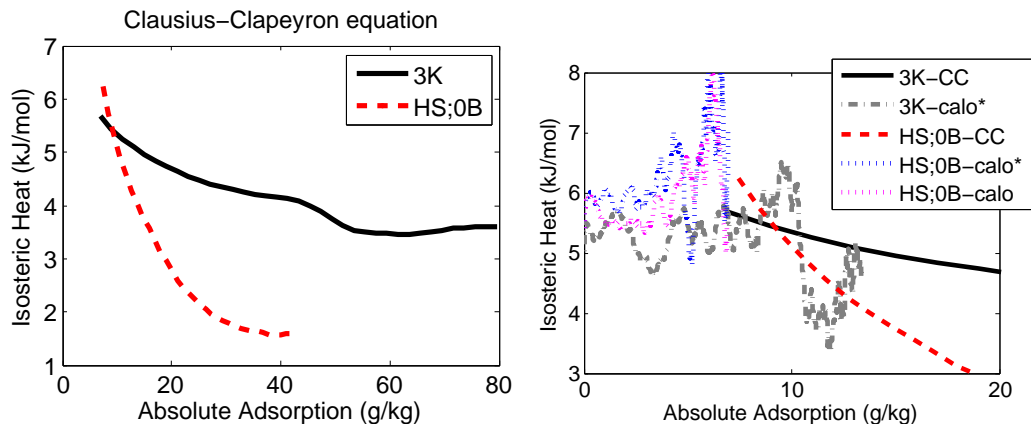


Figure 5.7: Isosteric heats of adsorption calculated from isotherms (left) and compared with calorimetry measurements (right). \*Outgassing done at 150 °C.

In addition, the isosteric heat was measured directly by calorimetry [104] at Laboratoire Chimie Provence at 77 K using the same quasi-equilibrium procedure described in the previous section. The heat flux  $\phi$  was measured as a function of time and used

to calculate the isosteric heat,

$$\Delta h = \frac{dt}{dn_a}(\phi(t) + \frac{dP(t)}{dt}V_c), \quad (5.3)$$

where  $V_c$  is the volume of the sample cell in contact with the calorimeter. Because the heat flux, which is on the order of microwatts and quite noisy to begin with, is divided by the differential amount adsorbed, the noise of the resultant signal is only reasonable in the very low pressure region where the differential amount adsorbed is comparably large. These low coverage isosteric heats are shown in Figure 5.7(b) along with the results of the Clausius-Clapeyron equation. While noisy, the results for 3K obtained via the two different methods are quite comparable to one another. Not only do the absolute values of the low coverage isosteric heat agree well, but both tend to drop off as a function of coverage. On the other hand for HS;0B, while the absolute values agree reasonably well, the slopes are quite different for the two methods. The isosteric heat as calculated by the Clausius-Clapeyron equation drops off quickly, whereas the isosteric heat as measured by calorimetry actually appears to rise as a function of coverage for both outgassing temperatures. While the noisiness of the calorimetry signal makes definite conclusions difficult, it is clear that the coverage dependent behavior of the isosteric heat as measured by the two different methods is quite different.

## 5.5 Discussion

While the results reported in this paper are quite unusual, they are not unprecedented. Quinn [101] has previously published data on a similar PVDC sample whose room temperature excess adsorption at 30 bar is as large as ours. This sample also has a cryogenic excess adsorption up to 13 bar which is unusually large for its surface area,

although it appears to be leveling off and thus would likely show a peak if higher pressure data were taken. However, other samples of various types can be found in the literature [38, 39, 64] which share HS;0B's lack of a peak in the excess and unusually high adsorption at cryogenic temperatures, and are likewise coupled with an unusually low isosteric heat as determined by the Clausius-Clapeyron equation. As such, it appears that there may be samples which are significantly affected by phenomena which are not well described by classical adsorption theory.

The simplest explanation for the unusually high room temperature excess adsorption of HS;0B is simply that this sample does contain many of the narrow pores in which the binding energy is significantly larger, and indeed is large enough to overcome the significantly smaller surface area. This explanation is certainly consistent with the pore size distribution 5.2, but the nitrogen adsorption analysis techniques are not accurate enough to tell us whether or not this assertion is certainly true. Assuming that at room temperature we are in the Henry's law regime in which adsorption is linearly proportional to surface area and proportional to the exponential of the binding energy, if 3K has a binding energy of about 5 kJ/mol [53], the binding energy of sample HS;0B should be about 7.7 kJ/mol, an increase of over 50%. However, if this were indeed the explanation, we would expect the absolute value of the isosteric heat as measured by calorimetry for sample HS;0B to be increased by a similar amount, but instead it is increased by only about 15% at low coverage. In addition, this hypothesis does not at all explain the cryogenic adsorption or Clausius-Clapeyron isosteric heat, and is not supported by the analysis presented in Chapter 4 in which neutron scattering data is shown to not demonstrate the effects of a significant number of these small pores.

Another possible explanation is that the surface area and nanopore volume of HS;0B increases significantly as a function of pressure through some unknown physical mechanism. To investigate this possibility, theoretical absolute isotherms were

calculated at 80 and 90 K as in Chapter 2 using the localized Langmuir adsorption model [54], which treats the adsorbed layer as consisting of independent adsorption sites of fixed size with a binding energy of  $E_b = 5$  kJ/mole [53]. Adjacent molecules are assumed to not interact with one another. The motion parallel and perpendicular to the plane is assumed to be that of a harmonic oscillator, with vibrational frequencies  $\nu = 3 \times 10^{12}$  Hz. Excess isotherms were calculated from the absolute isotherms using a volume of the adsorbed film equal to  $V_a = \Sigma l$  where  $l = 4$  Å and  $\Sigma = 2630$  m<sup>2</sup>/g. Figure 5.8 shows excess isotherms at 80 K and isosteric heats calculated using the Clausius-Clapeyron equation for the case in which the number of adsorption sites is constant, and the case in which the number of adsorption sites increases linearly by a factor of 2 over the 100 bar pressure range.

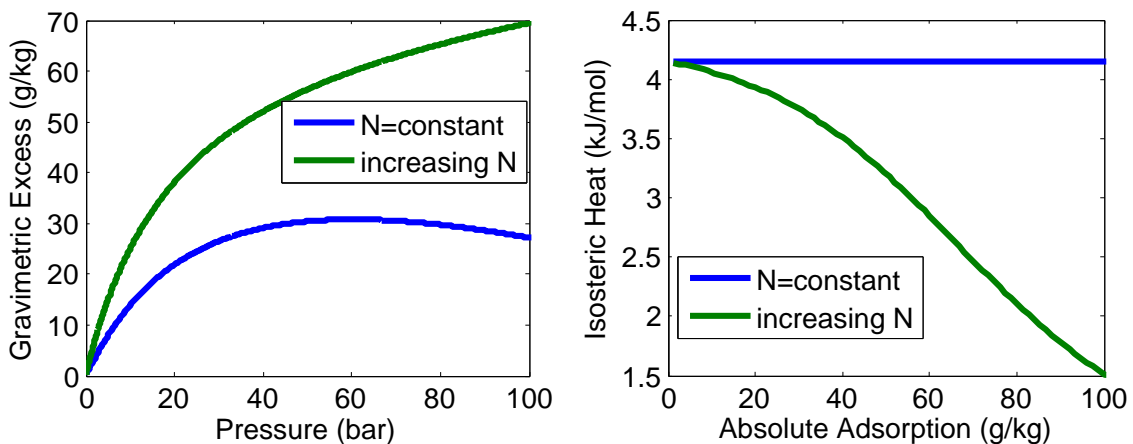


Figure 5.8: Gravimetric excess adsorption (left) and isosteric heat (right) for theoretical isotherms in which the number of adsorption sites is either fixed or variable.

When the number of adsorption sites is constant, the cryogenic excess adsorption has a peak and the isosteric heat of adsorption is flat, as it should be for an idealized isotherm. When the number of adsorption sites increases as a function of pressure, the cryogenic excess adsorption does not have a peak and appears to be overly large for its surface area, and the isosteric heat drops off to a low value at high pressure. However, a number of significant problems with this hypothesis remain. Firstly, to

get results which match our experimental data reasonably well, we must imagine some physical mechanism by which the surface area increases by a factor of two as the pressure increases. This mechanism might open up pores which are initially just barely too small for hydrogen to enter, but if there were significant numbers of these pores, their presence should have been revealed by a significant difference between the apparent density and the compressed bulk density and we showed in Table 5.1 that this is not the case. Otherwise, we must imagine some mechanism by which the application of the pressure of the adsorbed hydrogen molecules simply increases the surface area by the factor of two, and given the strength of carbon-carbon bonds this is difficult to imagine, as bonds would have to be stretched by 40% on average. In addition, this hypothesis does not explain the room temperature adsorption. Not only is this increase in surface area not large enough to explain the absolute value of the room temperature adsorption, it would also significantly affect the slope of this isotherm as well, an effect which is not seen.

A third hypothesis has to do with the fact that the hydrogen molecule is a boson, and as such a state may be occupied by more than one molecule. The thermal wavelength, which gives the average distance between molecules at which quantum statistics begin to significantly affect the results, is equal to  $\lambda_r = 0.7 \text{ \AA}$  at room temperature and  $\lambda_c = 1.4 \text{ \AA}$  at 77 K, distances at which the H<sub>2</sub>-H<sub>2</sub> potential is highly repulsive. The repulsive part of this Van der Waals potential is caused by the fact that electrons are fermions, and at these distances the electron clouds of the adjacent molecule significantly overlap, forcing electrons to higher energy states and increasing the interaction energy. Thus under normal circumstances, the fact that electrons are fermions prevents the hydrogen molecules from getting close enough that the bosonic nature of the composite particle can affect the adsorption statistics.

The thermal wavelength is derived by counting the density of quantized energy states accessible at a given temperature in a macroscopically sized box. However, we

certainly do not have macroscopically sized pores, thus it is possible that the structure of the pores could significantly reduce the density of states. The density of states in the adsorption plane is given by  $1/\alpha l$  where  $\alpha$  is the surface area per adsorption site and  $l$  is the width of the adsorbed film. By increasing  $\alpha$ , thus not allowing adjacent hydrogen molecules to get as close to one another, it could be possible for boson statistics to begin resulting in multiple occupation of states before the potential between molecules becomes highly repulsive. This explanation is consistent with the results of Chapter 4, which showed that HS;0B has more states which diffuse along the plane and that these states are at a lower energy, thus are more likely to be occupied. However, it would have to be determined how this could also reduce the Debye-Waller factor for this to be a complete hypothesis.

# Chapter 6

## Summary and concluding remarks

The first part of this work has primarily addressed theoretical and practical aspects of sample characterization techniques which have traditionally been less reliable due to their complex nature, the isosteric heat of adsorption as calculated by comparing nearby adsorption isotherms in Chapter 2 and inelastic neutron scattering (INS) from adsorbed hydrogen atoms in Chapter 3. In Chapter 4, theoretical lessons from Chapter 3 were applied to real experimental data, and the recoil states were found to be not only an important part of the spectra, but integral in separating different types of transitions. One sample, HS;0B, was found to have significantly different recoiling states suggesting that the diffusive motion of molecules adsorbed in this sample is quite different. It was hypothesized that this behavior could be related to structural properties of the pores in this material, perhaps reflecting the presence of long contiguous pores which are curved along their length.

In Chapter 5 this unusual sample was discussed more in depth, with structural data obtained through nitrogen adsorption and transmission electron microscopy supporting the presence of these types of pores. In addition, the basis of this unusual structure in the details of the manufacturing process was explored. Thermodynamic

characterization of the sample was presented. The sample shows unusually high adsorption, at both cryogenic and room temperatures. In fact, the high pressure cryogenic adsorption appears to be impossibly high, with the film at nearly twice the liquid density of molecular hydrogen. Isothermic heats were presented, both calculated from comparing two isotherms as discussed in Chapter 2 and experimentally determined through calorimetry. The results of the two methods were found to be at odds with one another, in stark comparison to other samples whose isothermic heats obtained through different methods are quite consistent.

Several hypotheses that account for aspects of this unusual data set were presented. Firstly, the sample may contain many very small pores with high binding energy, accounting for the high room temperature adsorption. However, this does not explain the high cryogenic adsorption and is not consistent with the neutron scattering data or isothermic heats. Secondly, there may be some physical mechanism by which the surface area and thus number of adsorption sites increases significantly as a function of pressure, which would explain the calculated isothermic heat and the cryogenic adsorption. However, this does not explain the room temperature adsorption and in addition, the physical mechanism by which this happens to such a significant amount in this sample, but not in others is difficult to imagine.

Finally, the unusual results are hypothesized to arise from the bosonic nature of molecular hydrogen, which allows for the multiple occupation of states. This explanation seems initially quite fantastic and improbable, and I certainly would not propose it out of the blue as a solution to the hydrogen storage problem. However, none of the other explanations seem to have the ability to consistently explain the majority of the data and as Sherlock Holmes would say, "Once you eliminate the impossible, whatever remains, no matter how improbable, must be the truth." Certainly we are not at this stage of certainty yet. But in my opinion, the mere possibility makes continued research along this line worthy of attention, not only for the pure mental

pleasure which it is sure to continue to provide, but because it also offers an exciting possibility of even greater improvements in performance which could be utilized by further modifications of the structure of these types of samples.

Of course at this stage where no details of the theory have been offered, we simply do not know for sure if it can consistently explain the data either, so clearly a great deal of work remains to be done. In what follows, I will outline qualitative aspects which a final theory must have. Then future work, both theoretical and experimental will be discussed.

Detailed examination of the adsorption data, both on this particular sample and on other similar samples, seems to suggest that there are in fact two phenomena, which are likely linked, that need to be explained. The first aspect is the impossibly large high pressure cryogenic adsorption, coupled with the lack of peak in the excess and unusually low calculated isosteric heat. As we noted in Chapter 2, this trio of features has been seen in other samples [38, 39, 64]. However, these samples do not have cryogenic isotherms which rise with such a large slope, nor do they have room temperature adsorption which is unusually high for its surface area (where reported). Conversely, as noted in Chapter 5 there is another PVDC sample in the literature [101] which has room temperature adsorption which matches our sample and cryogenic adsorption which rises with a very large slope, but that levels off quickly and, though the isotherm does not go to high enough pressure to be sure, it looks as though it is near reaching a peak at a pressure of only 13 bar.

The high large pressure cryogenic adsorption, where film densities are reaching values nearly twice as large as the liquid density, and where adsorption continues to grow beyond values where the film would normally be saturated, seems impossible to explain without there being multiple occupation of states due to the bosonic nature of molecular hydrogen. As discussed in Chapter 5, this would not be observed under normal circumstances because the thermal wavelength, which gives the average

distance between molecules at which quantum statistics becomes important, equal to  $\lambda_r = 0.7 \text{ \AA}$  at room temperature and  $\lambda_c = 1.4 \text{ \AA}$  at 77 K, is much smaller than the distance at which the  $\text{H}_2\text{-H}_2$  potential becomes highly repulsive,  $\sigma = 3 \text{ \AA}$ . This repulsive part of the potential is caused by overlap of the electron clouds of the two adjacent molecules, which forces the electrons to higher energy states so as to avoid one another. Thus under normal circumstances, the fact that electrons are fermions prevents the hydrogen molecules from getting close enough that the bosonic nature of the composite particle can affect the adsorption statistics.

Our goal, then, is to increase  $\lambda$  by decreasing the density of states. Certainly we know that to decrease the number of states, we simply confine the molecule in a narrow potential. However, while this decreases the overall number of states, it also tends to decrease the volume by the same factor, leaving the density of states roughly unchanged. In addition, since we need to be able to get the molecules into the pore, we must choose a pore shape with at least one extended dimension, in which the states will be very close together. This situation is depicted in the left of Figure 6.1, in which the pore is a cylinder, with the  $z$  direction going along the length. We might imagine decreasing the number of states in the extended direction by curving the pore around, as in the torus shaped pore depicted in the center of Figure 6.1. Now when deep in the pore, the molecule is confined in all directions, which would seem to decrease the number of states without an attendant decrease in the volume. But if we choose a relatively ordered configuration, such as the torus, we know that the problem is now more simply solved in some alternative coordinate system, and the states will simply be close together in the  $\theta$  dimension rather than the  $z$  dimension. However, if we choose a pore configuration where the pore is curved around in random directions, as the pore in the right of Figure 6.1, the molecule is still heavily confined when deep in the pore, but there is no alternative coordinate system in which the states remain close together in one dimension. We can hypothesize that in pores of

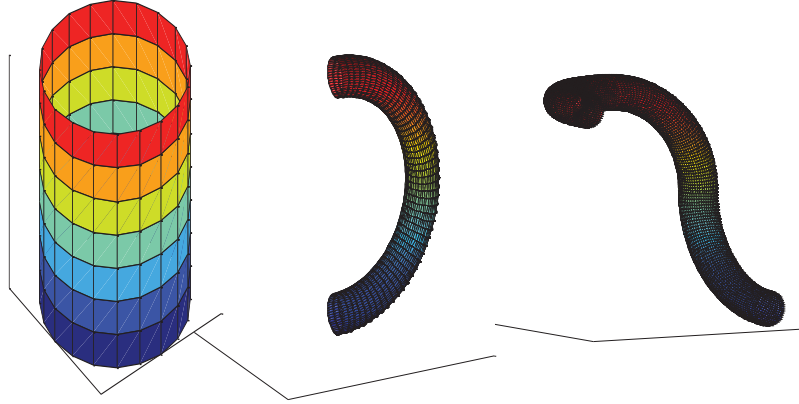


Figure 6.1: Representative pore shapes.

this type, which are long and contiguous with random curvature occurring along their length, the density of states will be decreased. These are exactly the types of pores for which we have shown evidence of their existence in HS;0B.

There is another significant problem with this scheme which occurs to one upon initial consideration. Let us consider a simple isotherm, such as the Langmuir model, which is derived by considering a single adsorption site which does not interact with its neighbors. Using the grand canonical ensemble and Fermi statistics, the partition function for an unoccupied state is 1 and the partition function for an occupied state is  $\chi P$ , thus the coverage or fraction of sites filled is simply,

$$\theta = \frac{\chi P}{1 + \chi P}. \quad (6.1)$$

$\chi$  is known as the Langmuir constant and is proportional to factors such as the exponential of the binding energy. To get the total number of adsorbed molecules, we must then multiply the coverage by  $N$ , the number of adsorption sites. So far so good, but if we now attempt to allow for multiple occupation of states by reducing the overall density of states, thus not allowing molecules in adjacent adsorption sites to get close enough to one another for the interaction potential to become repulsive, we likewise increase the surface area per adsorption site  $\alpha$  with an attendant reduction

in  $N$ , the number of adsorption sites. For example, if we halve the density of states, the surface area per adsorption site increases by a factor of 4 and the number of adsorption sites is reduced by the same factor of 4. Because the total adsorption is equal to  $N\theta$ , we must likewise quadruple  $\theta$  by the same factor of 4 to even match our previous adsorption, let alone increase it. This proposition seems like a ridiculous way to attain our goal, like walking down into the valley when faced with an unscalable peak simply because we can see the top more clearly from there.

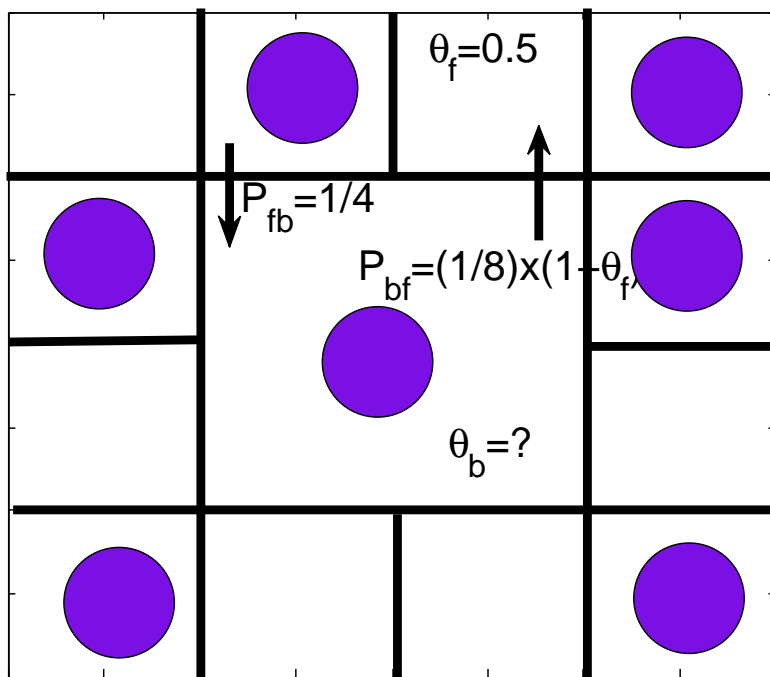


Figure 6.2: A model of an adsorption surface, where all sites have the same binding energy but are not the same size. The larger site is large enough that molecules inside it do not overlap with their neighbors enough for Fermi statistics to apply. The principle of detailed balance can be used to calculate the occupation of this site.

However, on further consideration this problem can be overcome if we consider the adsorbate system not by itself, but as in contact with the molecules in the gas phase. Figure 6.2 shows a surface with a number of adsorption sites, which all have the same binding energy. The smaller sites are of the normal size, and we assume that these sites are at the coverage  $\theta_f$ . There is also an adsorption site that is twice

as wide and tall as its neighbors, and we assume that it is so big that hydrogen molecules contained in this site do not overlap with their neighbors enough for Fermi statistics to apply, thus the average occupation of this site  $\theta_b$  can be greater than 1. The principle of detailed balance says that  $\theta_f P_{fb} = \theta_b P_{bf}$ , where  $P_{ij}$  gives the probability of a hydrogen molecule from jumping from site  $i$  to site  $j$  and is equal to the probability of choosing a particular neighbor from all of its neighbors times the probability of that move being accepted. The larger site has eight neighbors, and a molecule can only jump to the neighbor chosen if it is not already occupied, making  $P_{bf} = (1 - \theta_f)/8$ . Each of the smaller sites has four neighbors, one of which is the larger site, and these moves are always accepted since the larger site can be multiply occupied, making  $P_{fb} = 1/4$ . Thus we can calculate the occupation of the large site as,

$$\theta_b = \frac{2\theta_f}{1 - \theta_f} = 2\chi P. \quad (6.2)$$

This isotherm actually turns out to have a linear dependence on pressure, due to the fact that high occupation does not prevent more molecules from being added.

Figure 6.3(a) shows some model isotherms, calculated at a temperature of 80 K. One is a typical Langmuir isotherm, calculated using Eq. 6.1, where the entire surface is assumed to be covered with sites of normal size. For the second,  $5/9^{ths}$  of the surface is covered with 5 sites of normal size whose occupation is also given as Eq. 2.12, and  $4/9^{ths}$  of the surface is covered with 1 of the larger sites whose occupation is given as Eq. 6.2. One can see that at low pressures, the isotherm with some large adsorption sites does not perform as well as the typical langmuir isotherm, due to the fact that there are less adsorption sites. However, at high pressure, the multiple occupation of the large sites is large enough to overcome the overall reduction in the number of sites.

The theoretical isotherms can be compared with the experimental isotherms,

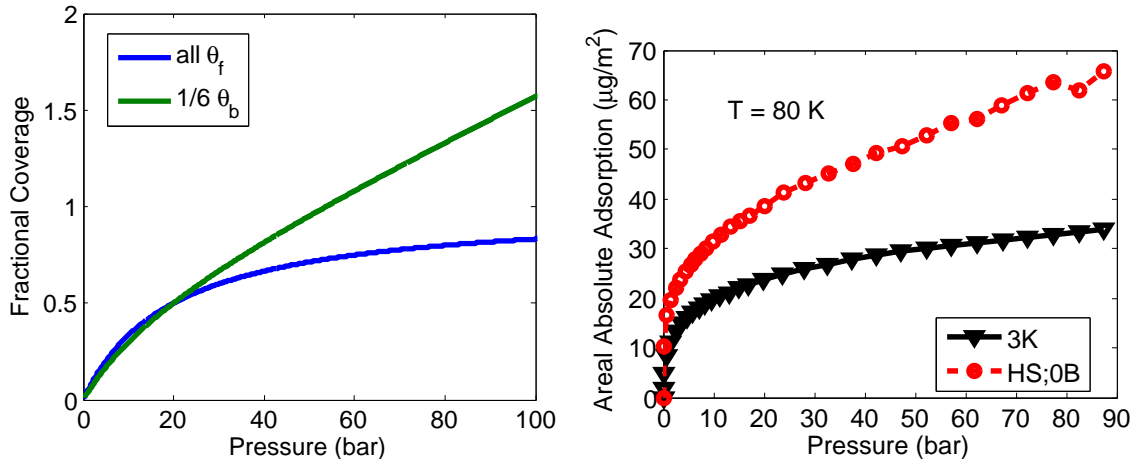


Figure 6.3: (Left) Theoretical isotherms which do or do not allow multiple occupation of some sites. (Right) Areal absolute adsorption isotherms calculated from experimental data as in Chapter 2.

shown in Figure 6.3(b). At high pressure, both experimental isotherms are comparable to the theoretical isotherms, with the results for HS;0B fitting better with the new type of isotherm discussed above. However, neither experimental isotherm is well described by these theoretical isotherms at low pressure. The fact that the experimental isotherms seem to have a very large initial slope has been noted in many other types of isotherms, and makes simple theoretical analysis of these isotherms difficult. This is why we used a Langmuir-Freundlich isotherm along with a moving window in Section 2.4.2 to fit. Generally, this is assumed to be due to sample heterogeneity, as sites with a higher binding energy tend to fill exponentially faster. These pores with higher binding energy are the same ones that we show in Chapter 3 should have significantly different neutron scattering spectra. However, the experimental results shown in Chapter 4 did not show large amounts of these small pores, thus mere sample heterogeneity does not seem to be an adequate explanation, for either the more typical sample 3K, or HS;0B.

Model isotherms use many simplifying assumptions, the most significant of which is ignoring the interactions. The Langmuir constant  $\chi$  can be calculated based on

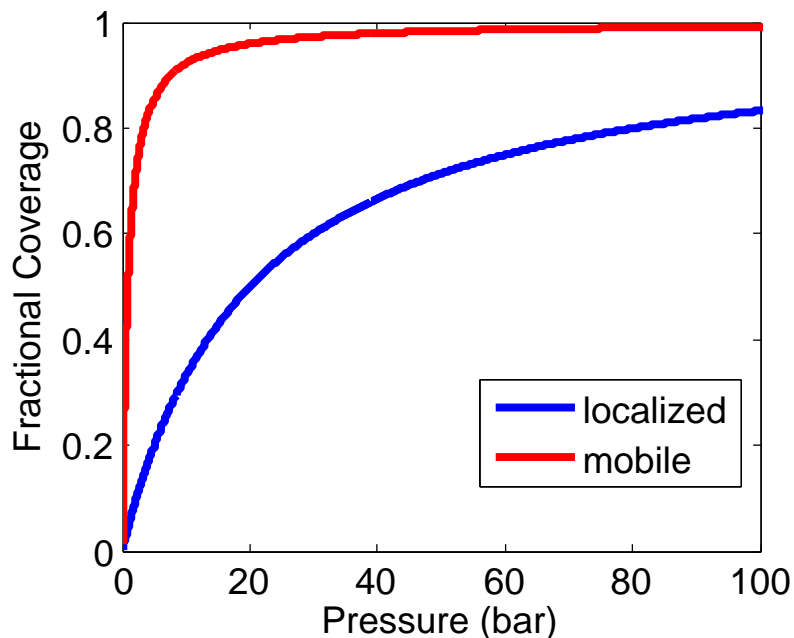


Figure 6.4: Langmuir isotherm at 80 K in which a localized or mobile model is used.

either a localized model, in which adsorption happens at individual sites which do not interact with one another, or a mobile model, in which adsorbed molecules diffuse along the plane. Typical isotherms are shown in Figure 6.4, where parameters have been estimated as in Section 2. The corrugation of a graphene adsorption surface, which is assumed to be a good model for small regions in activated carbon, is 50 Kelvin. Thus the adsorption potential itself is not large enough to localize the molecules. Instead, it is the interactions between the molecules that define the localized adsorption sites. Thus it is reasonable to assume that the size of the adsorption sites  $\alpha$  change as a function of coverage. At low enough coverages that interactions become relatively unimportant, it is likely that adsorption is mobile, accounting for the steep low-coverage slope of the isotherms. For mobile adsorption,  $\chi$  itself is linearly dependent on  $\alpha$ . Thus, if the diffusive behavior of molecules adsorbed in HS;0B is significantly different, as suggested by the results of Chapter 4, we would also expect the low-coverage and high-temperature behavior of this sample to be higher, though for slightly different reasons than the high-coverage adsorption.

It is clear that significant work remains to understand the theoretical basis of HS;0B's high adsorption. A proposal has been submitted for neutron scattering work that will explore the temperature dependence of the spectra. In addition, spectra will be collected from variants of HS;0B, including a sample which has been outgassed at 400 °C, rather than 125 °C as was done for the work presented in Chapter 4. Another variant was created by applying the heat much faster during the manufacturing process, which we hypothesized in Chapter 5 does not give as much time for the PVDC to melt and form the long curved pores that seem to be present in HS;0B. It is also important that we explore the exact nature of the free recoil states of adsorbed systems, and whether the effective mass is significantly different from that of a free hydrogen molecule due to interference between different discrete states, or if the change is due to the low energy of the colliding neutrons. To explore this, it will be important to collect spectra both from free liquid hydrogen under the same conditions, as well as from hydrogen adsorbed on surfaces that can be oriented relative to the scattering angle. Based on the experimental spectra, there is also significant work that can be done to improve the theoretical treatment presented in Chapter 3. Finally, hydrogen adsorption isotherms and other characterization techniques need to be applied to variants of HS;0B, so that spectral work can be correlated with adsorption data.

# Bibliography

- [1] Alison Fleig Frank. *Oil Empire: Visions of Prosperity in Austrian Galicia*. Harvard University Press, 2005.
- [2] Alfred J. Cavallo. Hubbert's petroleum production model: An evaluation and implications for world oil production forecasts. *Natural Resources Research*, 13:211–221, 2004.
- [3] Grant W. Petty. *A First Course in Atmospheric Radiation*. Sundog Publishing, 2006.
- [4] Sunita Satyapai, John Petrovic, Carole Read, George Thomas, and Grace Ordaz. The U.S. department of energy's national hydrogen storage project: Progress towards meeting hydrogen-powered vehicle requirements. *Catalysis Today*, 120:246–256, 2007.
- [5] David R. Lide. *CRC Handbook of Chemistry and Physics*. CRC PRes, 1993.
- [6] John W. Sheffield. Show me the road to hydrogen. [http://utc.mst.edu/documents/R204\\_CR.pdf](http://utc.mst.edu/documents/R204_CR.pdf).
- [7] U.S. department of energy hydrogen program. <http://www.hydrogen.energy.gov/storage.html>.

- [8] Alliance for collaborative research in alternative fuel technology. <http://all-craft.missouri.edu>.
- [9] J. Burrell, M. Kraus, M. Beckner, R. Cepel, G. Suppes, C. Wexler, and P. Pfeifer. Hydrogen storage in engineered carbon nanospaces. *Nanotechnology*, 20:204026, 2009.
- [10] Session h20: Focus session: Physics of energy storage materials iii – hydrogen storage adsorbents. <http://meetings.aps.org/Meeting/MAR11/sessionindex2/?SessionEventID=149739>.
- [11] F. Rouquerol, J. Rouquerol, and K. Singh. *Adsorption by Powders and Porous Solids: Principles, Methodology, and Applications*. Academic Press, 1999.
- [12] Christian Lastoskie, Keith E. Gubbins, and Nicholas Quirke. Pore size distribution analysis of microporous carbons: a density functional theory approach. *J. Phys. Chem.*, 97:4786–4796, 1993.
- [13] Alexander V. Neimark, Yangzheng Lin, Peter I. Ravikovitch, and Matthias Thommes. Quenched solid density functional theory and pore size analysis of micro-mesoporous carbons. *Carbon*, 47(7):1617–1628, 2009.
- [14] Peter I. Ravikovitch and Alexander V. Neimark. Pore size distribution analysis of microporous carbons: a density functional theory approach. *Langmuir*, 22(26):11171–11179, 2006.
- [15] Raina J. Olsen, Matthew Beckner, Jimmy Romanos, Peter Pfeifer, and Carlos Wexler. Best methods for determining the coverage-dependent isosteric heat of adsorption. *Langmuir*, under review, 2011.

- [16] Raina J. Olsen, Lucyna Firlej, Bogdan Kuchta, Haskell Taub, Peter Pfeifer, and Carlos Wexler. Sub-nanometer characterization of activated carbon by inelastic neutron scattering. *Carbon*, 49:1111, 2011.
- [17] Tun Lu, Evelyn M. Goldfield, and Stephen K. Gray. Quantum states of hydrogen and its isotopes confined in single-walled carbon nanotubes: Dependence on interaction potential and extreme two-dimensional confinement. *J. Phys. Chem.*, 110(4):1742–1751, 2006.
- [18] Taner Yildirim and A. B. Harris. Rotational and vibrational dynamics of interstitial molecular hydrogen. *Phys. Rev. B*, 66:214301, 2002.
- [19] Taner Yildirim and A. B. Harris. Quantum dynamics of a hydrogen molecule confined in a cylindrical potential. *Phys. Rev. B*, 67:245413, 2003.
- [20] Kerson Huang. *Statistical Mechanics*. John Wiley and Sons, Inc., 2000.
- [21] Shivaji Sircar. Excess properties and thermodynamics of multicomponent gas adsorption. *J. Chem. Soc., Faraday Trans. 1*, 81:1527–1540, 1985.
- [22] J. M. Simon, O. E. Haas, and S. Kjelstrup. Adsorption and desorption of H<sub>2</sub> on graphite by molecular dynamics simulations. *J. Phys. Chem C*, 114:10212–10220, 2010.
- [23] Yufeng He and Nigel A. Seaton. Monte carlo simulation and pore-size distribution analysis of the isosteric heat of adsorption of methane in activated carbon. *Langmuir*, 21:8297–8301, 2005.
- [24] Alan L. Myers, Jose A. Calles, and Guillermo Calleja. Comparison of molecular simulation of adsorption with experiment. *Adsorption*, 3:107–115, 1997.

- [25] Barbara Schmitz, Ivana Krkljus, Emi Leung, Hans Wolfgang Hoffken, Ulrich Mullter, and Michael Hirscher. A high heat of adsorption for hydrogen in magnesium formate. *ChemSusChem*, 3:758–761, 2010.
- [26] Shaheen A. Al-Muhtaseb. Adsorption and desorption equilibria of nitrogen, methane, ethane, and ethylene on date-pit activated carbon. *J. Chem. Eng. Data*, 55:313–319, 2010.
- [27] Byoung-Uk Choi, Dae-Ki Choi, Young-Whan Lee, and Byung-Kwon Lee. Adsorption equilibria of methane, ethane, ethylene, nitrogen, and hydrogen onto activated carbon. *J. Chem. Eng. Data*, 48:603–607, 2003.
- [28] Hansong Cheng, Xianwei Sha, Liang Chen, Alan C. Cooper, Maw-Lin Foo, Garret C. Lau, Wade H. Bailey, and Guido P. Pez. An enhanced hydrogen adsorption enthalpy for fluoride intercalated graphite compounds. *J. Am. Chem. Soc.*, 131:17732–17733, 2009.
- [29] Jing Li, Erdong Wu, Jiangwei Song, Fengshou Xiao, and Changjian Geng. Cryoadsorption of hydrogen on divalent cation-exchanged X-zeolites. *Int. J. of Hyd. Energy*, 34:5458–5465, 2009.
- [30] Xin Hu, Boris O. Skadtchenko, Michel Trudeau, and David M. Antonelli. Hydrogen storage in chemically reducible mesoporous and microporous Ti oxides. *J. Am. Chem. Soc.*, 128:11740–11741, 2006.
- [31] Tuan K. A. Hoang, Ahmad Hamaed, Michel Trudeau, and David M. Antonelli. Bis(benzene) and bis(cyclopentadienyl) V and Cr doped mesoporous silica with high enthalpies of hydrogen adsorption. *J. Phys. Chem. C*, 113:17240–17246, 2009.

- [32] Vinay V. Bhat, Cristian I. Contescu, Nidia C. Gallego, and Frederick S. Baker. Atypical hydrogen uptake on chemically-activated, ultramicroporous carbon. *Carbon*, 48:1331–1340, 2010.
- [33] Sang Soo Han, Seung-Hoon Choi, and William A. Goddard. Zeolitic imidazolate frameworks as H<sub>2</sub> adsorbents: Ab initio based grand canonical monte carlo simulation. *J. Phys. Chem. C*, 114:12039–12047, 2010.
- [34] M.-A. Richard, P. Bnard, and R. Chahine. Gas adsorption process in activated carbon over a wide temperature range above the critical point. part 2: conservation of mass and energy. *Adsorption*, 15:53–63, 2009.
- [35] Zhuxian Yang, Yongde Xia, and Robert Mokaya. Enhanced hydrogen storage capacity of high surface area zeolite-like carbon materials. *J. Am. Chem. Soc.*, 129:1673–1679, 2007.
- [36] Yongde Xia, Gavin S. Walker, David M. Grant, and Robert Mokaya. Hydrogen storage in high surface area carbons: Experimental demonstration of the effects of nitrogen doping. *J. Am. Chem. Soc.*, 131:16493–16499, 2009.
- [37] E. Poirier, R. Chahine, P. Benard, L. Lafi, G. Dorval-Douville, and P. A. Chandonia. Hydrogen adsorption measurements and modeling on metal-organic frameworks and single-walled carbon nanotubes. *Langmuir*, 22:8784–8789, 2006.
- [38] Dipendu Saha, Zuojun Wei, and Shuguang Deng. Equilibrium, kinetics, and enthalpy of hydrogen adsorption in MOF-177. *Int. J. of Hyd. Energy*, 33:7479–7488, 2008.
- [39] Dipendu Saha, Zuojun Wei, and Shuguang Deng. Hydrogen adsorption equilibrium and kinetics in metaliorganic framework (MOF-5) synthesized with DEF approach. *Separation and Purification Technology*, 64:280–287, 2009.

- [40] Yong Sun and Paul A. Webley. Preparation of activated carbons from corncob with large specific surface area by a variety of chemical activators and their application in gas storage. *Chemical Engineering Journal*, 162:883–892, 2010.
- [41] Grigoriy Aranovich and Marc Donohue. Determining surface areas from linear adsorption isotherms at supercritical conditions. *J. Colloid and Interface Science*, 194:392–397, 1997.
- [42] B. Kuchta, L. Firlej, P. Pfeifer, and C. Wexler. Numerical estimation of hydrogen storage limits in carbon based nanospaces. *Carbon*, 48:223–231, 2010.
- [43] Huanhua Pan, James A. Ritter, and Perla B. Balbuena. Examination of the approximations used in determining the isosteric heat of adsorption from the Clausius-Clapeyron equation. *Langmuir*, 14:6323–6327, 1998.
- [44] G. Srinivas, Yanwu Zhu, Richard Piner, Neal Skipper, Mark Ellerby, and Rod Ruoff. Synthesis of graphene-like nanosheets and their hydrogen adsorption capacity. *Carbon*, 48:630–635, 2010.
- [45] Yaping Zhou and Li Zhou. Experimental study on high-pressure adsorption of hydrogen on activated carbon. *Science in China*, 39(6):598–607, 1996.
- [46] Robert Sips. On the structure of a catalyst surface. *J. Chem. Phys.*, 16:490–495, 1948.
- [47] M. Nielsen and W. Ellenson. Adsorbed layers of  $D_2$ ,  $H_2$ ,  $O_2$  and  $^3He$  on graphite studied by neutron scattering. *Journal De Physique*, 38(C4):10–18, 1977.
- [48] J. W. Gibbs. *The Collected Works of J. W. Gibbs Volume 1*. Longmans and Green, New York, 1928.
- [49] Shivaji Sircar. Excess properties and column dynamics of multicomponent gas adsorption. *J. Chem. Soc., Faraday Trans. 1*, 81:1541–1545, 1985.

- [50] Diego P. Valenzuela and Alan L. Myers. *Adsorption Equilibrium Data Handbook*. Prentice Hall, 1989.
- [51] Anutosh Chakraborty, Bidyut Baran Saha, Kim Choon Ng, Shigeru Koyama, and Kandadai Srinivasan. Theoretical insight of physical adsorption for a single-component adsorbent + adsorbate system: I. thermodynamic property surfaces. *Langmuir*, 25:2204–2211, 2009.
- [52] A. Chakraborty, B. B. Saha, S. Koyama, and K. C. Ng. On the thermodynamic modeling of the isosteric heat of adsorption and comparison with experiments. *Appl. Phys. Lett.*, 89:171901, 2006.
- [53] L. Mattera, F. Rosatelli, C. Salvo, F. Tommasini, U. Valbusa, and G. Vidali. Selective adsorption of  $^1\text{H}_2$  and  $^2\text{H}_2$  on the (0001) graphite surface. *Surface Science*, 93:515–525, 1980.
- [54] Terrell L. Hill. *An Introduction to Statistical Thermodynamics*. Dover Publications, Inc., 1986.
- [55] Anutosh Chakraborty, Bidyut Baran Saha, Kim Choon Ng, Shigeru Koyama, and Kandadai Srinivasan. Theoretical insight of physical adsorption for a single-component adsorbent + adsorbate system: II. the Henry region. *Langmuir*, 25:7359–7367, 2009.
- [56] Shaheen A. Al-Muhtaseb and James A. Ritter. Roles of surface heterogeneity and lateral interactions on the isosteric heat of adsorption and adsorbed phase heat capacity. *J. Phys. Chem. B*, 103:2467–2479, 1999.
- [57] V. Buch. Path integral simulations of mixed para- $\text{D}_2$  and ortho- $\text{D}_2$  clusters: The orientational effects. *J. of Chem. Phys.*, 100:7610–7629, 1994.

- [58] R. Chahine and T. K. Bose. Characterization and optimization of adsorbents for hydrogen storage. *Proc. 11<sup>th</sup> World Hydrogen Energy Conf. Stuttgart*, pages 1259–1263, 1996.
- [59] Tae Hong Park. *Introduction to Digital Signal Processing*. World Scientific, 2010.
- [60] Mieczyslaw Jaroniec and Adam W. Marczewski. Physical adsorption of gases on energetically heterogeneous solids II. theoretical extension of a generalized Langmuir equation and its application for analysing adsorption data. *Montash. Chem.*, 115:1013–1038, 1984.
- [61] Leszek Czepirski and Jacek Jagiello. Virial-type thermal equation of gas-solid adsorption. *Chem. Eng. Sci.*, 44:797–801, 1989.
- [62] Bryan J. Schindler and M. Douglas LeVan. The theoretical maximum isosteric heat of adsorption in the Henry’s law region for slit-shaped carbon nanopores. *Carbon*, 46:644–648, 2008.
- [63] Jian Liu and M. Douglas LeVan. Isosteric heats of adsorption in the Henry’s law region for carbon single wall cylindrical nanopores and spherical nanocavities. *Carbon*, 47:3415–3423, 2009.
- [64] Jing Li and Erdong Wu. Adsorption of hydrogen on porous materials of activated carbon and zeolite NaX crossover critical temperature. *J. of Supercritical Fluids*, 49:196–202, 2009.
- [65] Barbara Panella, Michael Hirscher, and Siegmund Roth. Hydrogen adsorption in different carbon nanostructures. *Carbon*, 43(10):2209 – 2214, 2005.

- [66] Qinyu Wang and J. Karl Johnson. Molecular simulation of hydrogen adsorption in single-walled carbon nanotubes and idealized carbon slit pores. *J. Chem. Phys.*, 110(1):577–586, 1999.
- [67] B. Kuchta, L. Firlej, Sz. Roszak, C. Wexler, and P. Pfeifer. Influence of structural heterogeneity of nano-porous sorbent walls on hydrogen storage. *Applied Surface Science*, 265(17):5270–5274, 2009.
- [68] B. Kuchta, L. Firlej, R. Cepel, P. Pfeifer, and C. Wexler. Structural and energetic factors in designing a nanoporous sorbent for hydrogen storage. *Colloids and Surfaces A*, 347:61–66, 2009.
- [69] L. Firlej, B. Kuchta, C. Wexler, and P. Pfeifer. Boron substituted graphene: energy landscape for hydrogen adsorption. *Adsorption*, 15:312–317, 2009.
- [70] P. Pfeifer, F. Ehrburger-Dolle, T. P. Rieker, M. T. Gonzalez, W. P. Hoffman, M. Molina-Sabio, F. Rodriguez-Reinoso, P.W. Schmidt, and D. J. Voss. Nearly space-filling fractal networks of carbon nanopores. *Phys. Rev Letters*, 88(11):1155021, 2002.
- [71] P. A. Georgiev, A. Giannasi, D. K. Ross, M. Zoppi, J. L. Sauvojol, and J. Stride. Experimental Q-dependence of the rotational  $J = 0$ -to-1 transition of molecular hydrogen adsorbed in single-wall carbon nanotubes. *Chemical Physics*, 328:318–323, 2006.
- [72] P. A. Georgiev, D. K. Ross, A. De Monte, U. Montaretto-Marullo, R. A. H. Edwards, A. J. Ramirez-Cuesta, M. A. Adams, and D. Colognesi. In situ inelastic neutron scattering studies of the rotational and translational dynamics of molecular hydrogen adsorbed in single-wall carbon nanotubes (SWNTs). *Carbon*, 43:895–906, 2005.

- [73] Y. Ren and D. L. Price. Neutron scattering study of H<sub>2</sub> adsorption in single-walled carbon nanotubes. *Applied Physics Letters*, 79(22):3684–3686, 2001.
- [74] H. Gijs Schimmel, Gordon J. Kearley, and Fokko M. Mulder. Resolving rotational spectra of hydrogen adsorbed on a single-walled carbon nanotube substrate. *Chem Phys Chem*, 5:1053–1055, 2004.
- [75] P. A. Georgiev, D. K. Ross, P. Albers, and A. J. Ramirez-Cuesta. The rotational and translational dynamics of molecular hydrogen physisorbed in activated carbon: A direct probe of microporosity and hydrogen storage performance. *Carbon*, 44:2724–2738, 2006.
- [76] F. Fernandez-Alonso, F. J. Bermejo, C. Cabrillo, R. O. Loutfy, V. Leon, and M. L. Saboungi. Nature of the bound states of molecular hydrogen in carbon nanohorns. *Phys. Rev. Lett.*, 98(21):215503, 2007.
- [77] H. Gijs Schimmel, Gordon J. Kearley, Marije G. Nijkamp, Cornelis T. Visser, Krijn P. de Jong, and Fokko M. Mulder. Hydrogen adsorption in carbon nanostructures: Comparison of nanotubes, fibers, and coals. *Chemistry A European Journal*, 9(19):4764–4770, 2003.
- [78] Nathaniel L. Rosi, Juergen Eckert, Mohamed Eddaoudi, David T. Vodak, Jaheon Kim, Michael O’Keeffe, and Omar M. Yaghi. Hydrogen storage in microporous metal-organic frameworks. *Science*, 300(5622):1127–1129, 2003.
- [79] Jesse L. C. Rowsell, Juergen Eckert, and Omar M. Yaghi. Characterization of H<sub>2</sub> binding sites in prototypical metal-organic frameworks by inelastic neutron scattering. *J. Am. Chem. Soc.*, 127(42):14904–14910, 2005.
- [80] Herve Jobic, Gerard Clugnet, Michel Lacroix, Shibin Yuan, Claude Mirodatos, and Michele Breyse. Identification of new hydrogen species adsorbed on ruthe-

- mium sulfide by neutron spectroscopy. *J. Am. Chem. Soc.*, 115(9):3654–3657, 1993.
- [81] Joseph Howard, Thomas C. Waddington, and Christopher J. Wright. The vibrational spectrum of hydrogen adsorbed on palladium black measured using inelastic neutron scattering spectroscopy. *Chem. Phys. Lett.*, 56(2):258–262, 1978.
- [82] Juergen Eckert, Jacqueline M. Nicol, Joseph Howard, and Frans R. Trouw. Adsorption of hydrogen in ca-exchanged na-a zeolites probed by inelastic neutron scattering spectroscopy. *J. Phys. Chem*, 100(25):10646–10651, 1996.
- [83] J. Z. Larese, T. Arnold, L. Frazier, R. J. Hinde, and A. J. Ramirez-Cuesta. Direct observation of H<sub>2</sub> binding to a metal oxide surface. *Phys. Rev. Lett.*, 101(16):165302, 2008.
- [84] F.M. Mulder, T.J. Dingemans, H.G. Schimmel, A.J. Ramirez-Cuesta, and G.J. Kearley. Hydrogen adsorption strength and sites in the metal organic framework MOF5: Comparing experiment and model calculations. *Chem. Phys.*, 351:72–76, 2008.
- [85] Craig M Brown, Yun Liu, Taner Yildirim, Vanessa K Peterson, and Cameron J Kepert. Hydrogen adsorption in HKUST-1: a combined inelastic neutron scattering and first-principles study. *Nanotechnology*, 20(20):204025, 2009.
- [86] P. A. Georgiev, Alberto Albinati, Barbara L. Mojet, Jacques Ollivier, and Juergen Eckert. Observation of exceptionally strong binding of molecular hydrogen in a porous material: Formation of an  $\eta^2$ -H<sub>2</sub> complex in a Cu-exchanged ZSM-5 zeolite. *J. Am. Chem. Soc.*, 129(26):8086–8087, 2007.
- [87] James A. Young and Juan U. Koppel. Slow neutron scattering by molecular hydrogen and deuterium. *Phys. Rev.*, 135(3A):603–611, 1964.

- [88] Minzhong Xu, Francesco Sebastianelli, Brittney R. Gibbons, Zlatko Bacic, Ronald Lawler, and Nicholas J. Turro. Coupled translation-rotation eigenstates of  $H_2$  in  $C_{60}$  and  $C_{70}$  on the spectroscopically optimized interaction potential: Effects of cage anisotropy on the energy level structure and assignments. *J. Chem. Phys.*, 130:224306, 2009.
- [89] Q Wang and J.K. Johnson. Thermodynamic properties and phase equilibrium of fluid hydrogen from path integral simulations. *Molecular Physics*, 89(4):1105–19, 1996.
- [90] R. J. Elliott and W. M. Hartmann. Theory of neutron scattering from liquid and solid hydrogen. *Proc. Phys. Soc. London*, 90:671–860, 1967.
- [91] M. Nielsen, J. P. McTague, and W. Ellenson.  $H_2$  and  $D_2$  on graphite studied by neutron scattering. *Proceedings of the Fourteenth International Conference on Low Temperature Physics*, 14:437–440, 1975.
- [92] S. F. Parker, C. J. Carlile, T. Pike, J. Tomkinson, R. J. Newport, C. Andreani, F. P. Ricci, F. Sacchetti, and M. Zoppi. TOSCA: a world class inelastic neutron spectrometer. *Physica B: Condens. Matter*, 241:154–156, 1998.
- [93] Peter J.F. Harris, Zheng Liu, and Kaza Suenaga. Imaging the atomic structure of activated carbon. *J. Phys.: Condens. Matter*, 20:362201, 2008.
- [94] Artur P. Terzyk, Sylwester Furmaniak, Piotr A. Gauden, Peter J. F. Harris, Jerzy Wloch, and Piotr Kowalczyk. Hyper-parallel tempering monte carlo simulations of Ar adsorption in new models of microporous non-graphitizing activated carbon: effect of microporosity. *J. Phys.: Condens. Matter*, 19(40):406208, 2007.
- [95] Artur P. Terzyk, Sylwester Furmaniak, Peter J. F. Harris, Piotr A. Gauden, Jerzy Wloch, Piotr Kowalczykd, and Gerhard Rychlickia. How realistic is the

- pore size distribution calculated from adsorption isotherms if activated carbon is composed of fullerene-like fragments? *Phys. Chem. Chem. Phys.*, 9:5919–5927, 2007.
- [96] D. J. Narehood, M. K. Kostov, P. C. Eklund, M. W. Cole, and P. E. Sokol. Deep inelastic scattering of H<sub>2</sub> in single walled carbon nanotubes. *Phys. Rev. B*, 65:233401, 2002.
- [97] T. J. Krieger and M. S. Nelkin. Slow neutron scattering by molecules. *Phys. Rev.*, 106:290–295, 1957.
- [98] T. Kamiyama, Y. Kiyonagi, T. Horikawa, H. Iwasa, T. Uchida, T. Ebinuma, H. Narita, and S.M. Bennington. Dynamical features of methane hydrate around 12 K. *Physica B*, 350:e395–e398, 2004.
- [99] U. Fano. Effects of configuration interaction on intensities and phase shifts. *Phys. Rev.*, 124:1866–1878, 1961.
- [100] L. Firlej, S. Roszak, B. Kuchta, P. Pfeifer, and C. Wexler. Enhanced hydrogen adsorption in boron substituted carbon nanospaces. *J. Chem. Phys.*, 131:164702, 2009.
- [101] David F. Quinn. Supercritical adsorption of permanent gases under corresponding states on various carbons. *Carbon*, 40:2767–73, 2002.
- [102] Joseph Goldstein, Dale Newbury, David Joy, Charles Lyman, Patrick Echlin, Eric Lifshin, Linda Sawyer, and Joseph Michael. *Scanning Electron Microscopy and X-Ray Microanalysis*. Springer Science, 2003.
- [103] M. Endo, Y. J. Kim, T. Takeda, T. Maeda, T. Hayashi, K. Koshiba, H. Hara, and M. S. Dresselhaus. Poly(vinylidene chloride)-based carbon as an electrode

material for high power capacitors with an aqueous electrolyte. *J. Electrochem. Soc.*, 148:A1135–40, 2002.

- [104] Philip L. Llewellyn and Guillaume Maurin. Gas adsorption microcalorimetry and modelling to characterise zeolites and related materials. *Comptes Rendus Chimie*, 8:283–302, 2005.

## VITA

Raina Janel Olsen was born in American Fork, Utah on December 24<sup>th</sup>, 1979. She began her long tenure at the University of Missouri Columbia as an undergraduate in the fall of 1998, obtaining BS degrees in Computer Engineering and Electrical Engineering in May 2002. After working for several years as a full time research specialist in the Mechanical Engineering department under the direction of Steven Neal, she started on course work for her MS degree in Electrical Engineering with an emphasis in signal processing, which was obtained in December 2007 under the direction of Dominic Ho. Shortly before this, Raina started working in the Physics department under the direction of Carlos Wexler, ultimately obtaining MS and PhD degrees in Physics in May of 2011, with an emphasis in condensed matter and hydrogen adsorption.